Large-Eddy Simulation of Flow Separation and Control on a Wall-Mounted Hump

Thesis by

Jennifer Ann Franck

In Partial Fulfillment of the Requirements

for the Degree of

Doctor of Philosophy

California Institute of Technology

Pasadena, California

2009

(Defended June 2, 2009)

To A., B. and C. Franck

Acknowledgments

I would first like to thank my advisor, Tim Colonius, for all the guidance and support he has provided throughout my graduate career. It has been a privilege to work for him over the past five years, and have such a talented scientist and engineer as a mentor. I am also gracious to my thesis committee members, Professors John Dabiri, Melany Hunt and Mory Gharib, for their feedback and advice in this thesis during my defense. I additionally would like to thank Professors G. Ravichandran and Julia Greer for their informal mentorship and friendship during my time at Caltech. And of course I need to acknowledge Linda Miranda and Cheryl Geer for all their administrative support, especially during the final months of my graduate studies when I was working remotely from Rhode Island.

Next I would like to acknowledge all the current and former members of the Colonius lab with whom I have had the pleasure of working with over the past five years: Eric Johnsen, Sam Taira, Guillaume Bres, Jeff Krimmel, Kristjan G., Rick Burnes, Won Tae Joe, Keita Ando, and Vedran Coralic. Working in the basement of Thomas would not have been nearly as enjoyable without the wonderful comradery of my labmates. I especially want to thank Jeff for maintaining the precious computers and clusters we rely on for our research, and basically teaching me everything I know about Linux and Beowulf cluster administration. I would also like to acknowledge Daniel Appelo for many fruitful discussions on the numerical challenges of my project, and Rick Burnes and Daniel Chung for the many conservations and suggestions in regard to LES.

I am also grateful for the many friends I have made at Caltech throughout the past six years. Starting from the beginning, I would like to acknowledge those who helped me survive the first menacing year at Caltech, and for the wonderful friendships that evolved from it: Winston Jackson, Ivan Bermejo Moreno, Manuel Lombardini, Lydia (Trevino) Ruiz, and Brenda (Ramirez) Hernandez.

I do not miss those nights we spent in SFL! Especially Winston, with whom I studied for qualifying exams, and who successfully taught me much about solid mechanics in the six weeks preceding the exams.

Outside of research at Caltech, I spent a considerable amount of time with two science and education outreach organizations on campus, Caltech Classroom Connection and the Young Engineering and Science Scholars (YESS). Both programs have provided me with terrific experiences, and I want to thank those who I have worked with and those who gave me the opportunity to be a part of these programs, especially Luz Rivas, Winston Jackson, James Maloney, Tara Gomez and Lydia Ruiz.

In order to keep my sanity I was often off to the gym or going for a run after work, so I definitely need to acknowledge my exercise partners (and former roommate) Katy Augustyn and Paul Lee. We had many exciting times together, mostly either burning or consuming calories, probably more of the latter. I am also fortunate to have had two fantastic friends in the Firestone building, Winston Jackson and Linda Miranda, whom I could always count on for anything. In the final months of preparing my thesis and finishing my research remotely I have relied on a few people who have literally given me a place to sleep, so thank you again to the Greer family and Paul Lee.

Finally I would like to thank my husband Christian, who supported me every step of the way. I do not think I can thank him enough for everything he has done to help me graduate from Caltech: from encouraging me to apply in the first place to the thesis proofreading he has provided more recently. I am extremely lucky and I can certainly say I wouldn't be here without him! Besides Christian I am thankful for having such a wonderful family, my parents, Michael and Debbie Cobb, and siblings, Brian, Kevin and Sarah Cobb, who have provided encouragement and support during my entire undergraduate and graduate career in engineering.

The first three years of my graduate studies were funded by a National Science Foundation Graduate Research Fellowship. This work was also supported by the US Air Force Office of Scientific Research (FA9550-05-1-0369), and computational resources were provided by the Department of Defense High Performance Computing Centers.

Abstract

Active flow control techniques such as synthetic jets have been successful in increasing the performance of naturally separating flows on post-stall airfoils, bluff body shedding, and internal flows such as wide-angle diffusers. However, in order to implement robust control techniques there is a need for accurate computational tools capable of predicting unsteady separation and control at high Reynolds numbers. This thesis developed a compressible large-eddy simulation (LES) and validated it by simulating the turbulent flow over a wall-mounted hump. The flow is characterized by an unsteady, turbulent recirculation region along the trailing edge of the geometry, and is simulated at a Reynolds number of $500,000$. Active flow control is applied just before the natural separation point via steady suction and zero-net mass flux oscillatory forcing. The addition of control is shown to be effective in decreasing the size of the separation bubble and pressure drag. LES baseline and controlled results are validated against previously performed experiments by Seifert and Pack and those performed for the NASA Langley Workshop on Turbulent Flow Separation and Control. Three test cases are explored to determine the effect of explicit filtering and the Smagorinsky subgrid scale model on the average flow and turbulent statistics. The flow physics and the control effectiveness are investigated at two Mach numbers, $M = 0.25$ and $M = 0.6$. Compressibility is shown to increase the separation bubble length in the baseline case, but does not significantly change the effectiveness of the control. In terms of decreasing drag on the wall-mounted hump model, steady suction is more effective than oscillatory control, but both control techniques are effective in reducing the separation bubble length. Two-dimensional direct numerical simulations (DNS) of the wall-mounted hump flow are also presented, and the results show different baseline flow features than the 3D LES. However the controlled 2D flow gives an indication of the most receptive actuation frequencies around twice

that of the natural shedding frequency. Two regimes of reduced actuation frequency, $F^+ = O(1)$ and $F^+ = O(10)$, are also explored with the 3D LES. It is found that the low frequency actuation is successful in reducing the separation bubble length, but high frequency actuation produces an average flow comparable to the baseline case, and does not result in drag or separation bubble length reduction.

Contents

List of Figures

List of Tables

Nomenclature

a	=	speed of sound
$C_{d,p}$	=	form drag coefficient
C_m	=	mass flux coefficient
C_μ	=	momentum flux coefficient
$< C_\mu >$	=	unsteady momentum flux coefficient
C_p	=	average surface pressure coefficient
c	=	chord length
Δ	=	local grid resolution
E	=	total energy
e	=	internal energy
F^+	=	non-dimensional excitation frequency
f	=	excitation frequency
f_{sh}	=	natural shedding frequency
h_b	=	separation bubble height
h_s	=	control slot width
μ	=	dynamic fluid viscosity
Pr	=	Prandtl number
$\boldsymbol{q}$	=	heat flux vector
Re	=	Reynolds number
ρ	=	density
$\boldsymbol{S}$	=	rate of strain tensor
T	=	temperature

t	=	time
$\boldsymbol{\tau}$	=	stress tensor
$\boldsymbol{u}$	=	velocity vector
u_τ	=	wall friction velocity
ξ, η	=	body-fitted or computational coordinates
X_{sep}	=	distance from separation to reattachment
x, y, z	=	physical spatial coordinates
Subscripts		
∞	=	freestream conditions
re	=	reattachment
s	=	slot conditions
sep	=	separation
Superscripts		
$\bar{}$	=	fitted, averaged
$\tilde{}$	=	favre-averaged
sgs	=	sub-grid scale components

Chapter 1

Introduction

1.1 Motivation

When a boundary layer separates from a surface, it is almost always detrimental to the performance of a fluid system. In aerodynamics flow separation causes a dramatic decrease in lift and increase in drag, resulting in aerodynamic stall conditions. In an internal flow such as a wide-angle diffuser, flow separation decreases the total pressure recovery downstream, decreasing the efficiency of the system. Other examples include bluff body separation of flow over large-scale structures or automobiles, which leads to undesired oscillations and additional form drag.

Over the past century researchers have been interested in controlling or manipulating the natural instabilities that lead to separation. Depending on the application and desired performance factors the specific goals of control may be to completely reattach the boundary layer, or partially reattach it by delaying the onset of separation, initiating reattachment, or decreasing the size of the separated flow region.

Flow control can be divided into passive and active control. Passive control utilizes a change in surface morphology that beneficially modifies the flow dynamics, but is fixed in place and offers no adaptivity once installed. Vortex generators mounted on airplane wings are one example of passive control, in which the slender vanes are thought to re-energize the boundary layer and delay separation resulting in better performance envelopes for ailerons and flaps. On the other hand,

active control injects or withdraws mass or momentum from the flow via slots mounted flush to the surface and controlled by actuators.

Traditional boundary layer control is achieved through steady suction or blowing which is effective in increasing lift to drag ratios on airfoils, and has been implemented on production aircraft such as the Lockheed F-104. However steady suction/blowing control had limited success due to the complexity of the installed systems, whose added weight and power requirements outweighed the aerodynamic benefits [1] etc..

Much of the recent research on flow control has been focused on synthetic jets [2]. Synthetic jets are zero-net mass flux oscillatory control devices that are operated with lower power requirements than traditional boundary layer control. Synthetic jets have been shown to increase aerodynamic performance of naturally separating flows in laboratory experiments. However the development of accurate predictive tools for unsteady separation and control is just as important for the development of robust in-flight control systems. Such computational simulations remain a challenge [3] due to the complex geometries and configurations in which separation occurs, as well as the typically fully turbulent, high Reynolds number regime associated with realistic flight conditions. Since oscillatory control often creates unsteady vortical structures, simulations must also be time-dependent and capable of capturing large-scale unsteady flow structures.

This thesis presents a large-eddy simulation (LES) capable of predicting compressible flow separation and control at turbulent Reynolds numbers. The computational model is validated on a wall-mounted hump geometry, and flow control methodologies are explored and discussed with relevance to the fundamental flow physics.

Section 1.2 will provide the basics of flow control and background information relevant to separating and reattaching flows and control techniques. Section 1.3 will introduce previous experimental and computational studies on the wall-mounted hump geometry, and an overview of the current work will be presented in section 1.4.

1.2 Background

1.2.1 Basics of Flow Control

Traditional boundary layer control via steady suction or blowing is often characterized by the mass-flux coefficient C_m defined by

$$C_m = \frac{\rho_s u_s h_s}{\rho_\infty U_\infty c} \tag{1.1}$$

where the variables ρ_s, u_s, h_s are the density, velocity and width at the control slot and ρ_∞, U_∞, c are the density, velocity and characteristic length scale of the freestream flow. Likewise, the momentum coefficient C_μ is defined below as the momentum added to the flow divided by the momentum of the freestream.

$$C_\mu = \frac{\rho_s u_s^2 h_s}{0.5\rho_\infty U_\infty^2 c} \tag{1.2}$$

Steady suction and blowing is achieved through slots mounted in the surface, and require additional plumbing for the addition or subtraction of fluid which is often powered by an auxiliary unit. With the availability of smaller and cheaper electronic actuators and manufacturing, synthetic jet control has replaced much of the traditional boundary layer control research. A schematic of a synthetic jet is shown in figure 1.1. Such devices are often very small compared with the length of the body ($h_s/c < 0.01$) and are mounted flush with the surface. An oscillating surface, such as a membrane or piston adds momentum to the boundary layer, but only utilizes the fluid already contained in the system. Since the actuation devices can be manufactured small and driven with low power, synthetic jets can be more efficiently operated than traditional boundary layer control.

The amplitude of actuation is characterized by an unsteady momentum coefficient $\langle C_\mu \rangle$ defined by

$$\langle C_\mu \rangle = \frac{\rho_s \langle u_s \rangle^2 h_s}{0.5\rho_\infty U_\infty^2 c}, \tag{1.3}$$

and the frequency of oscillation is characterized by the reduced frequency

$$F^+ = \frac{f X_{sep}}{U_\infty}. \tag{1.4}$$

The length scale X_{sep} is the length of the separated region or the length from separation to the end of the body in cases where the flow does not reattach.

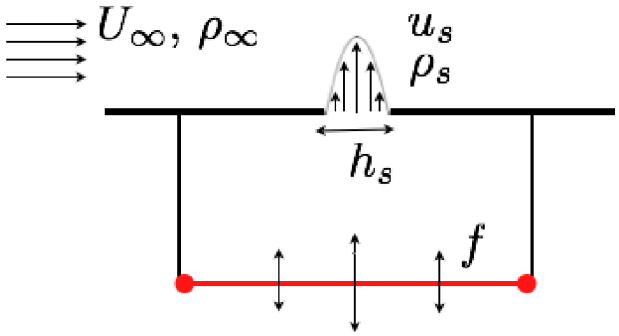

Figure 1.1: Schematic of a synthetic jet or oscillatory flow control device.

Momentum coefficients as low as 0.01% - 0.1% have been able to improve aerodynamic performance by altering the separation and reattachment dynamics of the natural system. Comparing similar levels C_μ and $\langle C_\mu \rangle$, oscillatory control is found to be just as effective as weak suction, and more effective than steady blowing [3]. As the value of C_μ increases and more momentum is added to the system, the effectiveness of the control generally increases. Whether the desired goal is to delay separation or shorten the separation region, control has shown to be most effective when applied just before the natural separation point.

1.2.2 Flow Separation and Reattachment

Control of flow separation has been investigated on a variety of different geometries, including backward-facing steps, high angle of attack airfoils, and bluff bodies such as cylinders. In bluff body flows, the separated shear layer has a natural instability that forms regular vortices that are shed downstream. In many separated flows such as a backward-facing step, or certain airfoil configurations, the separated shear layer interacts with the surface and naturally reattaches downstream,

forming a recirculation region. In order to control these flows, one must understand and control the dynamics of the entire separation bubble.

The initial formation of a separation bubble is very similar to a free shear layer, with the roll-up of spanwise vortices from the Kelvin-Helmholtz (KH) instabilities in the shear layer. However Castro and Haque [4] found many differences from a free shear layer in their experimental investigation of flow reattachment behind a plate normal to the flow direction. Their findings indicate a nonlinear growth rate with initially higher values than a free shear layer due to the higher level of turbulence in the recirculating flow. The growth rate decreases significantly as it approaches reattachment and turbulent Reynolds stresses are higher than levels expected in free shear layers. From a longitudinal velocity autocorrelation analysis, the authors found evidence of a low frequency motion in the beginning of the separation bubble that is lower than the large-scale structures formed by the shear layer. Low frequency motion, or flapping, has also been detected in the backward-facing step flow investigated by Eaton and Johnston [5] and Hudy et al. [6]. The low frequency is attributed to the growth and decay of the entire separation bubble, governed by the overall entrainment of fluid into the separation bubble.

Other investigations such as Sigurdson [7] and Kiya et al. [8] have focused on the large-scale shedding instability of the separation bubble. They experimentally investigated a circular cylinder whose axis is aligned with the freestream flow. Sigurdson found that the natural shedding frequency f_{sh} scales with the height of the separation bubble, h_b, and velocity at separation, U_s, and has a universal value of $f_{sh}h_b/U_s = 0.08$. This is the same as the Strouhal number St_h in bluff body separation, except rather than an alternating von Karman vortex street, the vortices here interact with their images resulting from the wall. Sigurdson claims the most effective forcing frequencies create vortices that amalgamate to form structures equal to the natural shedding frequency, or between $2f_{sh}$ and $5f_{sh}$. Kiya et al. [8] have proposed that the natural shedding frequency is due to an acoustic feedback loop. The impinging shear layer sends a pressure disturbance back to the separation location, which is then convected back downstream with the shear layer. Calculating the time for one feedback loop, the authors find a frequency of $f_{sh}x_R/U_\infty = 0.5$, which is consistent

with other reattaching experiments. They also supplement Sigurdson's argument about the most effective frequency being an integer multiple of f_{sh}.

1.2.3 Effect of Actuation Frequency

The effect of the actuation or forcing frequency has been tested in various experimental and computational studies. One of the simplest experimental setups is the deflected flap of Nishri and Wygnanski [9], where the addition of control at the separation point is able to reattach a naturally separated boundary layer. The deflected flap experiments determined that the boundary layer reattached at the lowest $\langle C_\mu \rangle$ when forced at a reduced frequency of $F^+ \approx 1$. Airfoil investigations have also increased lift in post-stall angles of attack for actuation frequencies $0.5 < F^+ < 1.5$ [10], a range that corresponds to the natural shedding frequency of the separated shear layer. It is hypothesized that adding oscillatory control regularizes shedding of the large scale vortices in the shear layer.

The effective range of forcing frequencies in separated flows has been investigated computationally and experimentally by many other researchers, where $F^+ \approx O(1)$ can either delay separation or initiate an earlier flow reattachment [1]. At this frequency large-scale vortices are created which increase the entrainment rate and deflect the separated shear layer towards the surface. This frequency scales with the separation bubble length, X_{sep}, and creates structures approximately the same height as the separation region.

The effect of higher actuation frequencies is not as clearly understood. These frequencies are an order of magnitude larger than the natural shedding or global frequency of the flow, or $F^+ \approx O(10)$. High frequency actuation has been effective in the experimental airfoil experiments of Amitay and Glezer [11]. In a stalled airfoil configuration they have shown that $F^+ \approx O(10)$ is more effective than O(1) forcing in increasing the suction force immediately after leading edge actuation. They also discovered that above a certain threshold $F^+ > 10$ all high frequencies exhibited the same averaged pressure forces, and are decoupled from the natural shedding instabilities of the flow. Velocity profiles and instantaneous vorticity plots show no evidence of large scale structures or reverse flow close to the surface, indicating that the flow is completely attached and separation is prevented. The authors

claim that the benefits of high frequency forcing are due to "virtual surface shaping" around the actuation location, or a modification to the average streamlines measuring 2-4 actuation wavelengths downstream [12]. This is accompanied by a decrease in the shear layer vorticity width and decrease in local Reynolds stresses in the near wake, particularly with the cross-stream fluctuations $\overline{v'v'}$.

The presence of multiple instabilities in the baseline flow has been documented in simulations by Wu et al. [13], Raju et al. [14], and Dandois et al. [15]. Wu et al. performed a two-dimensional Reynolds Averaged Navier-Stokes (RANS) computation of a stalled NACA 0012 airfoil. A spectral analysis determined a global instability corresponding to large scale shedding and a local instability over a broadband of higher frequencies in the shear layer just after separation likely due to Kelvin-Helmholtz instability of the separated shear layer. They found a locked-in frequency response when the flow is excited at twice the natural shedding frequency, corresponding to a highly organized vortex shedding and an increase in the lift-to-drag ratio.

Raju et al. [14] looked at a stalled airfoil using two-dimensional direct numerical simulations (DNS) at $Re = 44,000$, and also noted the presence of multiple instabilities in the baseline flow. These can be attributed to Kelvin-Helmholtz instabilities of the shear layer $St_{sh} \approx 12$, a shedding frequency from the roll up of vortices in the separated region $St_{sh} \approx 2$, and a low frequency in the wake of the airfoil $St_{sh} \approx 1$. Forcing at frequencies close to the natural shedding instability are found to be most effective in reducing separation and increasing the lift-to-drag ratio. Contrary to the experiments by Amitay and Glezer [11], forcing at the shear layer frequency had an unfavorable effect of increasing the separated region.

Dandois et al. [15] also found an increase in separation bubble length when high frequency forcing is investigated in the LES of a curved backward-facing step at $Re_h = 28,275$. The low frequency increases entrainment and turbulent kinetic energy whereas the high frequency modifies the mean streamwise velocity profile stability and decreases local kinetic energy. This supports the hypothesis by Stanek [16] that the high frequency forcing inhibits the growth of large scale structures by creating a more stable average velocity profile. This is in contrast to Glezer et al. who believe the high forcing frequency accelerates the turbulent energy cascade, enhancing energy transfer from

the larger to smaller scales [12].

1.3 Flow over a Wall-Mounted Hump Model

The wall-mounted hump model was created by Seifert and Pack [3] to experimentally investigate unsteady flow separation, reattachment and control at high Reynolds number,

$$Re = \rho_\infty U_\infty c/\mu, \tag{1.5}$$

defined by the chord length c and freestream velocity U_∞. The model approximates the upper surface of a 20% thick Glauert-Goldschmied type airfoil, originally developed in the early 20th century for traditional flow control applications. The model geometry is shown in figure 1.2, and features a highly convex region before the trailing edge, which initiates flow separation. The separated shear layer forms a turbulent and unsteady separation bubble over the trailing edge and eventually reattaches to the wall downstream of the model's chord length.

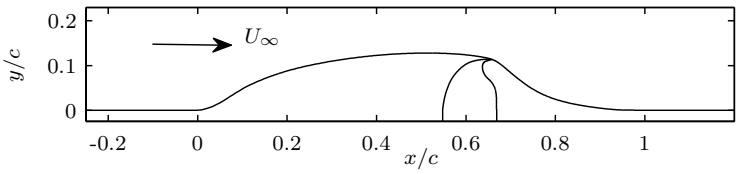

Figure 1.2: Wall-mounted hump geometry.

Seifert and Pack have investigated the flow experimentally for a variety of flow conditions at high Reynolds numbers, $2.4 \times 10^6 \leq Re \leq 26 \times 10^6$. Using a cryogenic flow facility and measuring the wall pressure fluctuations, they have documented the effect of flow control by means of steady suction and oscillatory forcing through a control cavity just before separation [3]. They have also investigated the effects of boundary layer thickness, compressibility, excitation location [17] and sweep [18] on the baseline and controlled flows. Their findings indicate that the flow dynamics are relatively independent of Reynolds number and boundary layer thickness, as long as the upstream boundary

layer remains fully turbulent. Steady suction and blowing are applied just before separation and are found to completely reattach the flow at high momentum coefficients of 2%-4%, recovering the geometry's ideal pressure distribution. Oscillatory forcing at $0.4 \leq F^+ \leq 1.6$ is just as effective as steady blowing at low momentum coefficient values, with $F^+ = 1.6$ most effective in reattaching the flow. These findings remain true when the model was mildly swept at 30° [18].

As the Mach number is increased from $M = 0.25$ to $M = 0.7$, Seifert and Pack found a consistent increase in the separation bubble length, and the existence of a shock at separation for $M \geq 0.65$ [17]. They hypothesized that the interaction with the separation shock wave reduced the effectiveness of control at $M = 0.65$. The optimal excitation location for the incompressible Mach number was found to be just before the natural separation, whereas the compressible flow had a slightly better pressure recovery when control is applied upstream of separation and the shock wave.

The wall-mounted hump was also a test case at the CFD Validation of Synthetic Jets and Turbulent Separation Control workshop held at NASA Langley Research Center [19]. The workshop provided a separate set of experimental data of the baseline and controlled flow including additional data from pressure taps, particle image velocimetry (PIV), and oil film flow visualization along the surface of the hump [20, 21, 22]. The experiments are performed in a separate wind tunnel facility from previous experiments at a Reynolds number range of $Re \approx 1 \times 10^6$ and at incompressible Mach numbers $0.04 \leq M \leq 1.2$. Steady suction and oscillatory control are applied through a control cavity just before natural separation, and additional flow visualization, including average velocity profiles give insight into the flow dynamics for three workshop test cases.

The well documented wall-mounted hump experiments provide a database that can be utilized for the development of CFD techniques capable of simulating separation and control. It provides a challenging test case for CFD validation due to its arbitrarily curved geometry, unsteady separation and reattachment, and high Reynolds number separation bubble. Participants from the workshop simulated the wall-mounted hump flow using a variety of techniques, including Reynolds-averaged Navier-Stokes (RANS) and large-eddy simulation (LES) [19]. These methods displayed varying degrees of success in predicting the surface pressure coefficient of the baseline, steady suction, and

oscillatory control test cases at a Reynolds number of 9.29×10^5 based on the freestream velocity U_∞ and the chord length c. It has been shown that LES generally provides better agreement with the experimental reattachment location and separation bubble dynamics than RANS-based simulations [23, 24]. In particular, Morgan et al. [23] performed an implicit LES (ILES) on the baseline and controlled cases at a Reynolds number of 200,000, one fifth the Reynolds number of the Langley Research Center Workshop (LRCW) test case. Good agreement was found between the pressure coefficient in the baseline and steady suction control cases, however the separation bubble length was over-predicted in the oscillatory forcing. Increasing the magnitude of oscillatory forcing improved the separation bubble length, agreeing with the trend in experimental data. Saric et al. [24] found better agreement with the experiments using LES rather than RANS or detached eddy simulation (DES), which over-predicted the reattachment location. The dynamic Smagorinsky model of You et al. [25] best predicted the wall pressure coefficient and separation bubble length for the oscillatory control case.

1.4 Overview of Current Work

All previous wall-mounted hump simulations, including those solving the compressible equations, have focused on the low Mach number ($M = 0.1$) results from the LRCW test case. The numerical method presented in this thesis is a compressible large-eddy simulation capable of modeling the compressible subsonic flow over the hump and demonstrates improved results from a previous ILES [26], particularly in the prediction of the controlled cases. The effects of using an explicit filter to remove the smallest scales instead of a subgrid scale (SGS) model is investigated and discussed. The formulation of the numerical method and a discussion of the numerical dissipation is presented in Chapter 2.

Chapter 3 is a validation of the LES using the wall-mounted hump experiments of Seifert and Pack and the experiments from the Langley Research Center workshop (LRCW) test cases. The baseline LES flow is presented at $M = 0.25$ and compared with low Mach number experiments. Active flow control is applied according to the test cases at the LRCW for both steady suction and

oscillatory forcing. The effect of the turbulence model parameters is also explored in more detail for the oscillatory flow test case.

In Chapter 4, the flow physics of the controlled and baseline cases are discussed with respect to the shear layer growth rate and fundamental instabilities detected in the flow. A comparison between the low and high (subsonic) Mach numbers are presented for the baseline and controlled flows. The effectiveness of control on the wall-mounted hump is also discussed.

Chapter 5 explores two ranges of actuation frequency, $F^+ = O(1) - O(10)$. The flow physics resulting from the various actuation frequencies are discussed and compared with findings from other investigations. The global and local effects of low and high frequency actuation are presented.

Finally, a concluding Chapter summarizes the main results and discusses future recommendations and directions for related research.

1.5 List of Significant Contributions

The following items represent the significant contributions presented in this thesis in the research areas of computational fluid dynamics, separated flows, and active flow control.

- Development of a compressible large-eddy simulation (LES) code capable of capturing turbulent, unsteady separation and control.
- Implementation of new numerical techniques in the LES code that provide better energy conversation and stability, producing a robust LES code without the need of explicit filtering.
- Integrated a conformal mapping routine in MATLAB with the generalized coordinate system of the LES code to create arbitrary body-fitted grids for simulation of complex flow configurations.
- Validation of the LES code at low and high (subsonic) Mach numbers using a wall-mounted hump geometry, which properly captured the effects of compressibility through the separated flow region.

- Modeled and validated steady suction and zero-net mass oscillatory flow control, and an assessed the control's effectiveness on the wall-mounted hump flow in terms of drag and separation bubble reduction.

- Compared the flow structure and vortex dynamics between two-dimensional low Reynolds and three-dimensional high Reynolds number separated and controlled flows.

- An investigation into the effects of actuation frequency of control applied to the wall-mounted hump flow.

Chapter 2

Large Eddy Simulation and Numerical Methods

In order to simulate high Reynolds number flow within a tractable computation time, a large eddy simulation (LES) is implemented. LES resolves the flow scales larger than the local grid size and applies either numerical dissipation or a physical model to capture the important dynamics of the smaller scales. This chapter will formulate the governing equations used in the LES, including the subgrid scale model, and present the numerical methods utilized in solving the equations. Additionally, the computational details of the wall-mounted hump simulation, including the flow control model, will be discussed.

2.1 Large Eddy Simulation Equations

The compressible large eddy simulation equations are derived by applying a spatial low-pass filter $G(\mathbf{x}-\mathbf{x}';\Delta)$ of width Δ to the compressible Navier-Stokes equations,

$$\bar{f}(\mathbf{x},t) = \int G(\mathbf{x}-\mathbf{x}';\Delta) f(\mathbf{x}',t) d\mathbf{x}', \tag{2.1}$$

where $\bar{f}$ represents the low-pass filtered flow variable f. The filtered compressible Navier-Stokes equations can be simplified by the Favre-averaging or density weighting given by

$$\tilde{f} = \frac{\overline{\rho f}}{\bar{\rho}} \tag{2.2}$$

where ρ is the density. The resulting continuity, momentum, and energy equations (neglecting any filter non-commutivity) are given by

$$\frac{\partial \bar{\rho}}{\partial t} + \frac{\partial}{\partial x_j}\bar{\rho}\tilde{u}_j = 0 \tag{2.3a}$$

$$\frac{\partial}{\partial t}\bar{\rho}\tilde{u}_i + \frac{\partial}{\partial x_j}(\bar{\rho}\tilde{u}_i\tilde{u}_j - \tilde{\tau}_{ji}) + \frac{\partial \bar{p}}{\partial x_i} = \frac{\partial}{\partial x_j}\tau_{ij}^{sgs} \tag{2.3b}$$

$$\frac{\partial}{\partial t}\bar{\rho}\tilde{E} + \frac{\partial}{\partial x_j}((\bar{\rho}\tilde{E} + \bar{p})\tilde{u}_j + \tilde{q}_j - \tilde{\tau}_{ji}\tilde{u}_i) = \frac{\partial}{\partial x_j}q_j^{sgs} \tag{2.3c}$$

where the quantities velocity and pressure are given by u_i and p respectively. The total energy is denoted by E and is formulated by $E = e + 0.5(u_i u_i)^2$, where e is the internal energy per unit mass. The filtered stress tensor, $\tilde{\tau}_{ij}$, and heat flux vector, $\tilde{q}_j$, components are

$$\tilde{\tau}_{ij} = \mu\left[\left(\frac{\partial \tilde{u}_i}{\partial x_j} + \frac{\partial \tilde{u}_j}{\partial x_i}\right) + \frac{2}{3}\frac{\partial \tilde{u}_k}{\partial x_k}\delta_{ij}\right] \tag{2.4a}$$

$$\tilde{q}_j = \frac{\mu}{Pr}\frac{\partial \tilde{T}}{\partial x_j} \tag{2.4b}$$

where $\tilde{T}$ is the filtered temperature variable. The length scales are non-dimensionalized by the chord length, c, and the freestream values of density, ρ_∞, and the speed of sound, a_∞. The pressure is non-dimensionalized by ρa_∞^2. The dynamic viscosity is held constant, the Prandtl number is fixed at 0.7, and the filtered ideal gas law is used as the equation of state, neglecting the subgrid transport terms that arise from filtering. The terms τ_{ij}^{sgs} represent the quantity $\bar{\rho}(\widetilde{u_i u_j} - \tilde{u}_i\tilde{u}_j)$, and $q_{ij}^{sgs} = \widetilde{Tu_i} - \tilde{T}\tilde{u}_i$. These terms arise due to the filtering of products on the left-hand-side of the equations and cannot be calculated directly prompting the need for a subgrid scale (SGS) model. The LES uses an eddy-viscosity Smagorinsky formulation for compressible flows [27], and the SGS model terms are given by

$$\tau_{ij}^{sgs} = C_s\Delta^2\bar{\rho}|\tilde{S}|\tilde{S}_{ij} \tag{2.5a}$$

$$q_j^{sgs} = C_q\Delta^2\bar{\rho}|\tilde{S}|\frac{\partial \tilde{T}}{\partial x_j} \tag{2.5b}$$

where Δ is the low pass filter width and $\tilde{S}_{ij}$ are the filtered rate of strain components. The filtered rate of strain is defined by

$$\tilde{S}_{ij} = \frac{1}{2}\left(\frac{\partial \tilde{u}_i}{\partial x_j} + \frac{\partial \tilde{u}_j}{\partial x_i}\right) \tag{2.6a}$$

$$|\tilde{S}| = (2\tilde{S}_{ij}\tilde{S}_{ij})^{1/2} \tag{2.6b}$$

and the filter width Δ, is calculated from the local grid spacings in the three coordinate directions, $\Delta = (\Delta_x \Delta_y \Delta_z)^{1/3}$. A constant Smagorinsky model is utilized with the coefficients C_s and C_q set to 0.06. With the constant coefficient method implemented, a van Driest damping function is used to decrease the characteristic length scale, Δ, along the wall boundary using an empirical law of the wall formulation [28]. The scaling function and related parameters are defined below.

$$\Delta' = \{1 - exp(x_2^+/A^+)\}\Delta \tag{2.7a}$$

$$x_2^+ = x_2 u_\tau/\nu, \qquad A^+ = 25 \tag{2.7b}$$

$$\frac{\overline{u_1}}{u_\tau} = 8.7 \cdot (y u_\tau/\nu)^{(1/7)} \tag{2.7c}$$

2.2 Computational Methods

In order to accommodate a broader range of geometries, the governing equations are solved in generalized coordinates $\xi = f(x, y)$ and $\eta = f(x, y)$ in the streamwise and wall-normal directions. The equations are solved in a uniformly spaced rectangular domain and transformed to the physical domain via a conformal mapping. The three-dimensional governing equations in generalized coordinates are given below, where $J = \xi_x \eta_y - \xi_y \eta_x$. The spanwise direction is homogeneous, and solved on a uniformly spaced grid, thus no coordinate transformation in z is required.

$$\frac{Q_t}{J} + \left(\frac{\xi_x F + \xi_y G}{J}\right)_\xi + \left(\frac{\eta_x F + \eta_y G}{J}\right)_\eta + \frac{I_z}{J} = \mu\left[\left(\frac{\xi_x^2 + \xi_y^2}{J} H_\xi\right)_\xi + \left(\frac{\eta_x^2 + \eta_y^2}{J} H_\eta\right)_\eta + \frac{H_{zz}}{J}\right] \tag{2.8}$$

$$Q = \begin{bmatrix} \bar{\rho}\tilde{u} \\ \bar{\rho}\tilde{v} \\ \bar{\rho}\tilde{w} \\ \bar{\rho} \\ \bar{\rho}\tilde{E} \end{bmatrix} \qquad H = \begin{bmatrix} \tilde{u} \\ \tilde{v} \\ \tilde{w} \\ 0 \\ \frac{C_p}{Pr}\tilde{T} \end{bmatrix}$$

$$F = \begin{bmatrix} \bar{\rho}\tilde{u}^2 + \tilde{p} - \frac{1}{3}\mu(\tilde{u}_x + \tilde{v}_y + \tilde{w}_z) \\ \bar{\rho}\tilde{u}\tilde{v} \\ \bar{\rho}\tilde{u}\tilde{w} \\ \bar{\rho}\tilde{u} \\ \bar{\rho}\tilde{u}H - \mu(\tilde{u}\tilde{\tau}_{xx} + \tilde{v}\tilde{\tau}_{xy} + \tilde{w}\tilde{\tau}_{xz}) \end{bmatrix} \qquad G = \begin{bmatrix} \bar{\rho}\tilde{u}\tilde{v} \\ \bar{\rho}\tilde{v}^2 + \tilde{p} - \frac{1}{3}\mu(\tilde{u}_x + \tilde{v}_y + \tilde{w}_y) \\ \bar{\rho}\tilde{u}\tilde{w} \\ \bar{\rho}\tilde{v} \\ \bar{\rho}\tilde{v}H - \mu(\tilde{u}\tilde{\tau}_{xy} + \tilde{v}\tilde{\tau}_{yy} + \tilde{w}\tilde{\tau}_{yz}) \end{bmatrix}$$

$$I = \begin{bmatrix} \bar{\rho}\tilde{u}\tilde{w} \\ \bar{\rho}\tilde{v}\tilde{w} \\ \bar{\rho}\tilde{w}^2 + \tilde{p} - \frac{1}{3}\mu(\tilde{u}_x + \tilde{v}_y + \tilde{w}_y) \\ \bar{\rho}\tilde{w} \\ \bar{\rho}\tilde{w}H - \mu(\tilde{u}\tilde{\tau}_{xz} + \tilde{v}\tilde{\tau}_{yz} + \tilde{w}\tilde{\tau}_{zz}) \end{bmatrix}$$

Two computational formulations for solving the compressible LES equations are presented in the following sections. The original computational method is based on the divergence form of the momentum and energy equations and a finite difference method from a previous two-dimensional direct numerical simulation (DNS) code [29]. The second method solves the convective terms in a skew-symmetric formulation and implements a finite difference solver based on summation by parts (SBP) operators [30]. The details and the benefits of each method are discussed in the next two sections. Both fomulations utilize high-order accurate finite difference methods in the streamwise and wall-normal directions, and a Fourier method for derivatives in the spanwise or z direction. Time-stepping is accomplished with a fourth order Runge-Kutta scheme.

2.2.1 Divergence Formulation

The divergence formulation is based on the two-dimensional direct numerical simulation (DNS) code originally developed for a diffuser geometry by Pirozzoli and Colonius [29], and also used by Suzuki et al. [31]. The convective terms of the momentum and energy equations are computed in the same manner as presented in 2.3. The derivatives in the computational domain are solved using a sixth-order Padé scheme in the wall-normal direction with lower order implicit schemes along the boundaries. The derivatives in the streamwise direction are computed with a fourth-order optimized explicit scheme implemented by Fung [32] in order to easily divide the computational load for parallel computing.

With the divergence formulation of the equations, aliasing errors build up in regions where the flow is under-resolved. These numerical errors originate as grid point-to-grid point oscillations and grow in amplitude until the code can no longer handle the unphysical size of the conservative variables (e.g., negative energy or density values). With DNS this is generally not an issue, because one is interested in resolving all the scales of motion. With the divergence form of the LES equations currently implemented, the modeled subgrid scale dissipation is not capable of removing the numerical instabilities that develop, and thus it is impossible to run the solver without explicitly filtering out the unphysical oscillations.

The divergence method also solves the non Favre-averaged filtered Navier-Stokes equations instead of those given by Eqs. (2.3), and whose details can be found in Appendix A. The non Favre-averaged filtered equations have additional SGS terms, and have been previously used by Bodony [33] and Boersma and Lele [34]. Although the Favre-averaged approach is simpler to implement due to less SGS terms, the non Favre-averaged equations are closer to the underlying physics, and the addition of the damping term in the continuity equation is believed to help decrease grid point-to-grid point oscillations [34].

2.2.2 LES Explicit Spatial Filtering

The LES equations are derived with a low-pass filter that captures the large scale structures and must include a model for those scales smaller than the given filter width. An implicit filter of width Δ can be implied from the grid spacing since the numerical method cannot accurately resolve scales smaller than the local grid spacing. With the divergence form of the governing equations, an additional explicit filter is required to remove unphysical numerical instabilities.

In the divergence formulation of the code, an 8th order implicit filter given by

$$\alpha_f(\hat{f}_{i-1} + \hat{f}_{i+1}) = \frac{1}{2}\sum_{n=0}^{N} a_n(f_{i+n} + f_{i-n}) \tag{2.9}$$

with $N = 4$ is implemented. It is part of a family of filters originally developed by Visbal and Gaitonde [35] and used in previous LES applications [23, 33]. The free parameter α_f can adjust the sharpness of the transfer function, as demonstrated in figure 2.1. In the non-periodic directions, the points close to the boundary use the appropriate lower order filter corresponding to a smaller stencil size (with the same value of α_f), and the boundary points in each coordinate direction are not filtered at all. Due to the parallelization scheme of the code, an explicit filter was required in the streamwise direction. Therefore, an explicit filter with a large 29-point stencil is used in the streamwise direction, and was chosen because it most closely matched the transfer function of the implicit filter for the commonly used value of $\alpha_f = 0.47$. The conservative variables are filtered after every full time-step, ideally removing the smallest scales associated with the numerical instability but with a minimal effect on the larger scale structures.

The minimum amount of filtering needed depends on the Reynolds number and Mach number. Typical values used in the simulations are $\alpha_f = 0.45 - 0.47$.

2.2.3 Skew-Symmetric Formulation

Although explicit filtering eliminates the numerical instabilities it can also have undesired effects on the physical or resolved scales. This is especially true for grids that have been aggressively

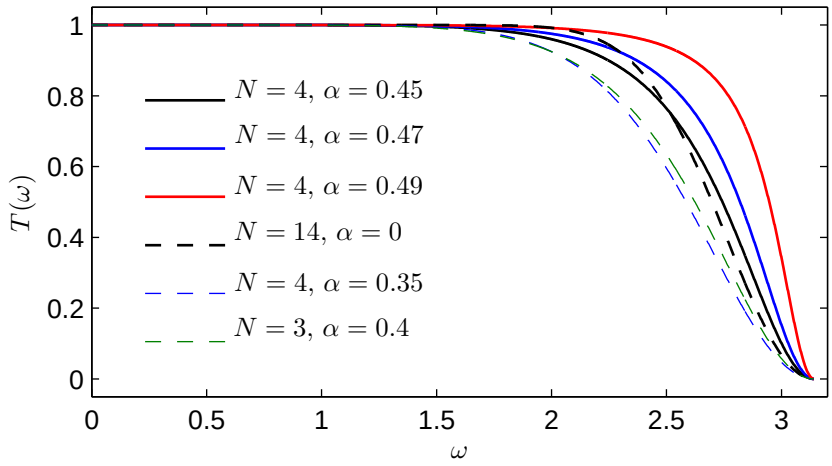

Figure 2.1: The transfer function associated with the Visbal and Gaitonde filter for various values of α_f and N. $\alpha_f = 0.45 - 0.47$ is commonly used in the spanwise and wall-normal direction, while the explicit N=14 filter is used in the streamwise direction.

stretched and for filters without a sharp cut-off. Even with a sharp cut-off and uniformly spaced grid points, filtering reduces the effective resolution of the simulation. Therefore there have been many attempts to alleviate the numerical instabilities of the divergence formulation. Most have focused on implementing a conservative numerical scheme, which for incompressible flows means conserving mass, momentum, and kinetic energy. This is accomplished with various methods, including a staggered grid arrangement or a skew-symmetric formulation of the momentum convective terms [36]. An overview of various techniques for compressible flows is given by Honein and Moin [37]. In the current implementation, we maintain a collocated grid but implement the skew-symmetric formulation of the momentum terms. This is accomplished by decomposing the momentum term $\frac{\partial(\rho u_i u_j)}{\partial x_j}$ as shown below.

$$\frac{\partial(\rho u_i u_j)}{\partial x_j} \rightarrow \frac{1}{2}\frac{\partial(\rho u_i u_j)}{\partial x_j} + \frac{\rho u_j}{2}\frac{\partial u_i}{\partial x_j} + \frac{u_i}{2}\frac{\partial(\rho u_j)}{\partial x_j} \tag{2.10}$$

The convective term in the energy equation is first decomposed to its internal energy and pressure components,

$$\frac{\partial((\rho E+p)u_j)}{\partial x_j} = \frac{\partial(\rho e u_j)}{\partial x_j} + \frac{1}{2}\frac{\partial(\rho u_i u_i u_j)}{\partial x_j} + \frac{\partial(p u_j)}{\partial x_j} \tag{2.11}$$

and the new internal energy term is rewritten in skew-symmetric formulation. The final form of the energy convective term is computed as

$$\frac{\partial((\rho E+p)u_j)}{\partial x_j} \rightarrow \frac{1}{2}\frac{\partial(\rho e u_j)}{\partial x_j} + \frac{\rho u_j}{2}\frac{\partial e}{\partial x_j} + \frac{e}{2}\frac{\partial(\rho u_j)}{\partial x_j} + \frac{1}{2}\frac{\partial(\rho u_i u_i u_j)}{\partial x_j} + \frac{\partial(p u_j)}{\partial x_j}. \tag{2.12}$$

Equations 2.10 and 2.12 introduce many new terms that must be computed at every right-hand side iteration. In addition, these new terms must be rewritten in generalized coordinates to fit smoothly in the code architecture. An example of one of the new terms in generalized coordinates is given by

$$\frac{u_i}{2}\frac{\partial(\rho u_j)}{\partial x_j} \rightarrow \frac{u_i}{2}\left[\left(\frac{\rho u \xi_x + \rho v \xi_y}{J}\right)_\xi + \left(\frac{\rho u \eta_x + \rho v \eta_y}{J}\right)_\eta + \frac{1}{J}\frac{\partial(\rho w)}{\partial z}\right]. \tag{2.13}$$

Even after the splitting of the convective terms into the skew-symmetric parts numerical instabilities still arose from the boundaries. Therefore, summation by parts (SBP) boundary closures [30] were implemented because of their proven stability properties. The interior scheme was changed to a sixth-order explicit finite difference scheme with third-order accurate boundary closure derived from the SBP operators based on diagonal norms. The combination of the new boundary closures with the skew-symmetric formulation led to a solver that computes stable solutions without explicit filtering, even at high Reynolds numbers. It is noted that grid point-to-grid point oscillations can still occur due to grid stretching or grid abnormalities, but they do not necessarily grow unstable.

2.2.4 Grid Generation

A Schwartz-Christoffel mapping is used to generate a comformal mapping between the physical domain of the hump and the rectangular computational domain. The method is described in context of the wall-mounted hump geometry, but it can be easily applied to many arbitrarily shaped domains.

A Schwartz-Christoffel mapping provides a conformal transformation from the upper half plane

to the interior of an arbitrary polygon defined by vertices $z_1 ... z_n$. Let the angles between each of the vertices in the polygon be $\alpha_1 ... \alpha_n$, and let $w_1 ... w_n$ define the pre-images of z. The Schwartz-Christoffel mapping, $z = S(w)$, is defined by its derivative,

$$\frac{dS(w)}{dw} = \prod_{i=1}^{n-1} (w - w_i)^{\alpha_i - 1}. \tag{2.14}$$

A sequence of transformations from the physical domain to the upper-half plane and subsequently the upper-half plane to a rectangular computational domain gives the full conformal mapping. In this case, the wall-mounted hump geometry was discretized into approximately 900 vertices and four more are added as corners of the computational domain. Although the derivative of the mapping is an analytic expression the mapping itself is calculated numerically using the Schwartz-Christoffel Toolbox for MATLAB [38].

The resulting physical domain is a 900-sided polygon whose derivative is piecewise continuous along the surface of the hump. Since the discontinuities are undesirable in the computation of the derivatives the contour line ϵ from the polygon boundary is chosen as the first point in the grid. If the value of ϵ is small enough then the mapping creates a smooth and very good approximation to the original wall-mounted hump coordinates. The value of epsilon chosen for this geometry is 1.0×10^{-3}.

Grid points are also clustered around areas of interest via another mapping from the uniform rectangular domain $\zeta = \xi + i\eta$ to a non-uniform rectangular domain $\zeta' = \xi' + i\eta'$ using the hyperbolic stretching function

$$\frac{d\xi'}{d\xi} = 1 + \frac{1}{2} \sum_{l=1}^{L} \left[1 + \tanh \left(\frac{\xi - \xi_l}{\delta_l} \right) \right] (a_l - a_{l-1}). \tag{2.15}$$

Each grid stretching location is defined by the set of constants ξ_l, a_l and δ_l.

2.3 Simulation Details for Wall-Mounted Hump

The grid and computational domain used for the LES simulations is given in figure 2.3 with every sixth grid point displayed. Current computations have 800 points in the streamwise direction, 160 in the wall normal direction and 64 points in the spanwise direction for a total of approximately 8.2 million points. The resolution at the point $x/c = -0.5$ on the wall is $\Delta x/c = 0.0094$, $\Delta y/c = 0.00087$, and $\Delta z/c = 0.0031$ in the streamwise, wall normal and spanwise directions, respectively, and a typical timestep is $\Delta t a_\infty/c = 0.00035$.

The domain size is $4.9c \times 0.909c \times 0.2c$ as illustrated in figure 2.2, which matches the experiments at LRCW but is shorter than the experimental domain in the spanwise and streamwise directions in order to reduce the computational cost. The height of the hump is approximately $0.12c$ at its maximum.

The Reynolds number of the simulations is 500,000 based on the chord and freestream velocity unless otherwise noted. Although the Reynolds number is lower than the test case at the LaRC workshop, it is within the range of Reynolds numbers investigated experimentally [20].

Simulations are run on the Army Research Lab's MJM cluster which has two dual-core 3.0GHz Intel Woodcrest processors per node connected with a DDR Infiniband internal network. On this architecture, an LES simulation utilizing 50 processors takes approximately 16 minutes to complete 100 timesteps using a constant Smagorinsky SGS model.

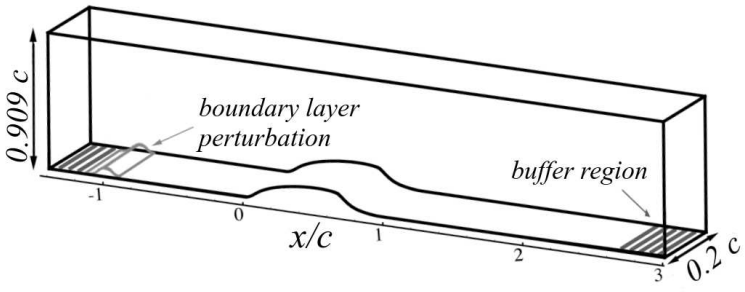

Figure 2.2: The LES computational domain.

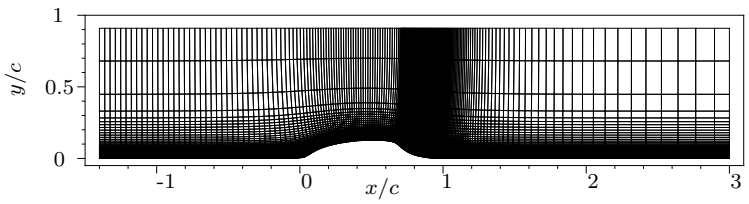

Figure 2.3: The computational grid (every sixth grid point plotted).

2.3.1 Initial and Boundary Conditions

The flow is initialized with a potential flow solution superimposed with a turbulent boundary layer profile on the lower wall. Since the primary goal of this work is to investigate the flow separation and reattachment downstream of the hump the inflow turbulent boundary layer is not fully resolved. Instead velocity perturbations, formulated with sums of random Fourier modes, are added in a Gaussian region close to the inlet. This approach has been used in previous studies [39, 28] to accelerate the development of a turbulent boundary layer. Details on the inflow noise perturbations can be found in Appendix B.

The average velocity profile of the computation at the inlet location of $x/c = -1.4$ is shown in figure 2.4 compared with the velocity profile obtained experimentally from Greenblatt et al. [20] at the upstream location $x/c = -2.14$. The boundary layer thickness in the present computations is smaller than the experiments, but it has been shown that the upstream boundary layer thickness at high Reynolds numbers has a minor effect on the flow [3].

The boundary conditions are periodic in the spanwise direction, no-slip and iso-thermal conditions on the lower wall boundary, and symmetry is imposed on the upper boundary. The inflow and exit boundaries have non-reflecting boundary conditions with a buffer zone that relaxes the flow towards the initial solution [40]. Figure 2.2 illustrates the extend of the buffer zone and inflow noise perturbations in the computational domain.

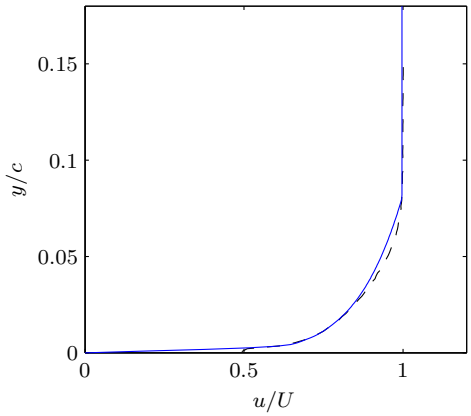

Figure 2.4: The inflow profile at x/c=−1.4 of the LES (solid line) compared with the experimental profile at x/c=−2.14 [20].

2.4 Control Implementation

Rather than model the flow field inside the actuation cavity of the experiment, the boundary conditions are modified at the wall to simulate the slot jet. This methodology has been successful in simulating the effects of the flow control cavity in other investigations [25, 41]. When actuation is applied, a normal velocity distribution is prescribed on the boundary nodes to approximate the same slot location and approximate slot width, h_s, as used in the experiments. The slot geometry and location from Greenblatt et al. [20] is shown in figure 2.5 with the slot region enlarged. Superimposed over the slot are the grid points that define the forcing width and location depicted as the positive normal velocity imposed during the blowing phase. The velocity at the wall is given by the Gaussian profile

$$u_s = u_{s,max} e^{-(x-x_s)^2/2\sigma^2}, \quad h_s = 4\sigma. \tag{2.16}$$

When steady suction actuation is applied the negated velocity profile in Eq. (2.16) is gradually turned on with the ramp function

$$r(t) = \frac{1}{2}\left(1 + tanh(3t - \frac{1}{2})\right). \tag{2.17}$$

For oscillatory forcing the normal velocity at the wall is actuated in time by $sin(\omega t)$ such that the mean slot velocity is zero. The steady suction controlled cases can be characterized by the mass-flux coefficient

$$C_m = \frac{\rho_s u_s h_s}{\rho_\infty U_\infty c} \tag{2.18}$$

and the steady momemtum flux coefficient

$$C_\mu = \frac{\rho_s u_s^2 h_s}{0.5 \rho_\infty U_\infty^2 c}, \tag{2.19}$$

both of which are calculated using the bulk slot velocity from Eq. (2.16). The non-dimensional parameters for the oscillatory control are defined by the unsteady momentum flux coefficient

$$\langle C_\mu \rangle = \frac{\rho_s \langle u_s \rangle^2 h_s}{0.5 \rho_\infty U_\infty^2 c} \tag{2.20}$$

and the reduced forcing frequency

$$F^+ = \frac{f X_{sep}}{U_\infty} \tag{2.21}$$

in which X_{sep} is $c/2$.

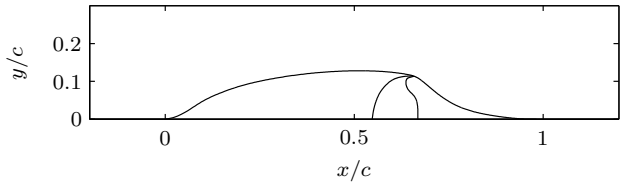

(a) experimental hump and control slot geometry

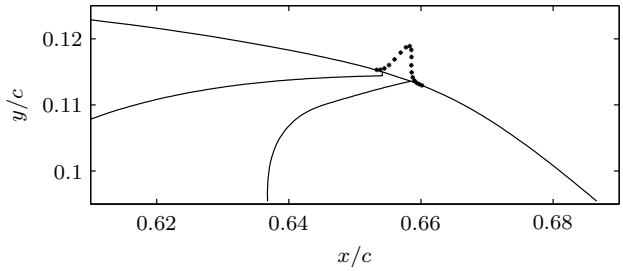

(b) prescribed velocity profile

Figure 2.5: The experimental hump configuration with an enlargement of the slot geometry and the prescribed Gaussian profile superimposed.

Chapter 3

LES Validation: Baseline and Controlled Flows

The large eddy simulation described in chapter 2 is validated using the low Mach number baseline and controlled wall-mounted hump flow corresponding to case three at the Langley Research Center Workshop (LRCW) on CFD Validation of Synthetic Jets and Turbulent Separation Control [19]. THe LES is also validated against the experimental data from Seifert and Pack [3], who have also performed detailed experiments of the wall-mounted hump flow in a separate wind tunnel facility. The low Mach number flow is simulated for the baseline or uncontrolled case, as well as steady suction and zero net mass flux oscillatory control at the non-dimensional forcing levels of the experiments. The effect of the LES model parameters on the baseline and turbulent quantities is investigated for the oscillatory controlled case.

3.1 Baseline Flow

The wall-mounted hump flow has been investigated by two separate experimental groups using separate wind tunnel facilities [3, 20]. Figure 3.1 shows the surface pressure coefficient at a low Mach number from each facility, demonstrating similar results throughout the separated region. The LRCW test case has a higher suction peak at mid-chord, which may be attributed to the lower wind tunnel height, creating more blockage. Another facility difference is accounted for by the endplates installed on the LRCW model. When the endplates were temporarily removed the

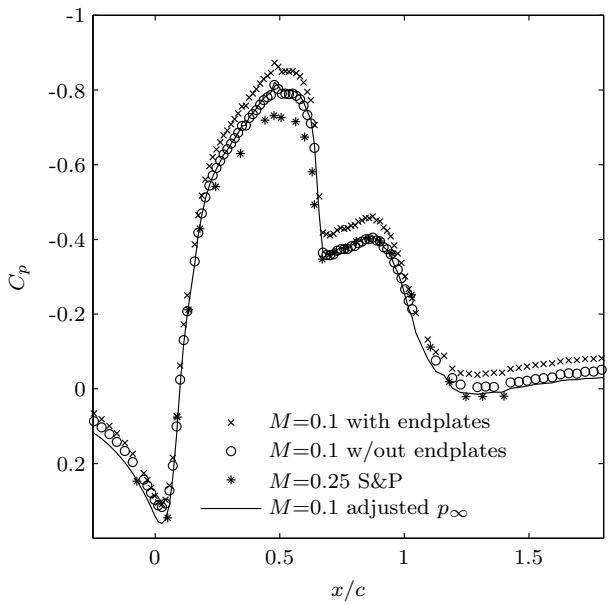

Figure 3.1: The surface C_p illustrating facility dependence between Seifert and Pack (S&P) ($M = 0.25$, $Re = 16 \times 10^6$) [3] and the LRCW ($M = 0.1$, $Re = 1 \times 10^6$) data with the effect of endplates [20].

new C_p curve was consistently a better match to the CFD results presented at the workshop [20]. Since the controlled cases are performed with endplates, corresponding experimental C_p results from Greenblatt et al. [20, 21] have been rescaled by increasing the reference pressure by 0.0365%. The effect of adjusting the C_p for the baseline case is shown in figure 3.1 along with the experimental data from Seifert and Pack [3]. The experimental data have shown that the separation and reattachment locations are relatively insensitive to Mach numbers in the range 0.1-0.25, Reynolds number above 517,000 (not shown) [20], and the wind tunnel model and facility.

The boundary layer accelerates over the leading edge of the hump with a small separation bubble at $x/c = 0$ and reaches a suction peak at $x/c \approx 0.5$, initiating pressure recovery. Recovery is hindered when the flow separates at $x/c \approx 0.66$, forming an unsteady separation bubble over the trailing edge. As the separated shear layer grows it is deflected towards the wall and eventually reattaches downstream of the hump geometry. For comparison, a fully attached flow over the hump geometry [3] has strong suction peak of $C_p = -1.6$ at $x/c \approx 0.65$ followed by a sharp recovery to $C_p = 0.5$.

The LES pressure coefficient of the baseline flow is given in figure 3.2 for a low Mach number

of $M = 0.25$ compared with experimental results. The LES maintains a good prediction of the separation behavior except for a slight over-prediction of the pressure coefficient within the separated region. The suction peak at mid-chord is also lower than in the experiments, but is not believed to significantly affect the separation dynamics. The averaged LES results show a small suction peak within the separated region at the same location as the experimental data, and the location of the final pressure recovery is also well predicted.

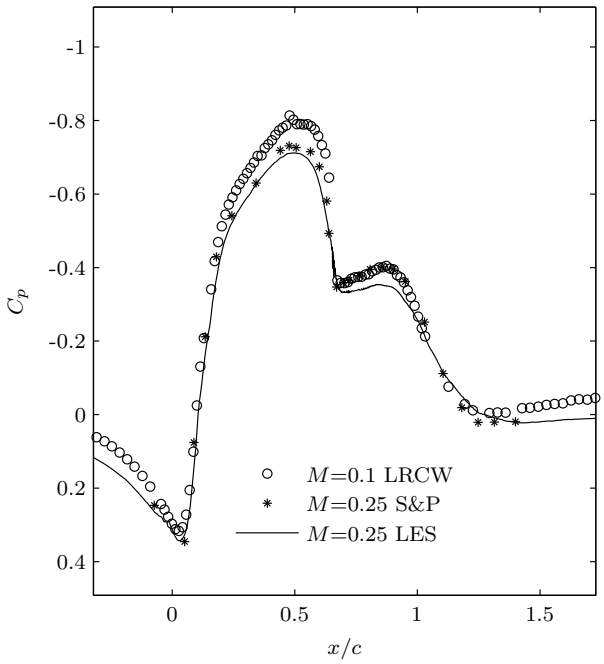

Figure 3.2: The baseline LES ($Re = 0.5 \times 10^6$) compared with experimental data from Seifert and Pack (S&P) ($M = 0.25$, $Re = 16 \times 10^6$) and LRCW ($M = 0.1$, $Re = 1 \times 10^6$) data [20].

The average streamlines for the LES and the PIV data (with endplates)[20] are plotted in figure 3.3. Comparing the average streamline corresponding to reattachment, the LES predicts a separation bubble approximately 7.3% larger than the experimental data at low Mach number, but the center and shape of the streamlines compares well with the experiment.

The time and span-averaged velocity profiles, $\bar{u}/U_\infty$ and $\bar{v}/U_\infty$, are plotted against the PIV data in figure 3.4 and show good agreement throughout the separated region for the low Mach number flow. The magnitude of the velocity in the reverse flow region is slightly under-predicted, which may indicate lower entrainment rates between $0.7 < x/c < 0.9$, which may cause the slightly

longer separation bubble in figure 3.3. The vertical component of velocity is negative above the reattachment region ($x/c \approx 1.1$), indicating that the average shear layer is deflected towards the wall. The experiments indicate a stronger negative vertical velocity in this region, perhaps indicative of a stronger downward deflection of the shear layer, causing an earlier reattachment.

The resolved Reynolds stresses of the LES are compared with experimental results in figure 3.5. The Reynolds stresses peak within the shear layer for both the experiment and LES curves, but the LES initially over-predicts the maximum values just after separation and under-predicts the peak values further in the separated region. Experiments indicate that the maximum Reynolds stress values occur within the shear layer, just before reattachment.

Figure 3.6 has average C_p data for other numerical simulations of the LRCW uncontrolled case compared with the current LES and the experimental data without endplates. LES models generally have a better prediction of the pressure coefficient compared with RANS-based models such as the unsteady RANS employed by Capizzano et al [42]. In addition, the current Smagorinsky based SGS model compares well with other implicit LES (ILES) [23] and LES utilizing a dynamic Smagorinsky SGS model [24, 25].

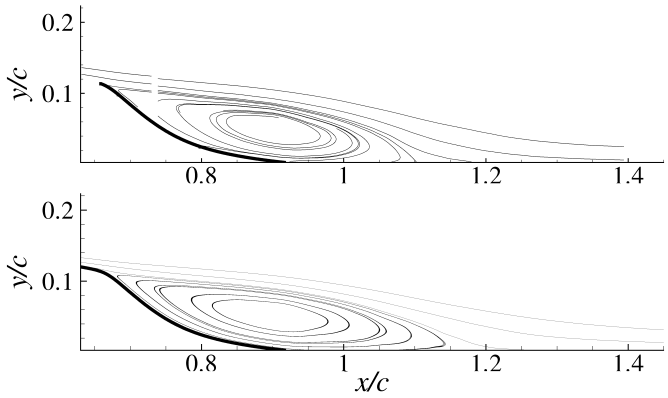

Figure 3.3: The averaged streamlines and from 2D PIV data at $M = 0.1$ [20] (top) and LES at $M = 0.25$ (bottom).

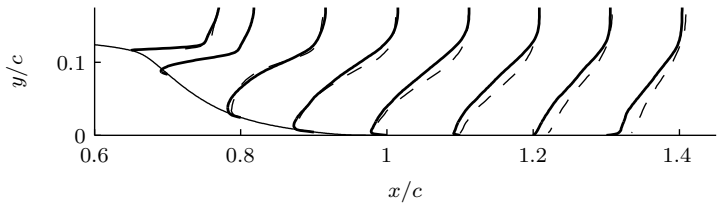

(a) $\bar{u}/U_\infty$ velocity profiles

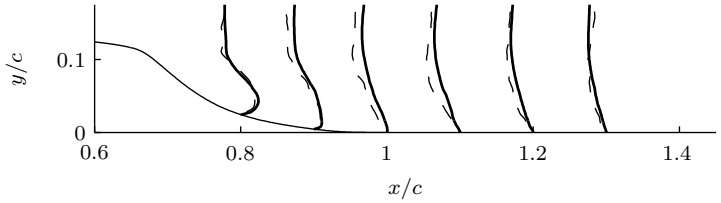

(b) $\bar{v}/U_\infty$ velocity profiles

Figure 3.4: Velocity profiles translated to corresponding locations on geometry, values of $\bar{u}$ scaled by 0.1 and $\bar{v}$ by 0.3 to fit all on the axis. Solid line is LES, dashed line is experimental PIV data [20].

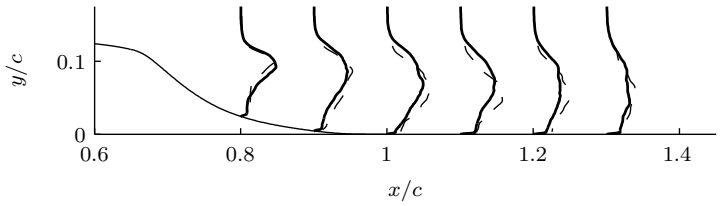

(a) $\overline{u'u'}$

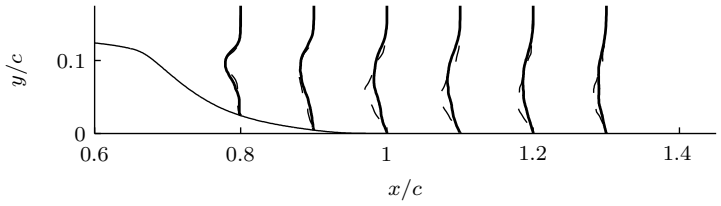

(b) $\overline{u'v'}$

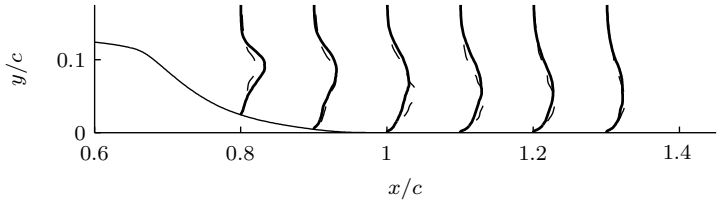

(c) $\overline{v'v'}$

Figure 3.5: Reynolds stress profiles translated to corresponding locations on geometry. Solid line is LES, dashed line is experimental PIV data [20].

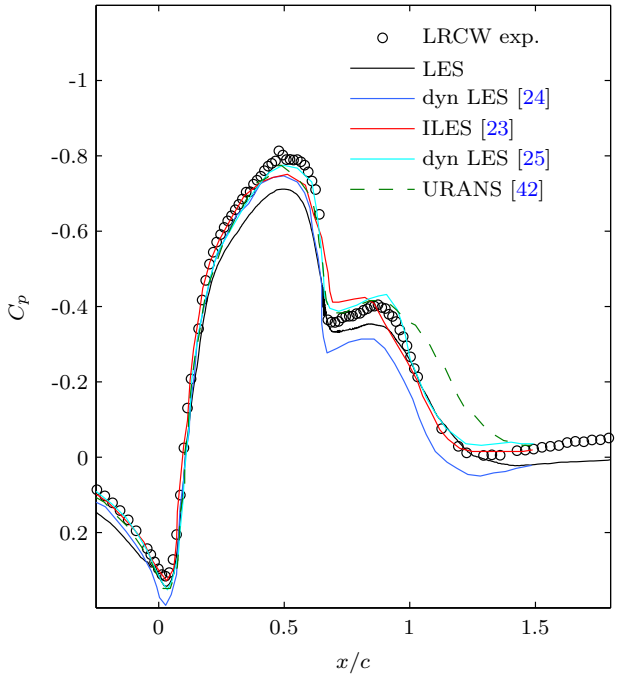

Figure 3.6: A comparison with other numerical simulations of the LRCW baseline flow.

3.2 Controlled Flow

In order to assess the LES as a predictive tool for flow control, steady suction and zero net mass flux oscillatory control is applied to the $M = 0.25$ flow and compared with experimental data.

3.2.1 Steady Suction Control

Steady suction control is applied just before natural separation, and has the effect of locally thinning the boundary layer and delaying separation. The slight separation delay keeps the flow attached longer over the highly convex region of the hump ($x/c \approx 0.67$). This deflects the shear layer downward and forms a smaller recirculation bubble, significantly decreasing the form drag.

The effect on the pressure coefficient is shown in figure 3.7. The control creates a steep suction peak that closely resembles the attached flow, but still creates a small turbulent separated region that reattaches around $x/c = 0.94$. The LES is compared with two sets of experimental data in figure 3.7 of similar C_m values, showing excellent C_p agreement at separation and reattachment.

The LES control parameters match the C_m values of the experiment, but have a lower C_μ value due to the larger slot width of the computational model. Since the slot width differs from that in the experiments, it is impossible to match both the experimental C_m and C_μ values simultaneously.

The average streamlines are shown in figure 3.8 compared with the 2D PIV data, and show a good prediction of average separation and reattachment. The separation bubble length is 2.2% longer than that determined from the experimental PIV data. Figure 3.9 displays the average velocity profiles for the steady suction case, which are well predicted in the reverse flow region ($x/c = 0.8$), as well surrounding reattachment ($x/c \approx 1.0$).

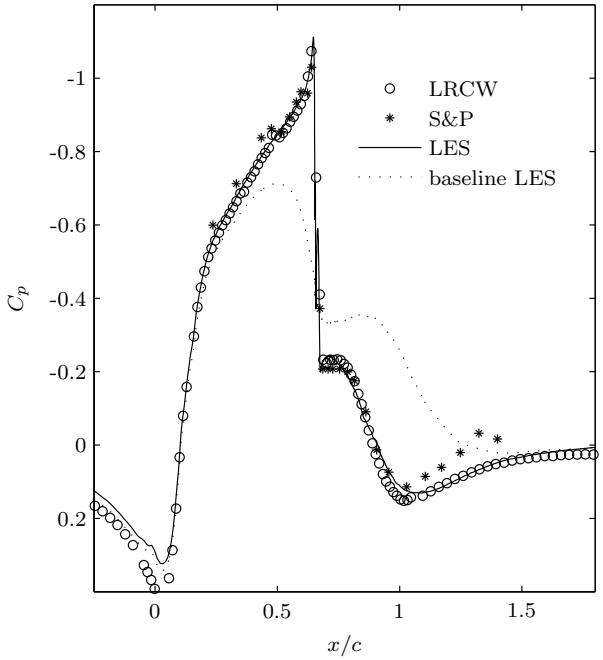

Figure 3.7: Steady suction surface pressure coefficient at low Mach number of experimental data from LRCW ($M = 0.1$, $C_m = 0.15\%$, $C_\mu = 0.24\%$), Seifert and Pack ($M = 0.25$, $C_m = 0.18\%$, $C_\mu = 0.25\%$), and LES ($M = 0.25$, $C_m = 0.15\%$, $C_\mu = 0.11\%$).

3.2.2 Oscillatory Control

Oscillatory forcing just before the separation point has been experimentally shown to decrease the size of the separated region, and if enough momentum is added, decrease the drag on the model [21]. The alternating blowing and suction do not delay separation, but rather form large-scale vortices

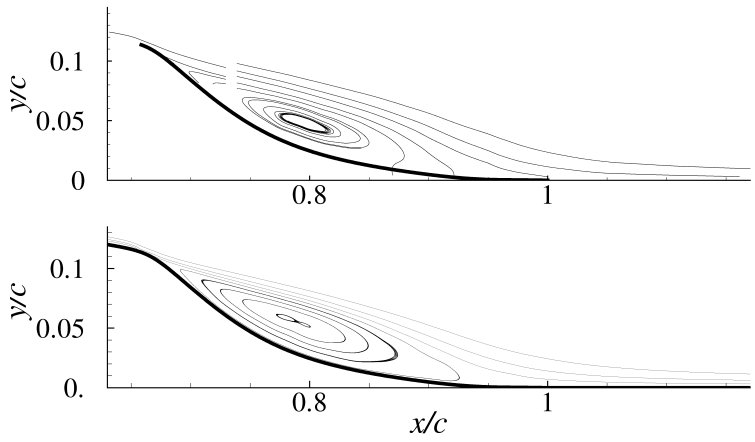

Figure 3.8: Steady suction averaged streamlines of 2D PIV data from LRCW (top) and LES (bottom), control parameters are the same as figure 3.7.

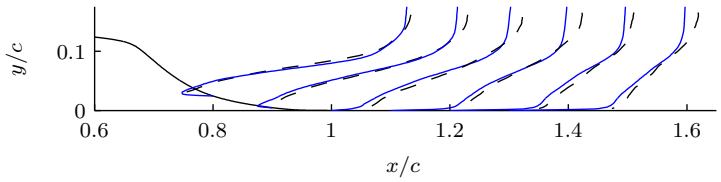

(a) $\bar{u}$ velocity profiles

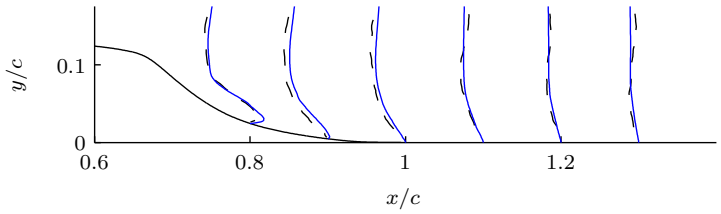

(b) $\bar{v}$ velocity profiles

Figure 3.9: Velocity profiles of steady suction controlled flow, translated to corresponding locations on geometry, values of $\bar{u}$ and $\bar{v}$ scaled by 0.3 to fit all on the axis. Solid line is LES, dashed line is experimental PIV data [20].

that accelerate the flow's reattachment to the wall.

Figure 3.10 shows the experimental data compared with the LES low Mach number flow forced at $F^+ = 0.84$. The LES C_p predictions are overall not as accurate as the steady suction results. However, the oscillatory flow has been more difficult to accurately predict than the baseline or steady suction cases [23, 24]. The two sets of experimental results also have a different C_p behavior just after separation, indicating that the vortex dynamics within $0.66 < x/c < 0.90$ may be very sensitive to the slot geometry or slot thickness. Despite the discrepancy in C_p just after separation, the average separation bubble length is only slightly over-predicted by the LES, which is similar to the baseline results.

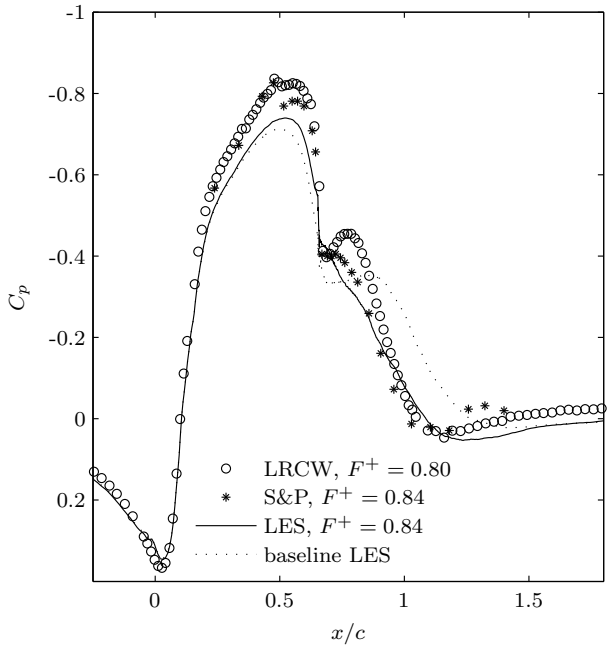

Figure 3.10: Oscillatory controlled averaged surface pressure coefficient for low Mach number from LRCW ($M = 0.1$, $C_\mu = 0.11\%$), Seifert and Pack ($M = 0.25$, $C_\mu = 0.13\%$), and LES ($M = 0.25$, $C_\mu = 0.11\%$)

A qualitative comparison with the phase-averaged PIV spanwise vorticity contours is given in figure 3.11 where a phase of 90° corresponds to the peak blowing cycle and a phase of 270° corresponds to the peak suction cycle. The phase-averaged data agrees well with the experiments, indicating the correct size as the vortex convects downstream and dissipates. The vortex core has slightly higher vorticity levels in the LES results but it dissipates rapidly as it is convected downstream, and

beyond $x/c = 0.8$ the levels of vorticity agree very well with the experimental data including the region surrounding reattachment.

The steady suction and oscillatory control cases demonstrate improved C_p results from a previous ILES [26] due to less numerical dissipation and the addition of constant Smagorinsky model terms for the subgrid scale stress tensors, as well as an improvement in the stability and robustness of the solver. Parameters such as the control slot size/geometry, grid resolution, and the LES model including numerical dissipation may further improve the C_p prediction of the oscillatory control.

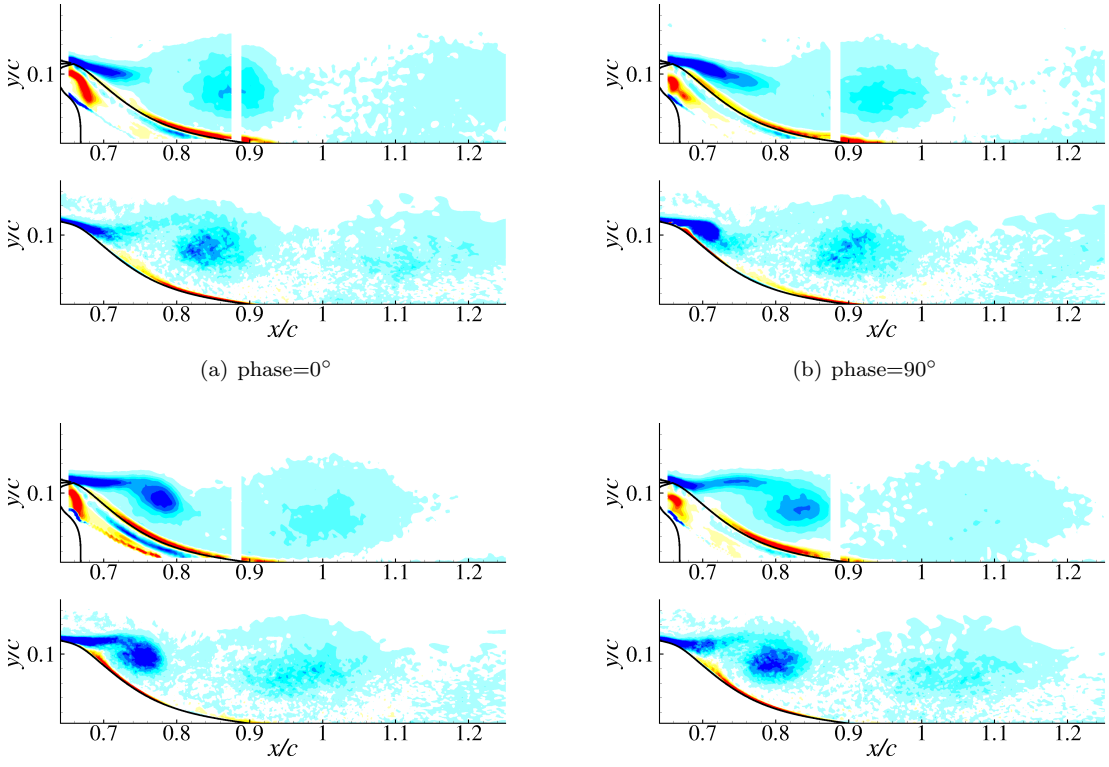

(a) phase=0°

(b) phase=90°

(c) phase=180°

(d) phase=270°

Figure 3.11: Phase-averaged spanwise vorticity contours of 2D PIV data (top) and LES (bottom). Shown are 15 contour levels from -70 to 70.

3.3 Effect of LES Parameters

Three test cases are devised to test the effect of the Smagorinsky SGS model and explicit filtering. The oscillatory forced flow is used for the test cases since it is the most difficult to accurately model. All are performed at low Mach number to enable comparison with the LRCW data. Case A

refers to the constant Smagorinsky model presented in the previous section with a sharp cutoff filter ($\alpha_f = 0.49$ in figure 2.1) in the wall-normal and spanwise directions. Case B has the same filter, but the SGS constants are set to zero (ILES). Case C is also an ILES but with a more aggressive filter ($\alpha_f = 0.35$ in figure 2.1) applied in all three spatial directions.

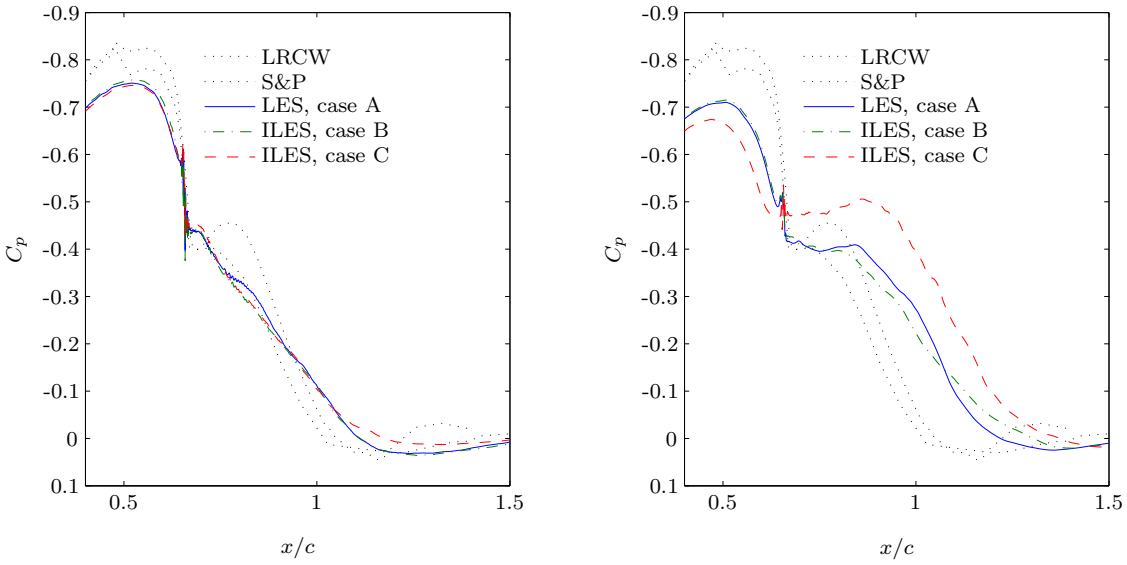

(a) LES grid size: $800 \times 160 \times 64$

(b) LES grid size: $400 \times 80 \times 32$

Figure 3.12: The time and span-averaged C_p of three LES test cases.

The time and span-averaged pressure coefficients are shown in figure 3.12, and indicate only small differences between the three cases. The constant Smagorinsky has the best approximation of the pressure within the average separation region due to a slight suction peak at $x/c \approx 0.8$. Comparing the two ILES, more filtering delays pressure recovery in the reattachment region. The small differences may indicate the flow is already well resolved by the grid, thus each test case is also run on a lower resolution grid of $400 \times 80 \times 32$. The lower resolution averaged C_p results clearly show an increased suction peak within the separated region followed by an earlier reattachment when the Smagorinsky model is added. With more aggressive filtering, the mean pressure coefficient is shifted throughout the domain, and reattachment is delayed. Therefore, increasing the filter width, or filtering larger scales, is similar to a reduction in grid resolution.

Perturbations in the forced flow are due to the large scale coherent motion of the vortex shedding

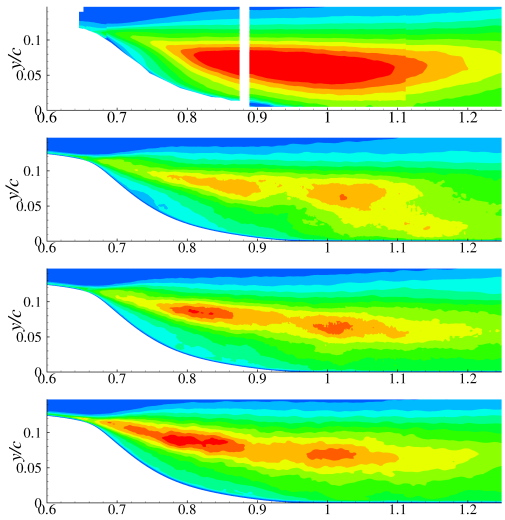

(a) $\overline{\langle u'u' \rangle}$, contour levels: 0 to 0.06.

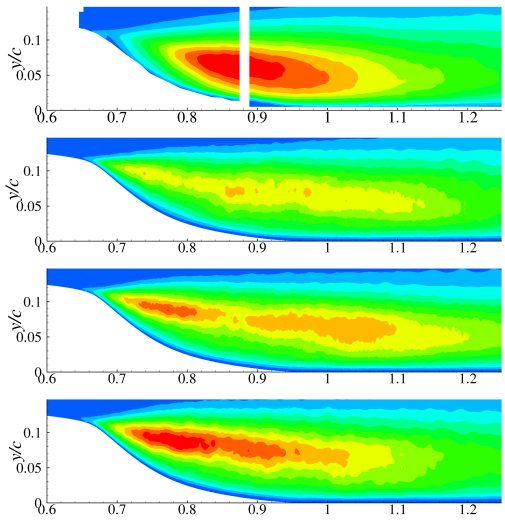

(b) $\overline{\langle v'v' \rangle}$, contour levels: 0 to 0.055.

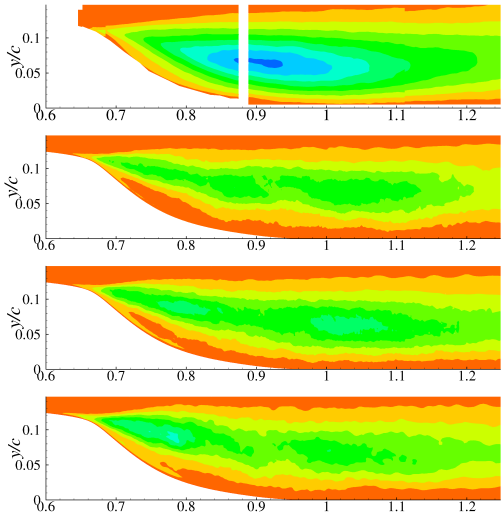

(c) $\overline{\langle u'v' \rangle}$, contour levels: -0.45 to 0.

Figure 3.13: Turbulent Reynolds stresses, from top to bottom: experimental PIV results, case A, case B, and case C.

as well as the turbulent fluctuations. In order to isolate the turbulent quantities, the perturbations $\langle q' \rangle$ are calculated from the phase-averaged $\langle q(x,y) \rangle$ states. The perturbations from the various phases are then averaged to obtain $\overline{\langle q' \rangle}$. The resolved Reynolds stresses of $\overline{\langle u'u' \rangle}$, $\overline{\langle v'v' \rangle}$, and $\overline{\langle u'v' \rangle}$ are shown in figure 3.13 for the three test cases compared with the experimental PIV results.

The LES and ILES results generally have lower Reynolds stresses than the experimental data, however since the Reynolds number is a factor of two lower than the experiments, a qualitative comparison is sought. Case A, representing the addition of the Smagorinsky SGS terms from the ILES of case B, has a reduced magnitude of $\overline{\langle u'u' \rangle}$ and $\overline{\langle v'v' \rangle}$ across the middle of the separated shear layer. This reduction gives a better prediction in $0.65 < x/c < 0.8$ which is the region associated with vortex roll-up and growth. Case A also has a better prediction of the peak value of $\overline{\langle v'v' \rangle}$, around $x/c \approx 0.9$, resulting in good qualitative agreement in the center of the pressure recovery region. The more aggressive filter of Case C increases the values of $\overline{\langle u'u' \rangle}$ and $\overline{\langle v'v' \rangle}$, leading to over-predicted values through the vortex roll-up and growth region and maxima values further upstream, closer to separation.

The LES results are also compared with the compressible ILES of Morgan et al., who computed the baseline and forced cases at a Reynolds number of 200,000, with 20.3 million grid points defining the external flow and another 900,000 grid points modeling the flow in the control cavity. Since the forced flow was over-predicted at the test case C_μ, a higher coefficient was also modeled to show similar trends with the experiment [23]. The Smagorinsky LES presented in this thesis ($Re = 500,000$, 8.2 million grid points) provides a more accurate prediction of the reattachment location for the LRCW test case baseline and controlled flows at lower computational cost. A comparison of the pressure coefficients is shown in figure 3.14. It is noted that there is a discrepancy in Reynolds number which may account for the increase in separation bubble length for the ILES [23], but experimental results have shown only a slight dependence on Reynolds number between 371,600 and 1.11×10^6 for the baseline flow, and between 577,400 and 1.11×10^6 for the oscillatory forced flow [21].

It is also noted that modeling the flow control cavity does not have a significant effect on the

average pressure coefficient with the separated region. The ILES high C_μ case with the cavity flow modeled [23] displays a similar qualitative behavior to the current LES in figure 3.12. Therefore the current slot model of imposing a wall velocity is not believed to be directly related to the under-prediction of the suction peak within the separated region.

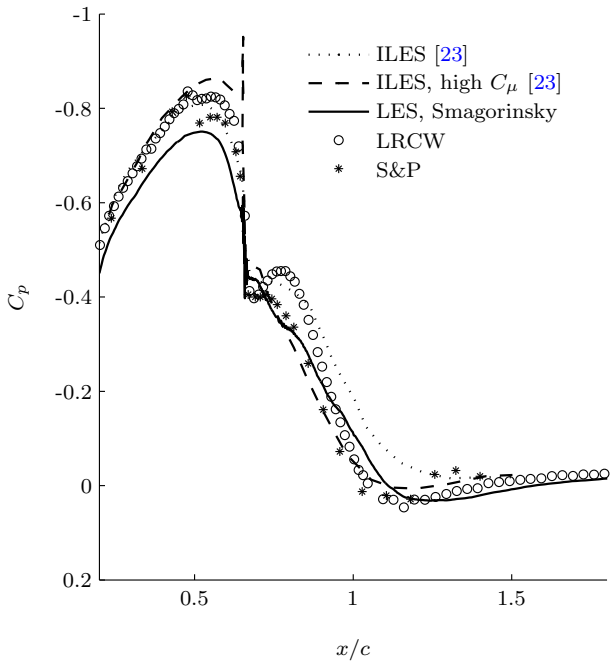

Figure 3.14: A comparison with the oscillatory forced cases of Morgan et al. [23].

Chapter 4

Flow Structure and the Effects of Compressibility

The effects of compressibility on the wall-mounted flow have been experimentally investigated by Seifert and Pack, who performed baseline experiments for $0.25 \leq M \leq 0.7$ [17]. They discovered that a shock wave exists at separation for the baseline flow at $M \geq 0.65$. They applied steady suction and oscillatory control at $M = 0.65$, and found that the control effectiveness is decreased in the presence of shocks.

The current computational scheme is not well-suited for shock-capturing, and thus compressibility is investigated at a high subsonic Mach number of 0.6. The baseline flow is validated against experimental data, and the flow physics are discussed and compared with the low Mach number results from Chapter 3. Steady suction and oscillatory control are also applied at $M = 0.6$, which provide insight into the compressibility effects on control without the presence of shocks.

4.1 Baseline Flow

4.1.1 Time and Span-Averaged Flow

The baseline wall-mounted hump flow is investigated at $M = 0.6$ and compared against experimental data in figure 4.1(a). As the Mach number increases, the flow has a greater acceleration over the leading edge resulting in a stronger suction peak at mid-chord. According to experiments by Seifert and Pack [17], at $M \geq 0.65$ the suction peak moves downstream and the flow becomes supersonic

at the suction peak, creating a shock wave in the pressure recovery region around $x/c = 0.65$.

The baseline flow at $M = 0.6$ remains subsonic around the suction peak, and the pressure recovery begins at the same location as the low Mach number flow. Recovery is hindered by separation at $x/c \approx 0.65$, the same location as the low Mach number flow, but at a lower C_p value. The most notable feature of the higher Mach number flow is the delayed reattachment and larger separation bubble. Figure 4.1(b) plots the C_p normalized by the pressure coefficient at separation, which shows the delay in pressure recovery at the higher Mach number. The larger separation region is likely due to the decreased growth and lower entrainment rate of the compressible shear layer.

The LES captures the main effects of compressibility but over-predicts the pressure recovery location with less accuracy than the lower Mach number case. This may be partially due to sparser grid resolution at the high Mach number reattachment location, since the same grid is utilized for both cases and was optimized for the low Mach number flow. Another possibility is that the height of the top wall may have more impact on the compressible flow than it does on the low Mach number flow. The height of the top wall, $H/c = 0.909$, is matched to the LRCW experiments, where the higher Mach number experiments of Seifert and Pack have a wall of height $H/c = 1.48$.

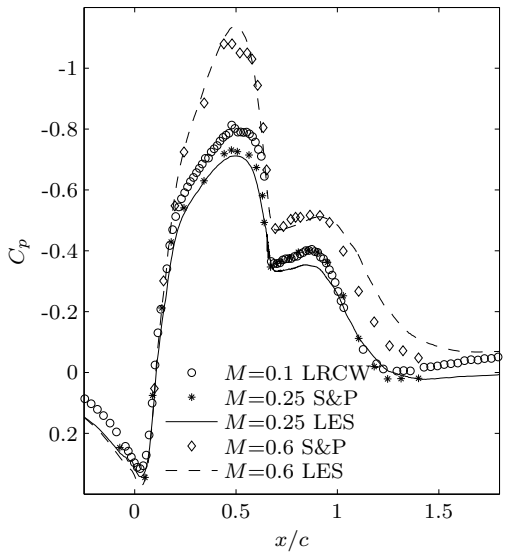

(a) C_p validation

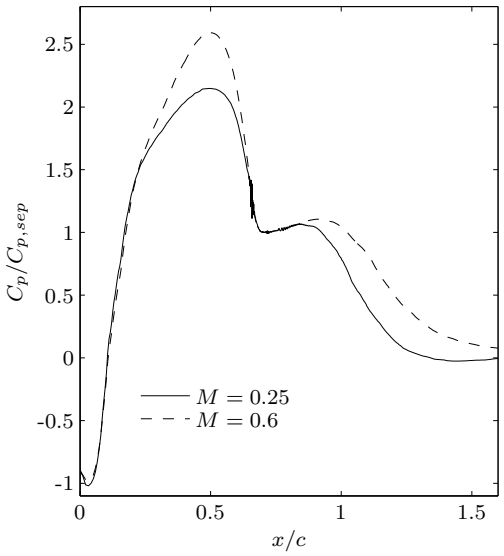

(b) C_p normalized by $C_{p,sep}$ for $M = 0.25$ and $M = 0.6$.

Figure 4.1: Pressure coefficients of $M = 0.25$ vs. high $M = 0.6$ baseline flow.

The average streamlines in figure 4.2 show the increased separation bubble length for the $M = 0.6$ flow, which is consistent with the delayed pressure recovery in figure 4.1(b). Comparing the average streamline corresponding to reattachment, the higher Mach number flow has a separation bubble length 9.3% larger than the low Mach number flow. The center of the separation bubble has shifted downstream from $x/c = 0.9$ to $x/c = 0.95$, which is also seen in the normalized C_p, where the separation region's suction peak is shifted downstream for the $M = 0.6$ case.

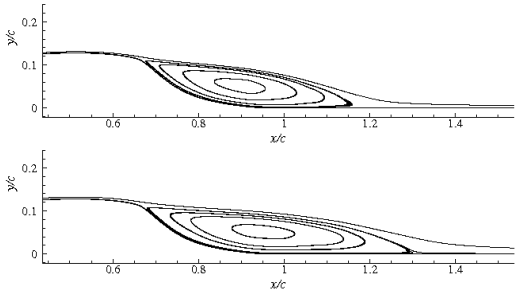

Figure 4.2: The averaged streamlines at $M = 0.25$ (top) and $M = 0.6$ (bottom).

The average u/U_∞ and v/U_∞ velocities are given in figure 4.3. The $M = 0.6$ flow has higher u/U_∞ velocities above the hump and separation bubble due to compressibility. The high Mach number flow also has weaker negative v/U_∞ (downward) velocities above the entire separation region, which could indicate that the freestream fluid is being entrained into the shear layer at a lower rate.

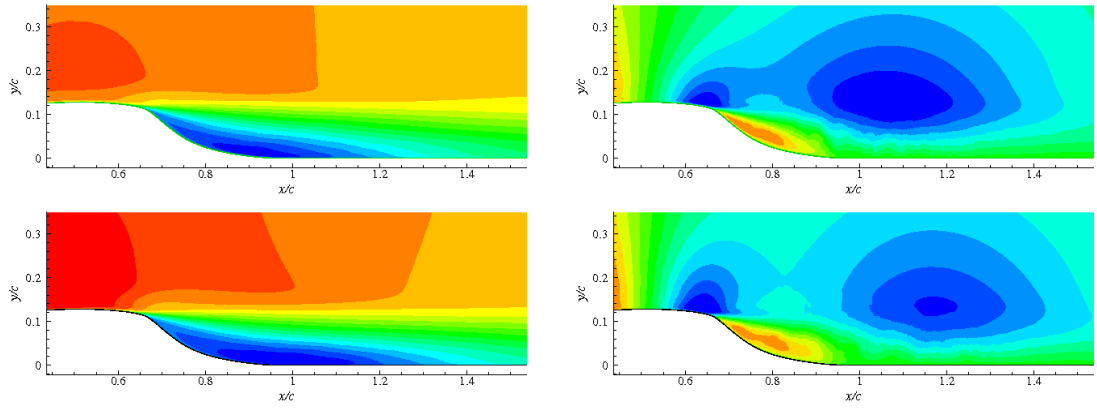

Figure 4.3: The average u/U_∞ (left) and v/U_∞ (right) velocity contours at $M = 0.25$ (top) and $M = 0.6$ (bottom). u/U_∞ contours from -0.2 to 1.3, v/U_∞ contours from -1 to 1.

4.1.2 Shear Layer Growth Rate

In order to investigate the growth rate of the separated shear layer, the vorticity thickness is calculated using

$$\delta_\omega(x) = 1/|\frac{d(u(x)/U_\infty)}{dy}|_{max} \tag{4.1}$$

for the time and span-averaged baseline flow. The vorticity thickness throughout the separation region is plotted for the $M = 0.25$ and $M = 0.6$ flows in figure 4.4(a) against the spatial coordinate x/c. The vorticity thickness is plotted in figure 4.4(b) using the local velocity difference $\Delta U(x) = u(x)_{max} - u(x)_{min}$ instead of U_∞ as the reference velocity, which Castro and Hague [4] found to better collapse the experimental data.

The centerline of the mean shear layer is curved, and follows the dividing streamline that separates the recirculating flow from the freestream in figure 4.2. However, the curved coordinate system associated with the shear layer growth is closely approximated by x/c.. Furthermore, measuring the growth rate with x/c provides a better comparison with previous investigations, including free shear layers.

In a free shear layer the spatial growth rate $d\delta_\omega(x)/dx$ is linear, and depends on the velocity ratio between the upper and lower freestream [43, 44]. Due to the presence of the wall, the growth rate in the shear layer separated from the hump is linear immediately after separation and decreases steadily until reattachment where it increases again. The same trend is found in other bounded and recirculating shear flows [4].

Compressible free shear layers are known to have a reduced growth rate with respect to incompressible flow. The reduction in growth rate scales with the convective Mach number M_c [45], defined by

$$M_c = \frac{U_1 - U_2}{a_1 + a_2}. \tag{4.2}$$

or with the compressibility parameter Π_c proposed by Slessor et al. [46],

$$\Pi_c(a_2 = a_1, \gamma_1 = \gamma_2) = \sqrt{\gamma_1 - 1}M_c. \tag{4.3}$$

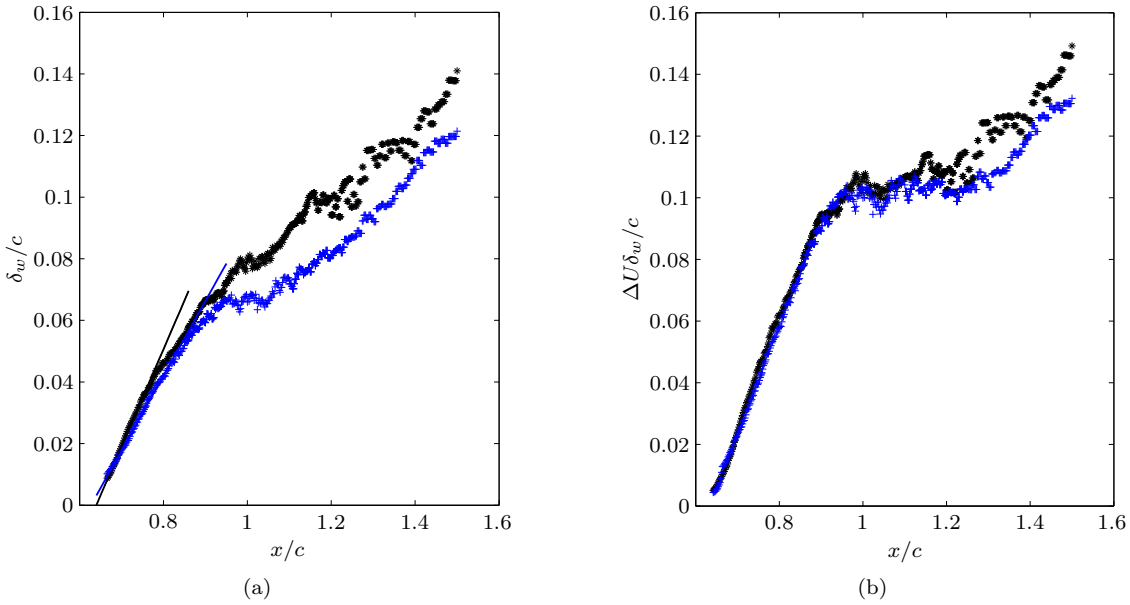

Figure 4.4: Vorticity thickness with (a) a linear fit through $0.6 < x/c < 0.8$ and (b) scaled by ΔU(x).

The definition of Π_c given by Eq. (4.3) assumes a density ratio of unity. Plotting the normalized growth rate against the compressibility parameter Π_c, Slessor et al. found the expression

$$\frac{\delta'_w}{\delta'_{w,0}}(\Pi_c) = (1 + \alpha\Pi_c^2)^{-\beta}, \qquad \alpha \simeq 4, \beta \simeq 0.5 \tag{4.4}$$

to be a good representation of the reduction in growth rate due to compressibility. In Eq. (4.4), $\delta'_w = d\delta_\omega(x)/dx$ and the subscript $_0$ denotes the incompressible growth rate.

Using the maximum velocity at separation PI_c is calculated for the $M = 0.25$ and $M = 0.6$ flows, along with the normalized growth rate from Eq. (4.4). A linear fit to the initial vorticity thickness immediately after separation in the region $0.67 < x/c < 0.80$ is performed to obtain an estimate of the initial growth rate. The fitted line is plotted in figure 4.4(a) and the slope of the line is tabulated in Table 4.1. From Eq. (4.4), the ratio of the high to low Mach number growth rates is 0.75. The ratio of the initial slopes from figure 4.4(a) is 0.77, agreeing well with the free shear layer prediction. Therefore, at least initially after separation, the effects of compressibility on the separated shear layer's growth rate agrees well with that of a free shear layer. The initially slower growth likely leads to less entrainment and thus the shear layer's deflection towards the lower wall

is delayed, resulting in a larger separated region.

Table 4.1: Comparison of growth rates for low and high Mach number flow.

M_∞	M_c	Π_c	δ'_w/δ'_{w0} (Eq. 4.4)	δ'_w/c (linear fit)
0.25	0.15	0.19	0.95	0.316
0.6	0.385	0.49	0.71	0.243

Compressibility has also been shown to reduce turbulent fluctuations and the production of turbulent kinetic energy [47], thus lower Reynolds stress values are expected in the higher Mach number shear layer. Since the inflow boundary layer noise perturbations are greater in the higher Mach number simulation, the resolved Reynolds stresses are plotted in figure 4.5 normalized by the maximum value within the boundary layer just before separation. Comparing the lower and higher Mach number Reynolds stresses, the lower Mach number has a stronger increase in fluctuations just after separation as well as in the reattachment region.

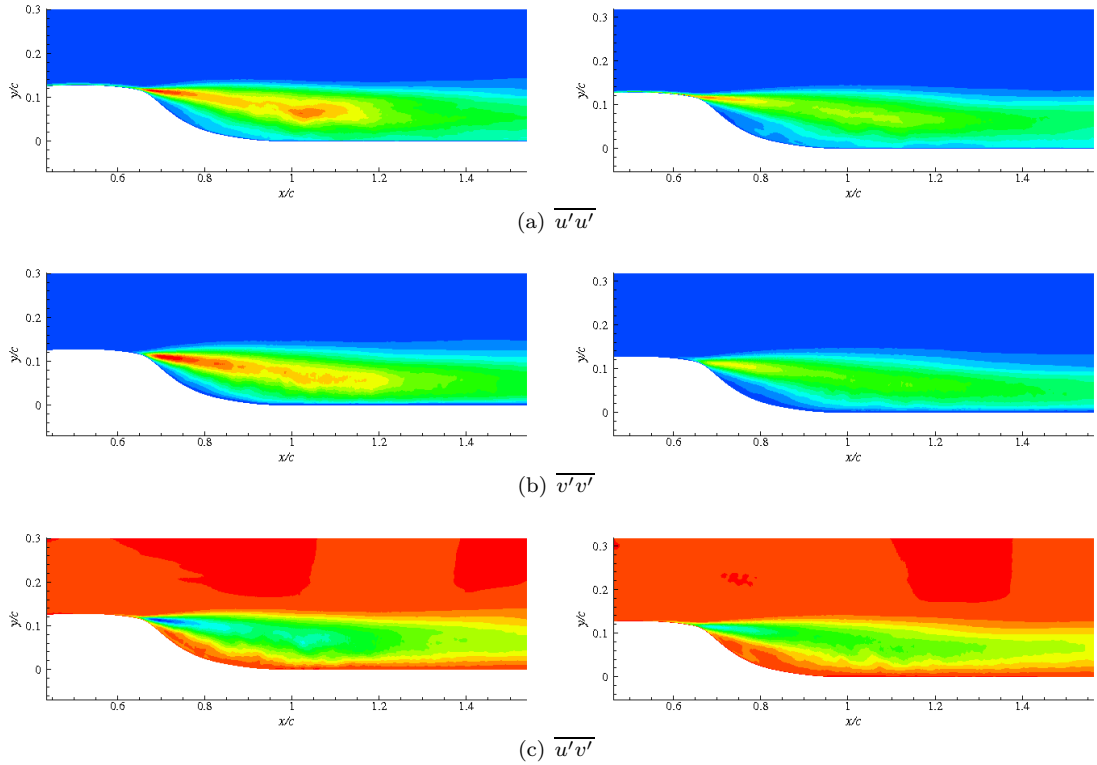

(a) $\overline{u'u'}$

(b) $\overline{v'v'}$

(c) $\overline{u'v'}$

Figure 4.5: The resolved Reynolds stresses, scaled by the maximum value in the boundary layer just before separation. Left: $M = 0.25$, Right: $M = 0.6$. 15 contour levels from a) 0 to 1.2, b) 0 to 3, and c) -1.8 to 0.

4.1.3 Unsteady Flow Characteristics

The turbulent separation bubble is highly unsteady and there is evidence of large scale structures formed inside the bubble that are shed downstream aperiodically. Contours of vorticity from the wall and one spanwise plane are shown with pressure iso-surfaces in figure 4.6. The isosurfaces highlight the shift in scale from small three-dimensional structures in the turbulent boundary layer to a larger unsteady structure within the separated region. These larger structures are approximately the height of the hump and often span across the geometry's width. After they are shed from the separation bubble, they convect downstream and dissipate rapidly.

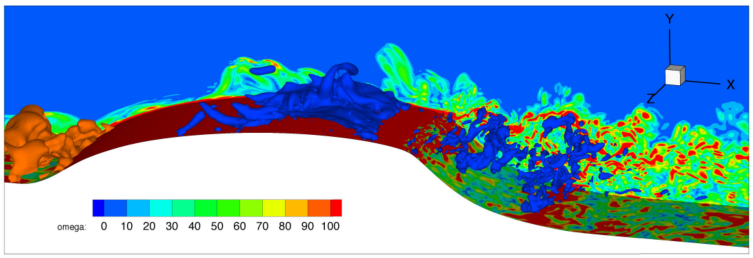

Figure 4.6: Isosurfaces of pressure superimposed with contours of vorticity, $|\omega|$ in one spanwise plane for the baseline flow at $M = 0.25$.

Figure 4.7 shows contour values of instantaneous pressure coefficient at mid-span for the $M = 0.25$ and $M = 0.6$ flows. The pressure coefficient has been normalized by the average C_p at separation, or $C_{p,sep}$, to enable a better comparison. A large scale structure is often present just before reattachment, indicating it may be an important factor to increasing fluid entrainment. The presence of the large scale structure gives rise to a local suction peak within the separated region seen in figure 4.1(a). Although this is seen in both the $M = 0.6$ and $M = 0.25$ cases, the low pressure region is shifted downstream in the $M = 0.6$ flow indicative of the larger separated region.

Pressure and velocity probes are placed within the shear layer and along the wall of the separation region, and spectra are computed at various locations depicted in figure 4.8. In figures 4.9(a) and 4.9(b), 32 spectra from equally spaced planes in the spanwise direction are taken at the locations of probes $s1$, $s3$, $s4$, $s5$, and $s6$. The spectra of each corresponding (x, y) location are averaged and plotted in figures 4.9(a) and 4.9(b), spaced one decade apart for comparison on one plot.

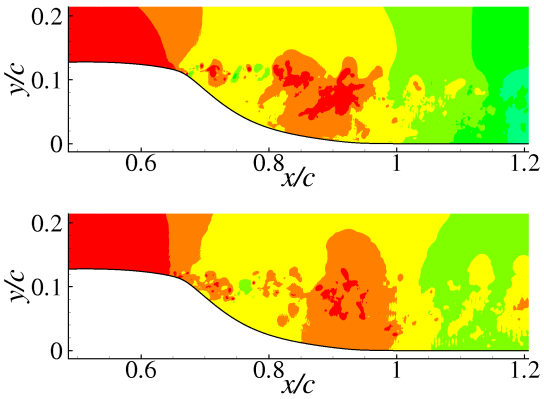

Figure 4.7: The instantaneous pressure coefficient normalized by $C_{p,sep}$ at mid-span for $M = 0.25$ (top) and $M = 0.6$ (bottom). 8 contour levels from -1 to 1.5.

Figure 4.9(a) contains the spectra of the low Mach number flow. Probe $s1$ has low frequency peaks around $F^+ = 0.5$ and 1.5, but also has activity at frequencies centered around $F^+ = 6$ and $F^+ = 11$, which are likely due to higher frequency shear layer or Kelvin-Helmholz type instabilities. The higher frequencies are not very detectable at later points in the separation bubble as the low frequency components grow in strength. At probes $s3$ and $s4$ there is a peak at $F^+ = 0.8$, and growth for a range of low frequencies $F^+ < 5$ in the middle of separation bubble. Towards the end of the separated region, the peaks have decreased to $F^+ = 0.5$ at probe $s5$ and $F^+ = 0.25$ at probe $s6$. The spectra for the higher Mach number flow are given in Figure 4.9(b) where similar trends are observed. The initial shear layer at probe s1 has a broad range of frequencies, with growth of the low frequencies $F^+ < 3$ at probe $s3$. Low frequency peaks emerge at $F^+ = 0.5$ at probe $s5$ and $F^+ = 0.25$ at probe $s6$.

The shift to lower frequencies is also seen in experimental data of the hump flow [48], where a broadband peak centered around $F^+ = 0.8$ early in the separation is reduced to $F^+ = 0.4 - 0.5$ downstream. The decrease in frequency could be due to vortex merging within the separation region. The results are consistent with other reattaching flows, which have found natural shedding frequencies between $0.5 < F^+ < 0.8$ [1].

Nondimensionalizing the frequency by the separation bubble height, $h_b = 0.12c$, and the velocity at separation, $u_{sep} = 1.2U_\infty$, the frequency $F^+ = 0.8$ is equivalent to $fh_b/u_{sep} = 0.08$. This is the

universal value suggested by Sigurdson [7] for reattaching flows, and as Sigurdson noted, the same as the universal bluff body shedding frequency originally proposed by Roshko. In bluff body separation, alternating vortex signs are shed from the top and bottom surfaces, which interact with one another in the wake forming a Kármán vortex street. In a wall-bounded reattaching flow, vortices of one sign are formed at separation, but Sigurdson hypothesizes that they could interact with their images from the wall, producing a similar frequency as found in bluff body separation.

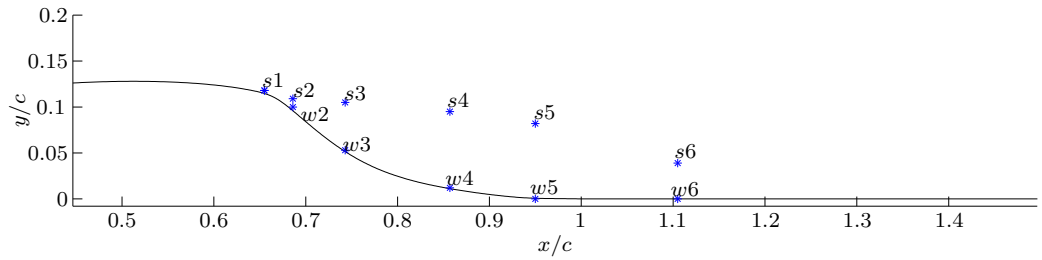

Figure 4.8: Locations of probes placed in the shear layer and along the wall. In increasing order, probes are at $x/c = 0.65, 0.68, 0.74, 0.86, 0.95, 1.10$.

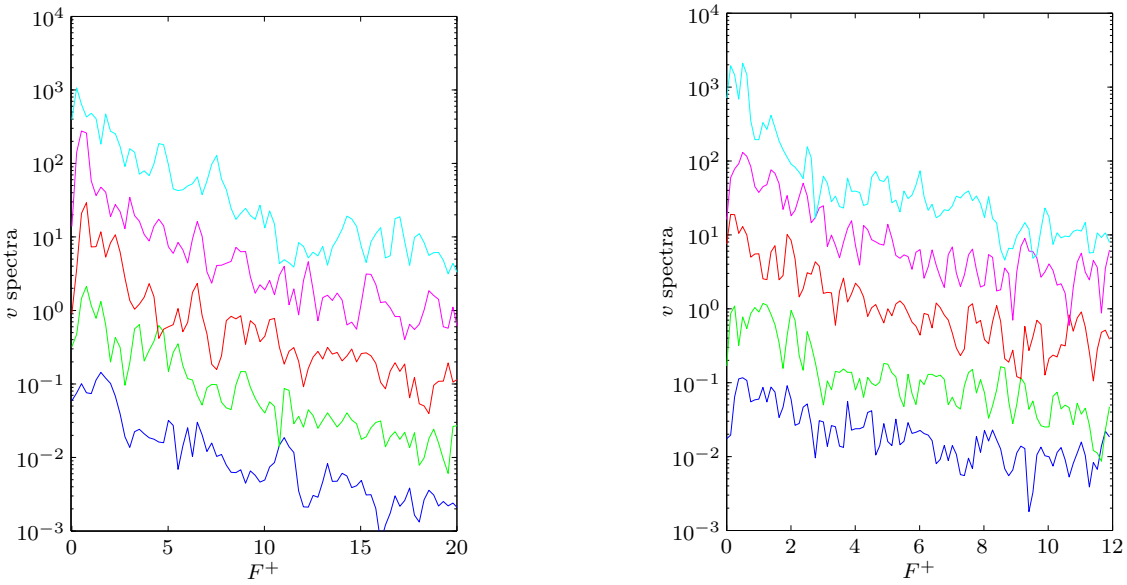

(a) $M = 0.25$ (b) $M = 0.6$

Figure 4.9: Averaged spectra of 32 locations along the span. From bottom to top, v/U_∞ probes at $s1$, $s3$, $s4$, $s5$, $s6$ are plotted one decade apart for better viewing.

4.2 Controlled Flow

4.2.1 Time and Span-Averaged Flow

The pressure coefficient for the steady suction controlled case at $M = 0.6$ is shown in figure 4.10(a) compared with the $M = 0.25$ flow controlled at the same C_m. The pressure profile of the higher Mach number steady suction shows a broader low pressure suction peak across the top surface of the hump geometry in comparison with the sharp peak of the low Mach number case. Both the low and higher Mach number flows initiate a strong pressure recovery in the location immediately after control, but is still hindered by a separation bubble over the trailing edge, similar to that of the baseline flow.

Steady suction control applied just before natural separation has the effect of locally thinning the boundary layer and delaying separation. The delay of separation and deflection of the mean streamlines is shown in figure 4.11 compared with the baseline flow. Although there is only a slight separation delay, the boundary layer remains attached over the highly convex region of the hump. This deflects the shear layer downward towards the wall, and the result is a smaller recirculation bubble. The local effect on the streamlines surrounding steady suction actuation is similar for the low and higher Mach number flow.

The oscillatory controlled case at higher Mach number is shown in figure 4.10(b). Both the low and higher Mach number flows have a lower C_p at separation than the baseline flow, but initiate pressure recovery earlier than the baseline flow. The alternating blowing and suction at $F^+ = 0.84$ creates regular shedding of vortices from the separated shear layer, which increases the entrainment of the fluid and accelerates the flow's reattachment to the wall. The oscillatory flow does not immediately deflect the shear layer downwards as much as the steady suction, although it does briefly reattach the flow after actuation.

The vorticity thickness of the controlled cases initially after separation is given in figure 4.12, and compared with the linear fit obtained from the baseline data. Over the initially separated region, the growth rate of the controlled cases is higher than the baseline flow, indicating higher initial

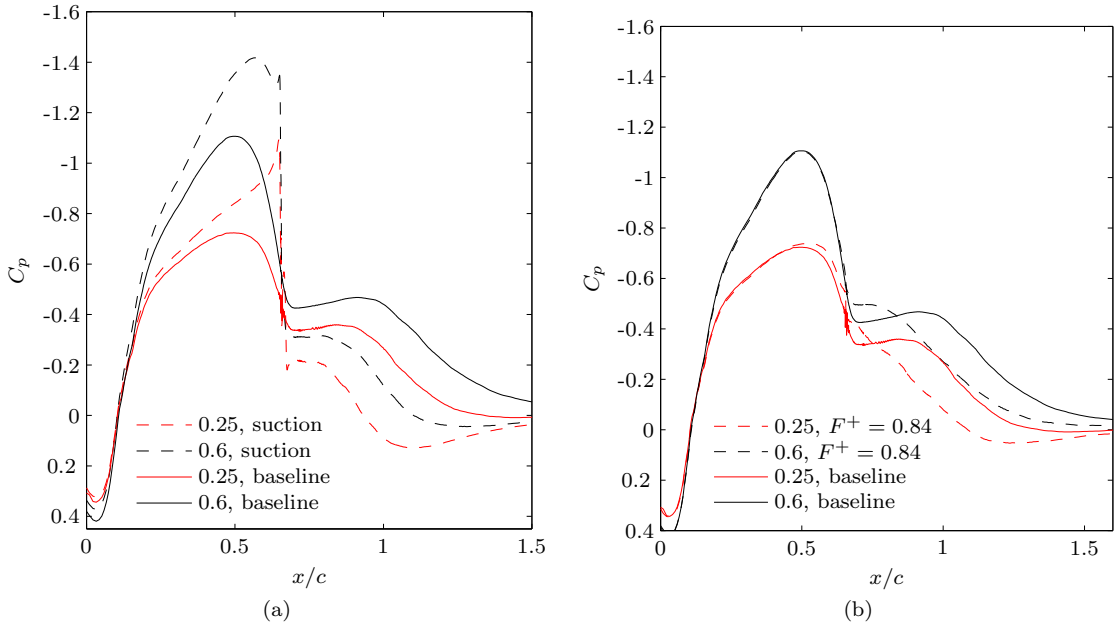

Figure 4.10: C_p of the $M = 0.6$ controlled flow compared with previous results at $M = 0.25$.

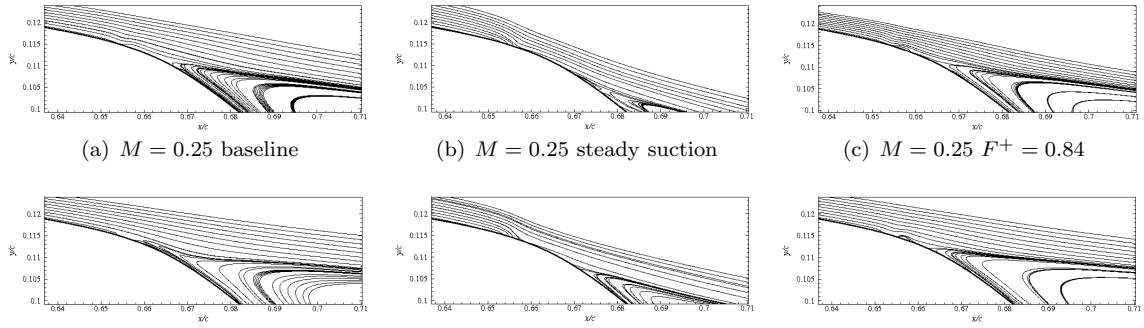

(a) $M = 0.25$ baseline (b) $M = 0.25$ steady suction (c) $M = 0.25$ $F^+ = 0.84$

(d) $M = 0.6$ baseline (e) $M = 0.6$ steady suction (f) $M = 0.6$ $F^+ = 0.84$

Figure 4.11: Average streamlines surrounding actuation.

entrainment, which may aid in deflecting the shear layer towards the wall.

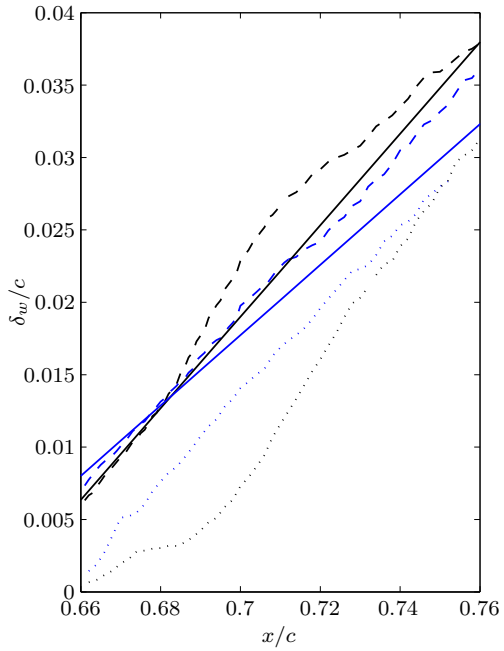

Figure 4.12: Vorticity thickness of steady suction control (dotted line) and oscillatory control (dashed line) for $M = 0.25$ (black) and $M = 0.6$ (blue), compared with linear fit of baseline data from figure 4.4(a).

4.2.2 Control Effectiveness

The effectiveness of control can be measured by the overall size of the separation bubble or location of reattachment, and by the decrease in form drag along the trailing edge of the hump. In an actual airfoil, control modifies the entire circulation around the body, and the lift coefficient, or lift to drag ratio is an important parameter of control effectiveness. For the wall-mounted hump flow lift or vertical force is not a good performance indicator because it is primarily generated at mid-chord, and is thus not directly affected by the separation and control along the trailing edge.

In terms of shortening the separation bubble, the effect of the control is similar for the low and higher Mach number flows. For the same value of $C_m = 0.15\%$, control at the higher Mach number decreases the baseline bubble length by 18.6%, whereas it decreases by 20.3% for $M = 0.25$. The oscillatory controlled case shortens the average separation bubble length by 15.5% compared to the baseline flow at $M = 0.6$, and 13.5% at $M = 0.25$.

With oscillatory control, the flow separates at a lower average C_p than the baseline case, causing an increase in drag due to the fuller C_p profile over the backwards-facing trailing edge where the drag force is most prominent. So although the oscillatory control initiates an earlier reattachment from the baseline state, the average pressure drag is increased. Table 4.2 compares the drag and reattachment locations of the LES and experimental data, and table 4.3 summarizes the performance for the low and higher Mach number controlled flows. The baseline form drag compares well with experimental results from Seifert and Pack [17], which is also calculated from integration of the C_p data. The steady suction control is most effective at decreasing drag because the enhanced pressure recovery at $x/c \approx 0.66$ raises the pressure along the trailing edge before separation. At the same C_m, the steady suction control is only slightly more effective at decreasing drag in the lower Mach number flow.

Table 4.2: Baseline pressure drag $C_{d,p}$ and reattachment location $(x/c)_{re}$ compared with experimental data [17].

Mach	case	$C_{d,p}$	$(x/c)_{re}$
0.25	exp.	0.027	1.10
0.25	LES	0.028	1.18
0.6	exp.	0.035	n/a
0.6	LES	0.035	1.29

Table 4.3: The effect of control on the form drag $C_{p,d}$ and reattachment location $(x/c)_{re}$.

Mach	case	$C_{d,p}$	$(x/c)_{re}$
0.25	baseline	0.028	1.18
0.25	$C_\mu = -0.11\%$	0.014	0.94
0.25	$\langle C_\mu \rangle = 0.11\%$	0.030	1.02
0.6	baseline	0.035	1.29
0.6	$C_\mu = -0.11\%$	0.018	1.05
0.6	$\langle C_\mu \rangle = 0.11\%$	0.041	1.09

The pressure drag is plotted versus time in figures 4.13 and 4.14 for the low and higher Mach numbers respectively. The corresponding maximum slot velocity is given above the pressure drag for reference. In figure 4.13 the drag immediately decreases close to zero when the steady suction is turned on, before increasing and leveling off. Contour images of the flow field show that a large vortex is formed over the trailing edge when the control is turned on. This structure convects downstream

for approximately $2tU_\infty/c$, the same time it takes for the drag to achieve steady state. Immediately after the initial vortex is shed, the separation bubble is almost eliminated, then it gradually grows back until it maintains its steady state at approximately $tU_\infty/c = 6$. The higher Mach number flow also decreases when steady suction control is turned on, but it does not temporarily reattach the flow. An initial, but weaker, vortex is shed and does not cause the separation bubble to disappear. The separation bubble does decrease in size however, and maintain its reduced length. The local increase in drag at $tU_\infty/c = 6$ is due to a pressure wave traveling upstream and affecting the drag component at the leading edge and is not due to the trailing edge separation bubble.

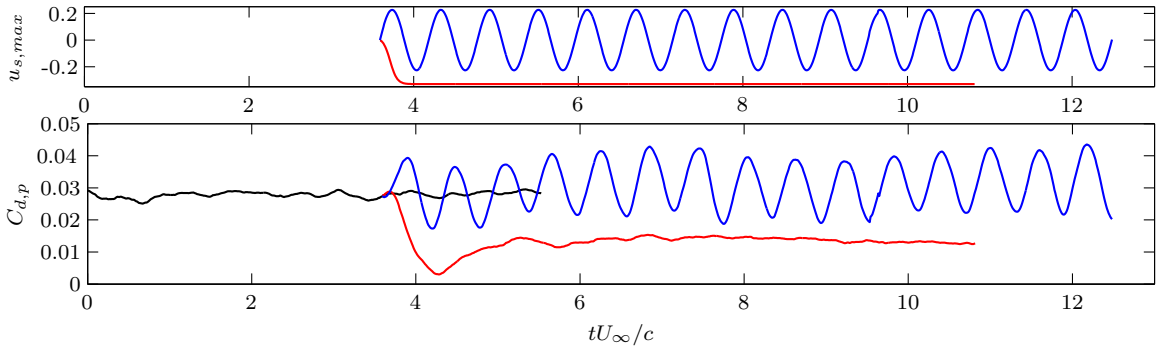

Figure 4.13: Time vs. form drag and time vs. $u_{s,max}$ for baseline (black), suction (red) and oscillatory (blue) flows at $M = 0.25$.

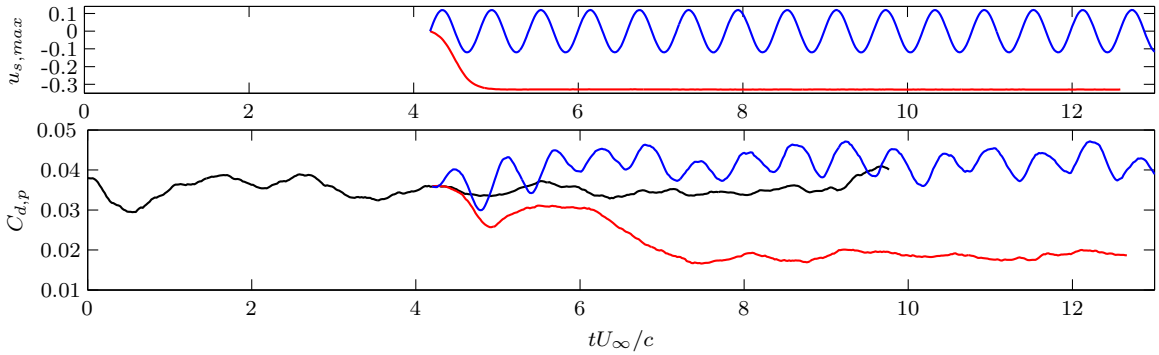

Figure 4.14: Time vs. form drag and time vs. $u_{s,max}$ for baseline and controlled flows at $M = 0.6$ Legend the same as in figure 4.13.

Phase-averaged vorticity fields of the low and higher Mach number flows are shown in figure 4.15 and the corresponding C_p values are given in figure 4.16. The two phases shown correspond to $u_{s,max} = 0$. The phase $\phi = 0°$ occurs after the suction cycle and $\phi = 180°$ occurs after the completion of the blowing cycle. When the suction phase of the actuation is turned on, the shear

layer is pulled towards the surface while the vortex from the previous cycle convects downstream. When the blowing phase begins, the vorticity collected close to the surface during the suction phase rolls up and grows in size, pinching off as the next suction phase begins.

In the higher Mach number flow the suction phase is not as effective in deflecting the shear layer towards the wall, resulting in a lower phase-averaged C_p in figure 4.16(a). As a result, the vortices are less coherent as they are shed, resulting in a lower and wider suction peak in figure 4.16(b). The higher Mach number vortices also have a higher phase velocity, which can be seen by the increased distance between suction peaks in the phase-averaged flow. An approximate value of the vortex's convective velocity can be given by an average of the velocities above and below the shear layer, or $u_c(x)/U_\infty = (u_{max}(x) - u_{min}(x))/2U_\infty$. Therefore, since $u_{max}(x)/U_\infty$ is greater in the $M = 0.6$ flow, the vortex convective velocity is also expected to be greater

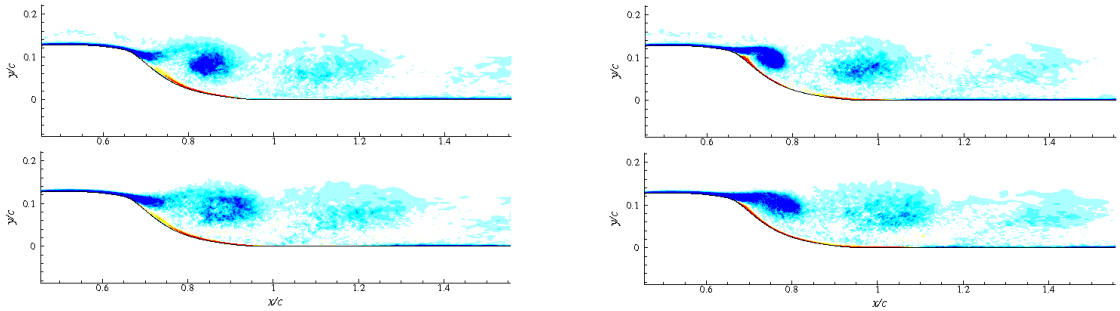

(a) $\phi = 0°$ (b) $\phi = 180°$

Figure 4.15: Phase-averaged vorticity. Low Mach number flow (top), higher Mach number flow (bottom).

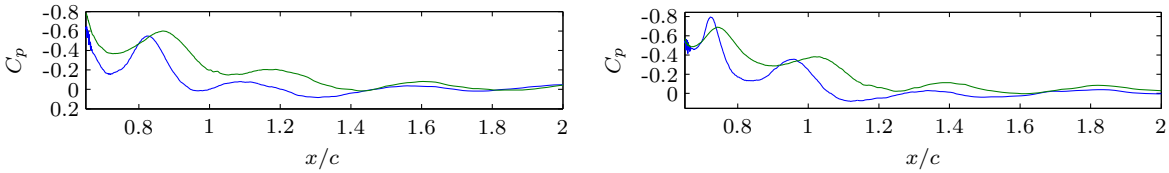

(a) $\phi = 0°$ (b) $\phi = 180°$

Figure 4.16: Phase-averaged C_p for low (blue) and higher (green) Mach number flows with oscillatory control.

Chapter 5

Effects of Actuation Frequency

The effective range of forcing frequencies has been explored in many experimental [11] and computational [13, 14, 15] investigations of separated flows. Forcing frequencies are generally divided into two regimes, one on the order of the natural large-scale shedding frequency $F^+ \sim O(1)$, and one an order of magnitude higher at $F^+ \sim O(10)$. The higher frequency range is decoupled from the natural shedding instability and is associated with the Kelvin-Helmholtz instabilities of the separated shear layer. This chapter explores both ranges of forcing frequencies, and compares the results with previous investigations. First, a 2D low Reynolds number direct numerical simulation (DNS) of the hump geometry is performed in order to give insight into the complicated turbulent dynamics by using a simplified system. Next, high frequency forcing is applied to the 3D LES and flow metrics are compared with the low frequency forcing and baseline flow.

5.1 2D Direct Numerical Simulations

5.1.1 2D DNS of Baseline Flow

Two dimensional direct numerical simulations (DNS) of the wall-mounted hump flow are performed at $Re = 15,000$ for the low and high Reynolds number flow. The numerical method is the same as the LES described in chapter 2 except that spatial filtering and the turbulence SGS model are not applied.

The 2D simulations are substantially different from the 3D simulations at high Reynolds number.

Figure 5.1 displays the average streamwise velocity contours and streamlines for the baseline flow at $M = 0.25$ and $M = 0.6$. When compared with the 3D results in figures 4.2 and 4.3, the separation bubble has increased significantly, due to an earlier separation as well as a delayed reattachment. There is also a second recirculation region beneath the primary separation bubble along the leading edge. This feature is more pronounced in the 2D $M = 0.6$ flow but it is not present in the 3D simulation. As in the 3D simulations, the average separation bubble is larger in the $M = 0.6$ than in the $M = 0.25$ flow. However this discrepancy between the reattachment locations of the $M = 0.25$ and $M = 0.6$ cases is greater in the 2D simulations.

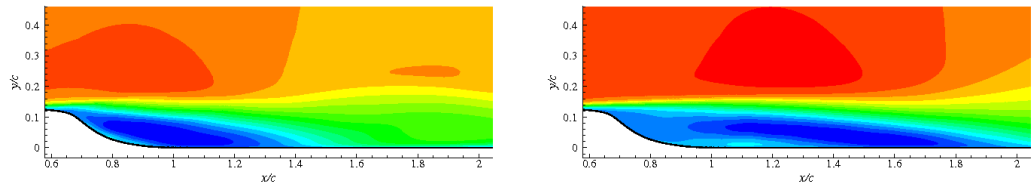

(a) u/U_∞: 16 contours from -0.2 to 1.3

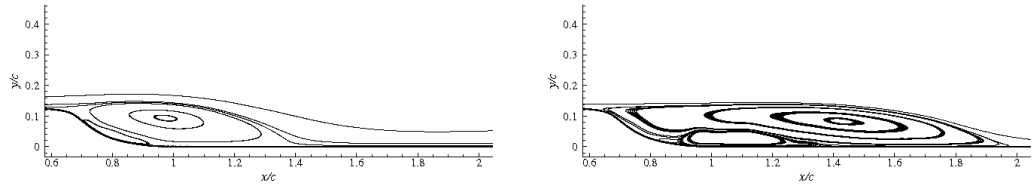

(b) Average streamlines

Figure 5.1: Averaged 2D baseline flow at $Re = 15,000$ and $M = 0.25$ (left) and $M = 0.6$ (right).

The 2D averaged pressure coefficients in figure 5.2 also show an earlier separation location and a longer separated region in comparison with the 3D averaged flow in figure 4.1(a). Compared with the 3D simulations, the average flow has a weaker suction peak at midchord and only a very brief pressure recovery before separation. Along the trailing edge the pressure is equal to or lower than the attached flow at midchord, causing significant pressure drag. There is a second suction peak before pressure recovery, similar to the 3D flow but more pronounced, and it occurs further downstream. The $M = 0.6$ flow has a region of constant pressure within the separation bubble before the reattachment process is initiated. In both the $M = 0.25$ and $M = 0.6$ flows, the average pressure recovery location of the 2D simulations occurs significantly downstream of that in the 3D simulations. The fully turbulent 3D flow is characterized by a range of scales, from small scales

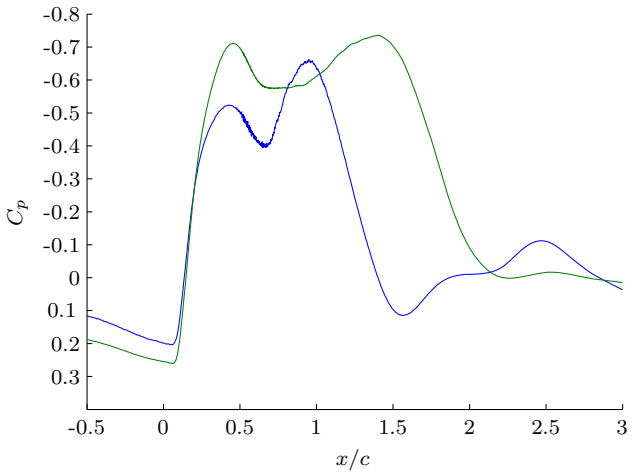

Figure 5.2: Pressure coefficients of $M = 0.25$ (blue) vs. $M = 0.6$ (green) 2D DNS.

that emanate from the boundary layer to large, highly unsteady structures that are shed from the separation bubble and dissipate very quickly. The 2D flow has a laminar boundary layer which separates upstream from the turbulent boundary layer, forming a separated shear layer which rolls up into coherent vortices. In the higher Mach number case, the shear layer extends over the trailing edge, and vortices roll up and interact with one another aperiodically as seen in the instantaneous vortcity contours in figure 5.3(b). At lower Mach numbers, the vortices are shed periodically and begin to roll up almost immediately after separation, as shown in figure 5.3(a).

Figure 5.4 contains the signal of a velocity probe placed within the shear layer at $x/c = 0.74$. The frequency of shedding in the $M = 0.25$ case corresponds to $fc/U_\infty \sim 0.8$. This frequency is equal to an $F^+ \sim 0.4$ when $X_{sep} = c/2$ as defined in the 3D simulation. However since the separation distance is larger in the 2D simulations, the modified value of X_{sep} is 0.9, resulting in a natural shedding frequency of $F^+ = 0.76$. The velocity signal at $M = 0.6$ is representative of many lower frequency components, which are from the aperiodic shedding of vortices and the merging and interactions with one another as the shear layer reattaches. Even with velocity probes placed further downstream in the $M = 0.6$ shear layer, periodic shedding does not occur. At a lower Reynolds number of 8,000, the $M = 0.25$ flow more closely resembles the $M = 0.6$ flow. The separated shear layer extends further downstream before vortex shedding and reattachment, and the shedding is less periodic. As the Reynolds number increases, reattachment is moved closer to the trailing edge, and

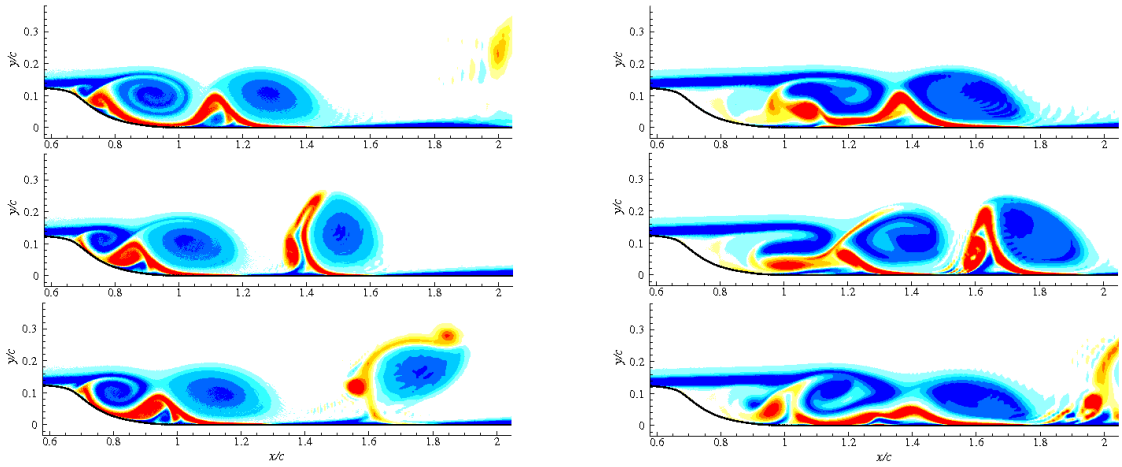

(a) $M = 0.25$ (b) $M = 0.6$

Figure 5.3: Instantaneous vorticity contours depicting the roll-up and shedding of 2D vortices in the baseline flow.

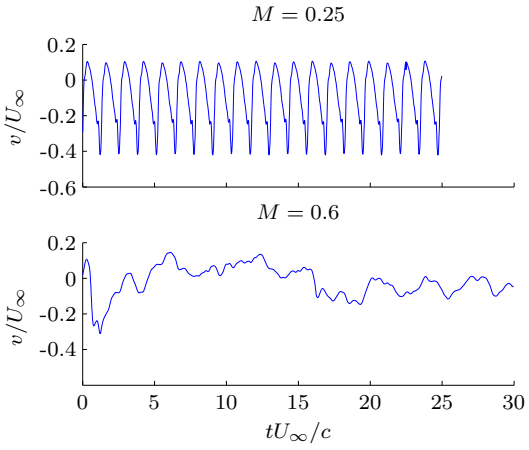

Figure 5.4: Shear layer v velocity probe at $x/c = 0.74$ ($s3$ in figure 4.8) in the 2D baseline flow.

at a critical Reynolds number periodic shedding occurs over the trailing edge. It is hypothesized that the 2D $M = 0.6$ flow will also have periodic shedding at a higher Reynolds number.

It should be noted that periodic shedding of vortices is not observed in the 3D LES or in the fully turbulent experiments of the baseline flow. There are low frequency peaks in the 3D spectra at various locations within the separation bubble, but the flow does not lock onto one distinct frequency. In the 3D turbulent flow, the most dominant frequency within the shear layer changes depending on the location (see figure 4.9). In the 2D flow at $Re = 15,000$, the shedding frequency $fc/U_\infty \sim 0.8$ is dominant at all probe locations. The locked-in shedding frequency, the earlier separation, and longer reattachment region are the most notable differences between the 2D and 3D baseline flow.

5.1.2 2D DNS of Controlled Flow

Since the 2D baseline flow separates upstream of the 3D simulations, the actuation location is also moved upstream to $x/c = 0.6$. The slot velocity and C_μ values remain the same as in the validation test cases in chapter 3. The flow is forced at non-dimensional frequencies of $fc/U_\infty = 0.84$, 1.68, and 3.36, corresponding to $F^+ = 0.76$, 1.5, and 3.0 when $X_{sep}/c = 0.9$, calculated from 2D $M = 0.25$ baseline flow. Note that is differs from the separation distance used in the 3D flow, which is based on the 3D $M = 0.25$ baseline separation distance, or $X_{sep}/c = 0.5$.

This lowest forcing frequency, $F^+ = 0.76$, is approximately equal to that of the natural shedding frequency found in the 2D $M = 0.25$ flow. The forcing frequency $F^+ = 1.5$ corresponds to $fc/U_\infty = 1.68$, and is equal to the frequency used in the LRCW oscillatory test case and in the high Reynolds number validation presented in chapter 3.

The average pressure coefficients of the forced flow are shown in figure 5.5. At the lowest forcing frequency, the separation bubble is reduced for the $M = 0.6$ flow, but remains approximately the same length for $M = 0.25$. At $F^+ = 1.5$, both flows show a reduction in separation length, and at $F^+ = 3.0$ forcing is not effective in reducing separation or promoting an earlier pressure recovery.

Figure 5.6 displays a velocity signal over time, located in the shear layer at $x/c = 0.74$. For all the forcing frequencies, the low Mach number flow maintains its natural shedding frequency as the

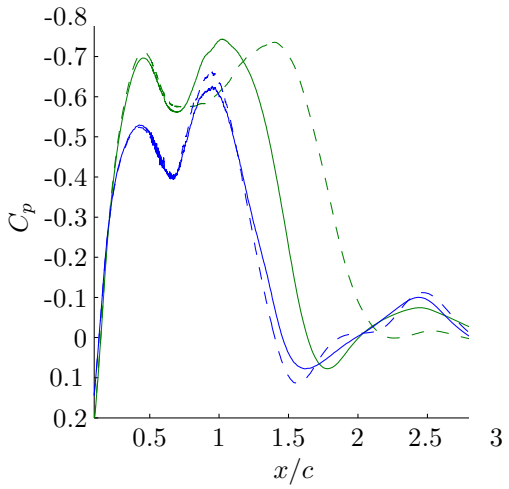

(a) $F^+ = 0.76$

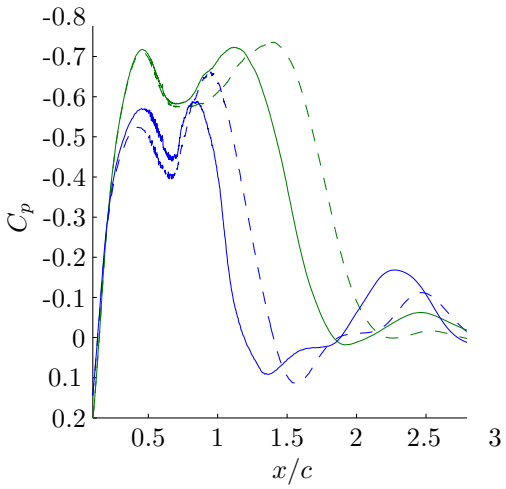

(b) $F^+ = 1.5$

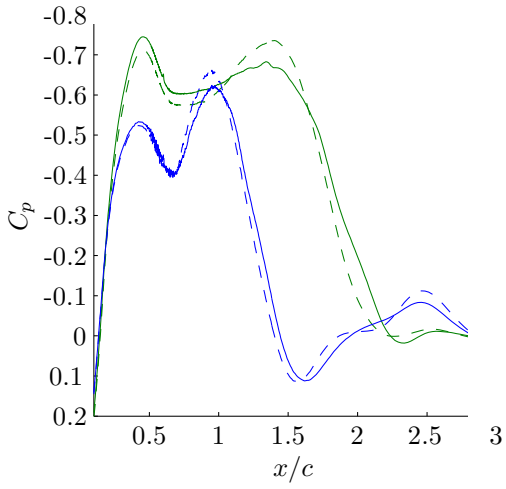

(c) $F^+ = 3.0$

Figure 5.5: Average pressure coefficients of controlled (solid) and baseline flow (dashed) for $M = 0.25$ (blue), $M = 0.6$ (green).

most dominant frequency. When forced at $F^+ = 1.5$, approximately twice the shedding frequency, the $M = 0.25$ flow locks into the natural shedding frequency through an immediate vortex pairing after actuation. A frequency lock-in behavior is also found in the 2D RANS high angle-of-attack airfoil simulations by Wu et al. [13]. When forced at an excitation frequency twice that of the natural shedding frequency, the lift and drag signals become locked-in to a single frequency and produce a highly organized vortex shedding. When the flow responds by locking into a frequency, the best separation length reduction is achieved. Likewise, in the investigations by Wu et al., the best lift-to-drag ratio is found at excitation frequencies that exhibited a locked-in frequency response.

Forcing at $F^+ = 0.76$, approximately equal to the natural shedding frequency, also decreases the separation bubble length but is not as effective as actuating the flow at $F^+ = 1.5$. At actuation frequencies higher than twice the natural shedding frequency, the flow does not lock into a single frequency, and the average flow is not modified significantly.

At $M = 0.6$, the flow is most responsive to the lowest forcing frequency, which resulted in a more periodic shedding. The velocity spectra show increased activity at frequencies around $fc/U_\infty = 0.65$. In all the $M = 0.6$ forced cases, the forcing frequency is detectable downstream at $x/c = 0.74$, whereas it is not easily detected at $M = 0.25$. The higher Mach number does not lock into any single shedding frequency with any of the forcing frequencies that are tested.

The response of the 2D flow to various actuation frequencies indicates that forcing the flow at frequencies one to two times the natural shedding frequency is most beneficial to decreasing the size of the separation bubble. As the actuation frequency is increased higher than twice the natural shedding frequency, the separation bubble increases slightly larger than the baseline flow. The $M = 0.6$ velocity probe indicates a strong presence of the high frequency actuation in the shear layer, but the lower modes seen in the baseline flow are attenuated. Higher frequency forcing of the $M = 0.25$ flow results in less periodic shedding than the baseline flow, which is detrimental to the reattachment process.

The purpose of performing the 2D DNS of the wall-mounted hump is to demonstrate that there are significant differences between the turbulent, three-dimensional flow and the low Reynolds num-

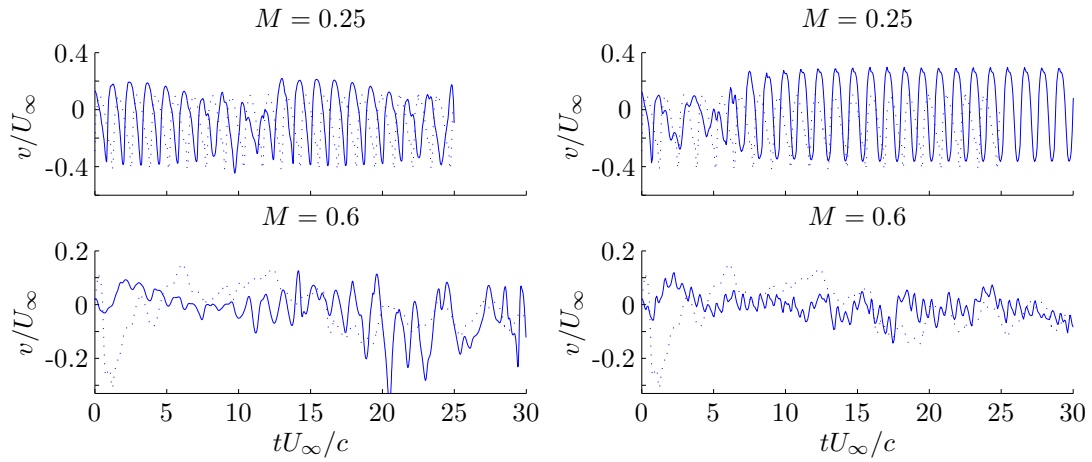

(a) $fc/U_\infty = 0.84$

(b) $fc/U_\infty = 1.68$

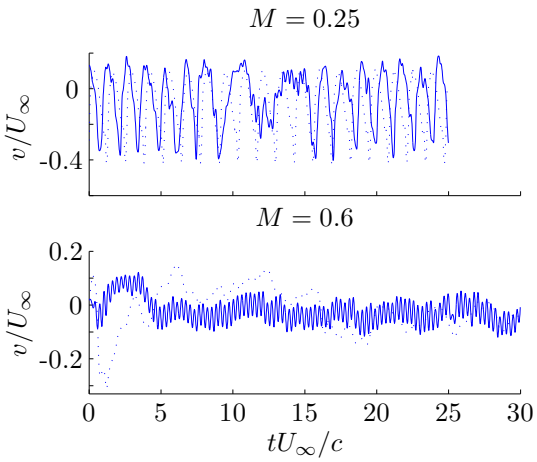

(c) $fc/U_\infty = 3.36$

Figure 5.6: Shear layer v velocity probe at $x/c = 0.74$ ($s3$ in figure 4.8) in 2D baseline (dashed) and controlled flow (solid).

ber 2D simulations. In two-dimensions, the shedding frequency becomes locked-in above a threshold Reynolds number, and the separation bubble is elongated due to an earlier separation and delayed reattachment. However, there are also many similarities, and the 2D DNS provides a simplified model of the complex three-dimensional turbulent separation bubble. The 2D separation bubble has fewer active frequencies or modes, and thus the vortex dynamics are simplified. Using this as a model for the fully turbulent flow, the actuation frequency is investigated and found to be effective at one to two times the natural shedding frequency. The next section will expand on this idea, and examine the effect of actuation frequency in the full 3D LES.

5.2 3D LES: High Frequency Forcing

A range of actuation frequencies are investigated for the $M = 0.6$ with a constant momentum coefficient of $C_\mu = 0.11\%$. The frequencies are multiples of the test case frequency in chapter 3: $F^+ = 0.84$, 1.7, 2.5, 3.4, 5.0, and 8.4. One additional actuation frequency of $F^+ = 11.8$ is performed for the $M = 0.25$ case.

5.2.1 Effect of Actuation on the Mean Flow

The average pressure coefficient for the various actuation frequencies is shown in figure 5.7. The low frequency (LF) actuation at $F^+ = 0.84$ and 1.7 both initiate an earlier pressure recovery and reattachment, whereas the high frequency (HF) actuation at $F^+ = 5.0$, 8.4, and 11.8 slightly delay the pressure recovery and reattachment. The two frequencies in between the LF and HF, $F^+ = 2.5$ and 3.4, do not have a significant effect on the average C_p.

Other investigations have also reported an increase in separation bubble length with HF actuation [15, 14]. Using LES, Dandois et al. applied LF and HF actuation to the naturally separating flow on a curved backward-facing step at $Re_h \approx 28,000$. Using a relatively high momentum coefficient compared to experimental investigations ($\langle C_\mu \rangle = 1\%$), they found a reduction in separation bubble length of 54% with LF actuation, and an increase in 43% when HF actuation was applied. A milder enhancement in separation is also found when HF actuation is applied to the 2D simulations around

an airfoil at high angle-of-attack [14].

The average pressure coefficients in figure 5.7 are all from cases performed with a momentum coefficient of $\langle C_\mu \rangle = 0.11\%$. Figure 5.8 displays the pressure coefficient of two HF cases at a higher momentum coefficient of $\langle C_\mu \rangle = 0.23\%$. The controlled case in figure 5.8(b) is actuated at $x/c = 0.655$, the same location as previously presented cases, and figure 5.8(a) is actuated further upstream of the natural separation point at $x/c = 0.60$. As seen figure 5.7, modifying the actuation location and the momentum coefficient of the high frequency actuation did not have a significant effect on the mean separation and reattachment behavior. There is a small increase in pressure at the actuation location, which is more distinguishable when the flow is actuated at the $x/c = 0.60$ location, but it does not have any noticeable global effects on the flow.

A similar trend is seen in the average velocity contours in figure 5.9 where the LF and HF cases are compared with the baseline flow. The $u/U\infty$ contours display a shorter recirculation region with LF actuation, but HF appears very similar to the baseline flow. The LF shows an increase in the reverse flow beneath the shear layer, and also an increase in negative vertical velocity above the shear layer. The increase in velocity magnitude indicates a higher rate of fluid entrainment into the shear layer from both the high speed fluid above, and the low speed fluid below the shear layer. Compared with the baseline flow, the HF actuation causes lower magnitudes of vertical velocity above the shear layer. This could be the result of lower levels of entrainment from the freestream fluid, or a net deflection of the shear layer away from the wall.

5.2.2 Local Effects of Actuation

The mean flow can also be examined locally at the actuation location. Previous investigations have hypothesized that HF actuation can modify the mean streamwise velocity profile, increasing stability of the boundary layer and inhibiting growth of large scale structures [16]. If the HF actuation were successful in inhibiting large-scale structure growth, it would be beneficial in reducing acoustic resonance generated by these structures. Other investigators have found that HF actuation can delay separation by stabilizing the local boundary layer and modifying the streamwise pressure

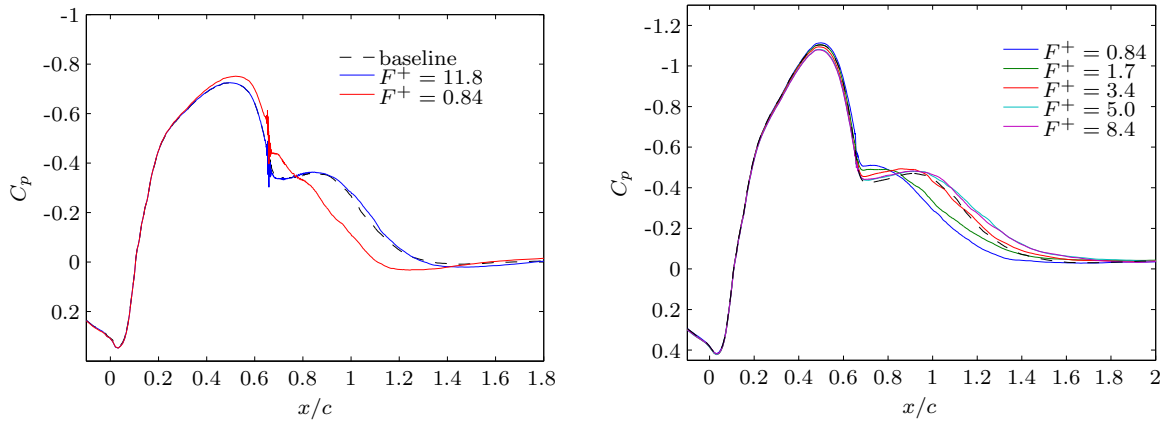

(a) $M = 0.25$ (b) $M = 0.6$

Figure 5.7: The effect of actuation frequency on the average pressure coefficient. For all actuation frequencies: $\langle C_\mu \rangle = 0.11\%$

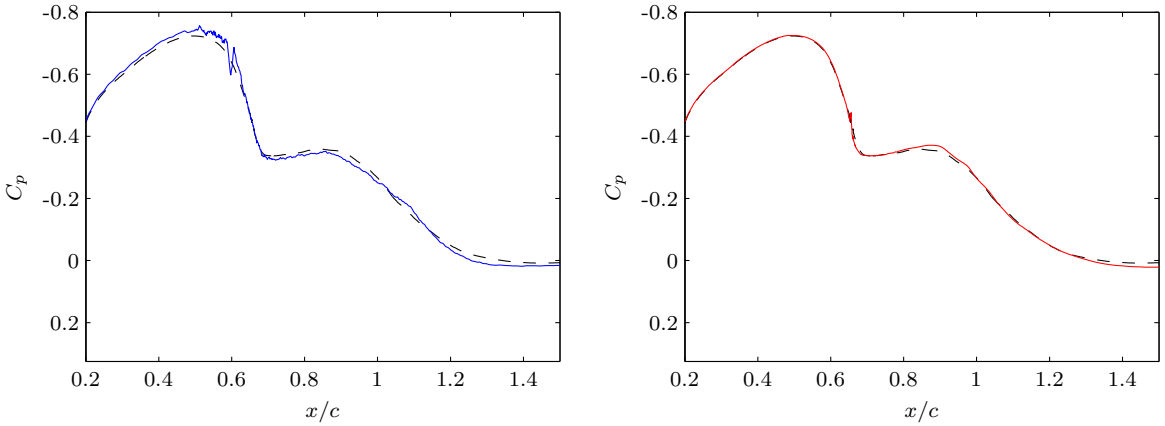

(a) Actuation location (b) Actuation strength

Figure 5.8: The effect of location and C_μ of high frequency actuation on the average pressure coefficient. Left figure: baseline (dashed) and $F^+ = 11.8$, $\langle C_\mu \rangle = 0.23\%$ actuated at $x/c = 0.60$ (blue). Right figure: baseline (dashed) and $F^+ = 11.8$, $\langle C_\mu \rangle = 0.23\%$ actuated at $x/c = 0.655$ (red).

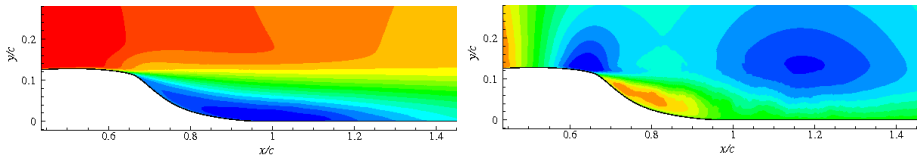

(a) $M = 0.6$ baseline

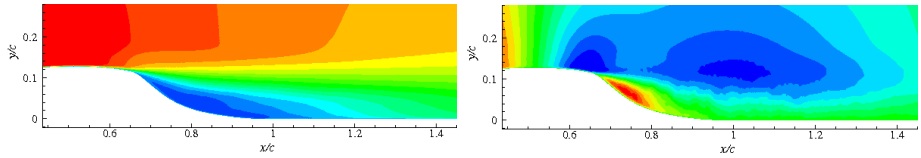

(b) $M = 0.6$ $F^+ = 0.84$

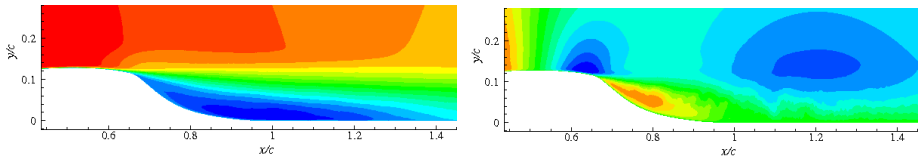

(c) $M = 0.6$ $F^+ = 8.4$

Figure 5.9: Average velocities $\bar{u}/U_\infty$ (left) and $\bar{v}/U_\infty$ (right). $\bar{u}/U_\infty$ contour levels from -0.2 to 1.3, $\bar{v}/U_\infty$ contour levels from -0.1 to 0.1.

gradient [12].

To look at the local effect of actuation, the momentum and vorticity thickness are calculated. The momentum thickness is modified to adjust for the acceleration of the freestream flow, as given in Eq. (5.1), and the vorticity thickness is defined by Eq. (4.1). The local momentum thickness is plotted for the baseline and controlled cases in figure 5.10. The LF actuation significantly increases the momentum thickness by 24% at $M = 0.25$, and more moderately increases it by 12% for the $M = 0.6$ flow. The modification in momentum thickness is both upstream and downstream of the actuation location. From low to high frequency, the momentum thickness decreases in size, and is less than the baseline case for the highest actuation frequencies. The two highest actuation frequencies have the same momentum thickness, which may imply that there is a threshold frequency above which the boundary layer will have the same response. The HF actuation reduces the momentum thickness by approximately 10% at $M = 0.6$ and 6% at $M = 0.25$.

$$\theta(x) = \int_{y_{min}}^{\infty} \frac{\bar{u}(x,y) - u_{min}(x)}{u_{max}(x) - u_{min}(x)} \left(1 - \frac{\bar{u}(x,y) - u_{min}(x)}{u_{max}(x) - u_{min}(x)}\right) \tag{5.1}$$

The spatial growth of the vorticity thickness is calculated with a linear fit beginning just after separation at $x/c = 0.67$. As seen in chapter 4, the growth rate of the shear layer is not linear, but the initially separated region is approximated by a linear fit to obtain a measure of the shear layer's growth rate. Estimates of the initial $d\delta_\omega/d(x/c)$ are given in table 5.1 for the controlled $M = 0.25$ and $M = 0.6$ flows. The $M = 0.25$ results indicate a decrease in $d\delta_\omega/d(x/c)$ for HF actuation and an increase for LF actuation compared with the baseline flow. At $M = 0.6$, $d\delta_\omega/d(x/c)$ decreases with increasing frequency, and is slightly less than the baseline growth rate at the highest frequency. Thus, LF actuation is actively increasing the growth of the shear layer whereas HF actuation slightly diminishes the growth rate immediately after separation.

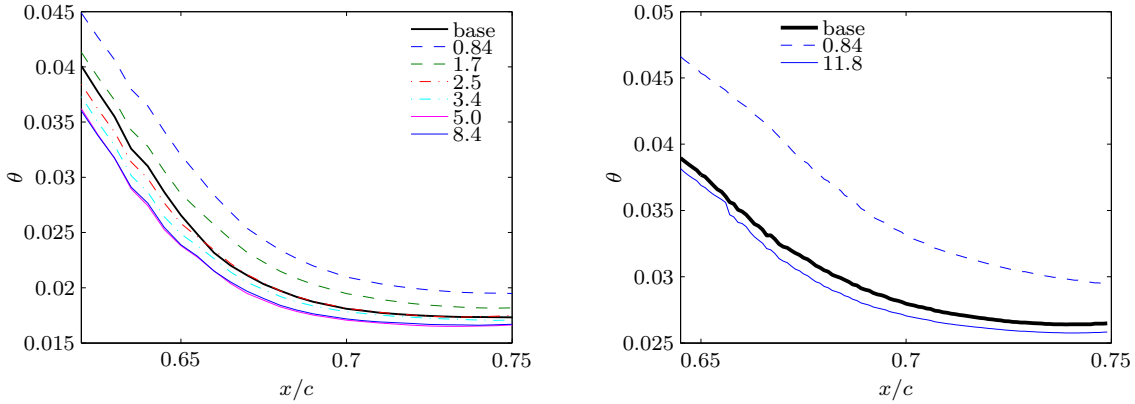

(a) $M = 0.6$ (b) $M = 0.25$

Figure 5.10: Boundary layer momentum thickness with various forcing frequencies. Control is applied at $x/c = 0.655$.

Table 5.1: Initial growth rate of controlled flow from a linear fit of $d\delta_\omega/d(x/c)$ between $0.67 < x/c < 0.76$ ($M = 0.6$) and $0.67 < x/c < 0.70$ ($M = 0.25$).

Mach	case	$d\delta_\omega/d(x/c)$
0.6	baseline	0.231
0.6	$F^+ = 0.84$	0.285
0.6	$F^+ = 1.7$	0.244
0.6	$F^+ = 2.5$	0.245
0.6	$F^+ = 3.5$	0.231
0.6	$F^+ = 5.0$	0.231
0.6	$F^+ = 8.4$	0.223
0.25	baseline	0.313
0.25	$F^+ = 0.84$	0.465
0.25	$F^+ = 11.8$	0.283

The averaged streamlines surrounding high frequency actuation are shown in figure 5.11. Compared to the baseline flow, the local streamlines are modified by the actuation. Averaged LF actuation streamlines have been previously shown in figure 4.11. At low frequencies, actuation creates a small recirculation bubble, briefly reattaching the flow downstream of where actuation is applied. High frequency actuation also modifies the local streamlines, but does not reattach the flow or delay the onset of separation. When HF actuation is applied, the streamlines are deflected towards the wall at the actuation location, an effect seen more clearly when the HF actuation is applied with a larger momentum coefficient, as seen in figures 5.11(e) and 5.11(f). This deflection corresponds to a very slight modification in the local streamwise pressure coefficient in figure 5.8(b), but does not significantly effect the pressure downstream or upstream of the actuation. Despite the streamline deflection closer to the wall, the average streamlines in figure 5.11 indicate that the flow separates at the same location as in the baseline flow. After separation, the HF actuation produces a slightly wider reverse flow region, which may slightly deflect the mean shear layer further away from the wall. When the flow is actuated further upstream of separation at $x/c = 0.6$, the local pressure coefficient is modified, as seen in figure 5.8(a). Once again the modification is local, and does not effect the mean flow within the separated region. Even though the local streamwise pressure is modified, the mean streamlines surrounding upstream actuation 5.11(g) are not strongly affected by the actuation.

The Reynolds stress profiles at $x/c = 0.67$ are plotted in figure 5.12. With HF actuation, the Reynolds stresses are lower than the baseline flow, whereas they are increased with LF actuation. Figure 5.13 plots the Reynolds stress contours of the separated region with HF actuation. Close to separation the Reynolds stresses are lower than in the baseline flow, but $u'u'/U_\infty^2$ displays a peak at reattachment slightly greater than that at the same location in the baseline flow.

The lower level of velocity fluctuations may be responsible for the initially lower growth rate, and greater deflection from the wall. Amitay and Glezer [11] have also found lower turbulent Reynolds stresses with HF actuation in their experimental airfoil experiments. However in these experiments, the boundary layer separation is delayed within the region of decreased Reynolds stresses, a feature

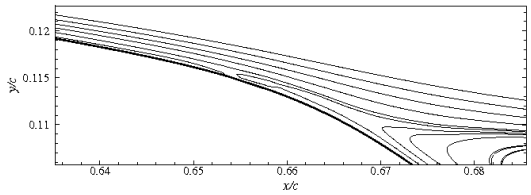

(a) $M = 0.6$: baseline

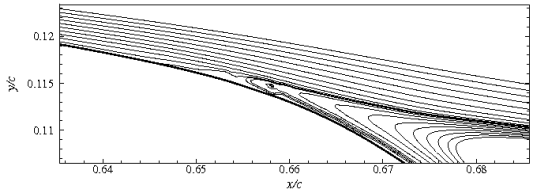

(b) $M = 0.25$: baseline

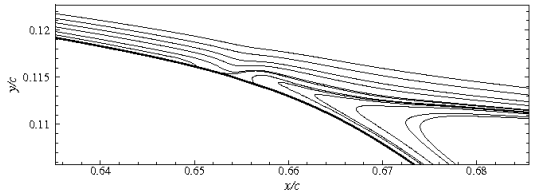

(c) $M = 0.6$: $F^+ = 8.4$, $\langle C_\mu \rangle = 0.11\%$

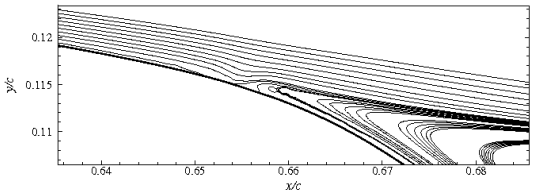

(d) $M = 0.25$: $F^+ = 11.8$, $\langle C_\mu \rangle = 0.11\%$

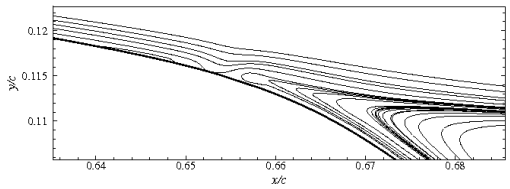

(e) $M = 0.6$: $F^+ = 8.4$, $\langle C_\mu \rangle = 0.16\%$

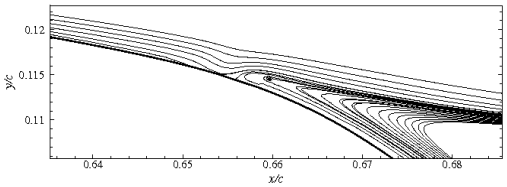

(f) $M = 0.25$: $F^+ = 11.8$, $\langle C_\mu \rangle = 0.23\%$

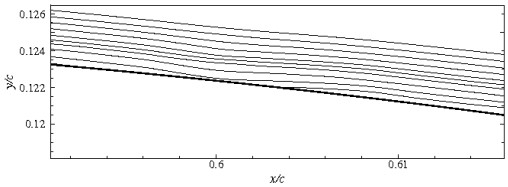

(g) $M = 0.25$: $F^+ = 11.8$, $\langle C_\mu \rangle = 0.23\%$

Figure 5.11: Averaged streamlines surrounding separation and actuation. Actuation is centered at $x/c = 0.655$ for (c) - (f) and at $x/c = 0.60$ for (g).

that is not observed in the present configuration.

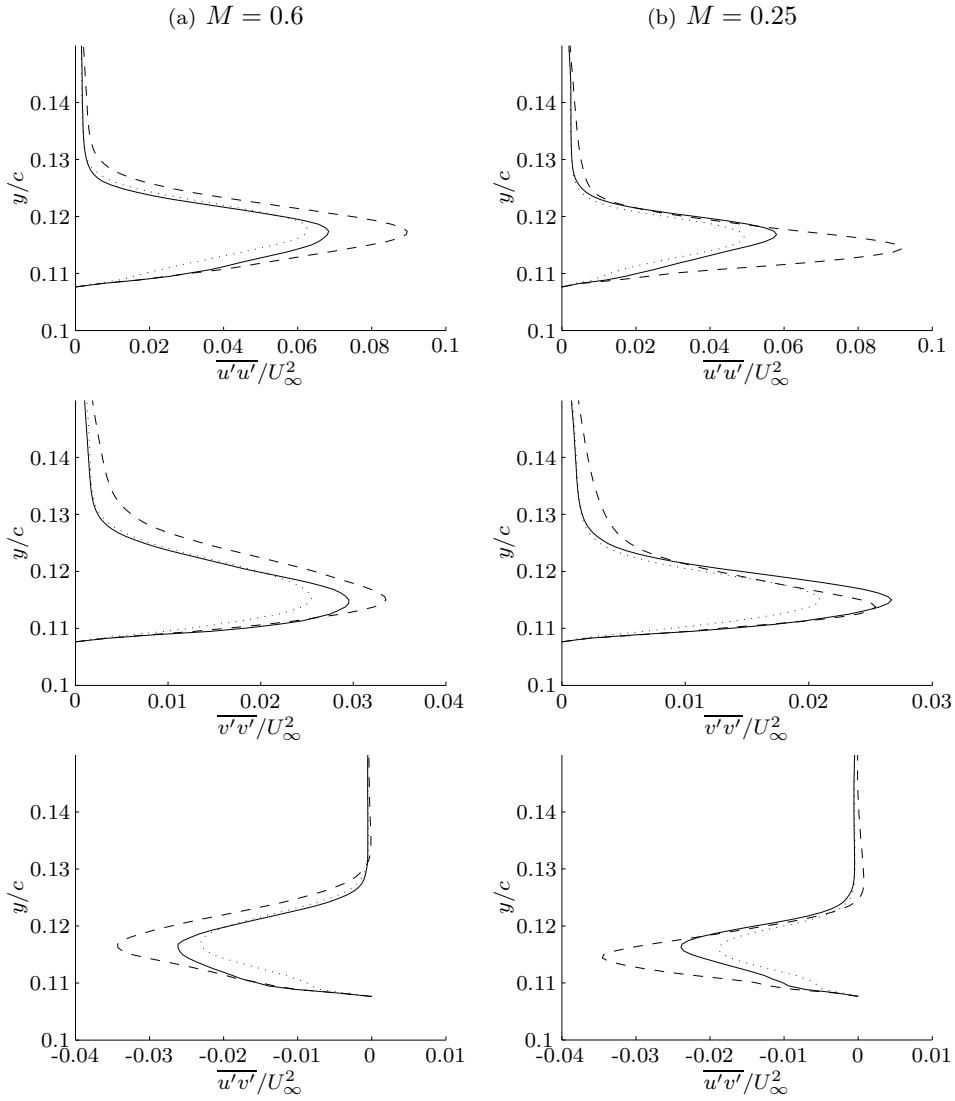

Figure 5.12: Resolved turbulent Reynolds stresses at $x/c = 0.67$ for: baseline flow (solid line), LF actuation (dashed), and HF actuation (dotted).

5.2.3 Unsteady Effects of Actuation

The phase-averaged spanwise vorticity of three actuation frequencies, $F^+ = 0.84$, 1.7, and 5.0, are shown in figure 5.14. With LF actuation, coherent structures form at separation and are shed from the shear layer as depicted in the LF suction and actuation phases in figures 5.14(a)-5.14(d). As the frequency increases, structures that result from actuation are no longer distinguishable in the phase-averaged vorticity. At $M = 0.6$ and $F^+ \geq 5.0$ there is no difference between the suction and

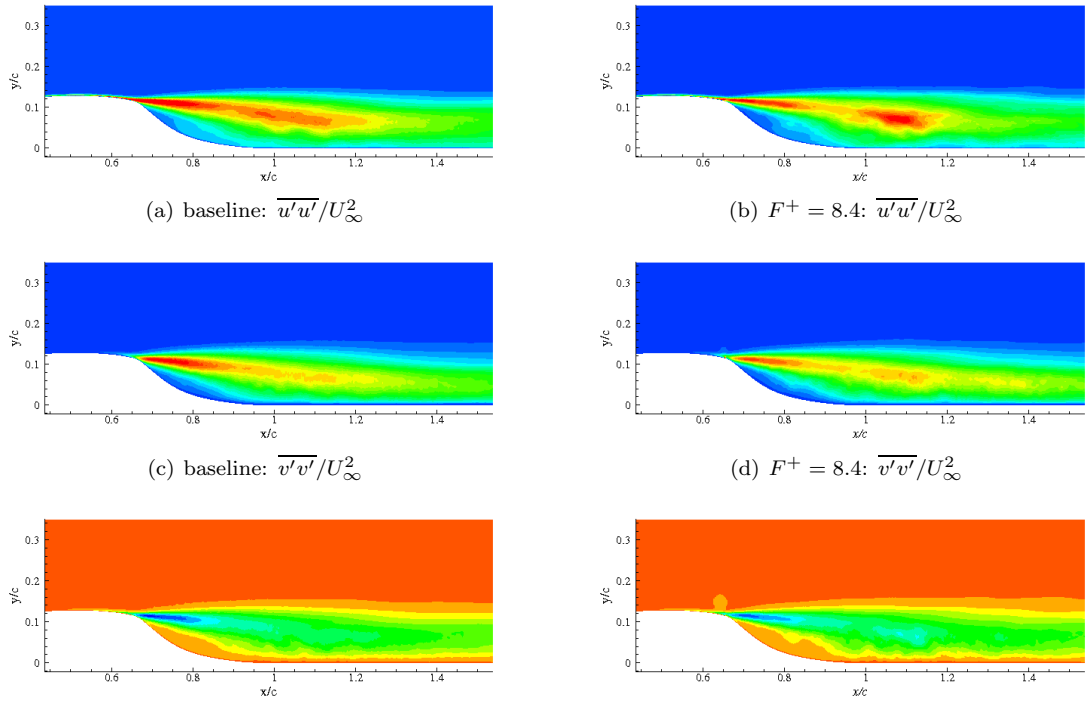

(a) baseline: $\overline{u'u'}/U_\infty^2$

(b) $F^+ = 8.4$: $\overline{u'u'}/U_\infty^2$

(c) baseline: $\overline{v'v'}/U_\infty^2$

(d) $F^+ = 8.4$: $\overline{v'v'}/U_\infty^2$

(e) baseline: $\overline{u'v'}/U_\infty^2$

(f) $F^+ = 8.4$: $\overline{u'v'}/U_\infty^2$

Figure 5.13: $M = 0.6$ resolved turbulent Reynolds stresses. Contour levels: $\overline{u'u'}/U_\infty^2$: $[0 : 0.002 : 0.044]$, $\overline{v'v'}/U_\infty^2$: $[0 : 0.002 : 0.036]$, $\overline{v'u'}/U_\infty^2$: $[-0.028 : 0.002 : 0.002]$.

blowing phase-averaged vorticity contours in figures 5.14(e) and 5.14(f).

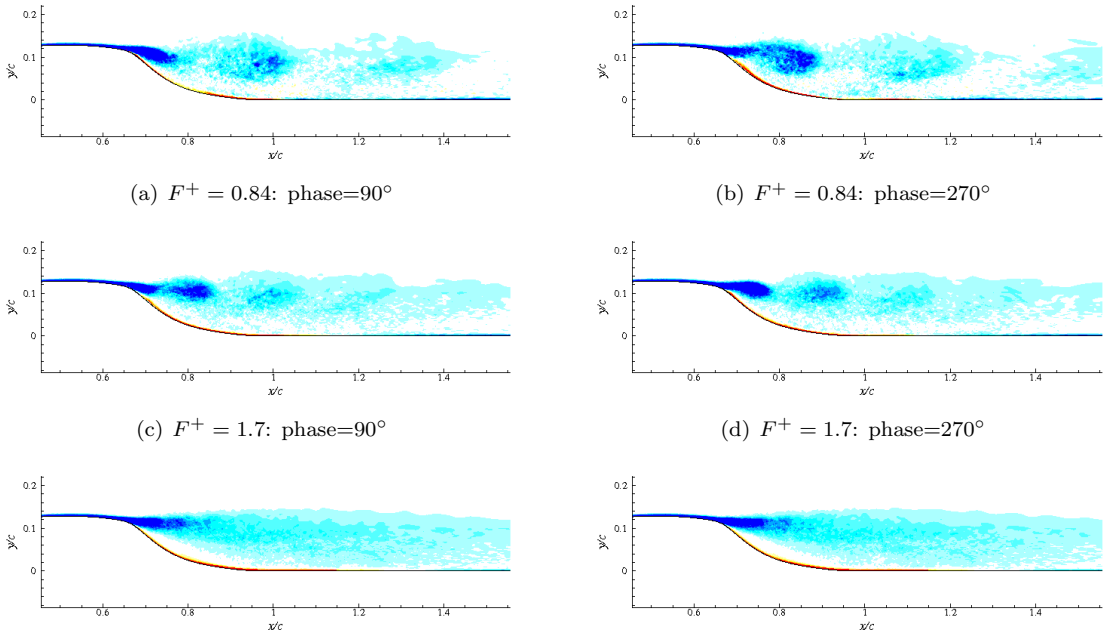

(a) $F^+ = 0.84$: phase=90°

(b) $F^+ = 0.84$: phase=270°

(c) $F^+ = 1.7$: phase=90°

(d) $F^+ = 1.7$: phase=270°

(e) $F^+ = 5.0$: phase=90°

(f) $F^+ = 5.0$: phase=270°

Figure 5.14: Phase-averaged spanwise vorticity corresponding to the blowing (phase=90°) and suction (phase=270°) phases. Contour levels from -30 to 30.

Velocity probes of the span-averaged flow are placed within the shear layer and along the wall at locations described in figure 4.8. The spectra in figures 5.15 represent probes at various locations along the separated region, including a probe at the actuation location itself. The LF and HF actuation cases are directly compared to the corresponding baseline spectra.

At $M = 0.6$, the LF actuated flow displays strong spectral peaks at the forcing frequency for all locations within the shear layer. The most distinct peaks at the actuation frequency occur at actuation ($x/c = 0.655$) and just after separation ($x/c = 0.67$). In the downstream portion of the separation bubble, frequencies lower than the actuation frequency grow in strength indicating that vortices may merge as the separation bubble reattaches. However, the lack of a distinct peak at the subharmonic of the actuation frequency indicates that pairing is not regular. The growth of lower frequencies decreases the actuation frequency peak at $x/c = 0.86$, but at reattachment ($x/c = 1.1$) the actuation frequency has increased again. Pressure probes at the wall also contain peaks at the actuation frequency, but the pressure-spectra peaks are lower than the velocity-spectra peaks from

the shear layer probe. In addition, the amplitude of the actuation peaks in the pressure spectra decrease significantly close to reattachment ($x/c = 1.1$).

When the $M = 0.6$ flow is actuated at $F +^{=} 5$, the velocity spectra displays a peak at the actuation frequency directly at the actuation location of $x/c = 0.655$. This peak is also detectable immediately after separation at $x/c = 0.69$, along with a subharmonic at $F +^{=} 2.5$. However the actuation frequency is no longer present towards the middle of the separation bubble ($x/c = 0.85$) and close to reattachment ($x/c = 1.1$). This is consistent with the lack of coherent structures in the phase-averaged vorticity contours in figure 5.14. This is contrary to the LF actuation, which maintains a peak at the actuation frequency at least until reattachment. With HF actuation, the associated flow structures are too small, and dissipate too quickly to be separated from the turbulence in the separated region. Thus, they have a very minor effect on the reorganization of the flow. Despite the weak appearance of the actuation in the velocity spectra, the pressure spectra have detectable peaks at the actuation frequency for all probes. Therefore, although the actuation may not significantly affect the mean flow, it does have a strong effect the acoustic field.

Similar trends are found in the $M = 0.25$ low and high frequency actuated flow. The baseline and controlled spectra are given in figure 5.16. The spectra of the actuated flow have many of the same attributes as the corresponding $M = 0.6$ flows, such as consistent peaks at the LF actuation for the shear layer velocity and wall pressure probes. However, HF actuation peaks are detected in the shear layer around reattachment, although the peaks are strongly attenuated at $x/c = 0.86$ towards the center of the separated region. The final spectra plot in figure 5.17 is the HF actuation velocity shear layer spectra plotted on log-log coordinates to demonstrate the energy dissipation at high frequencies.

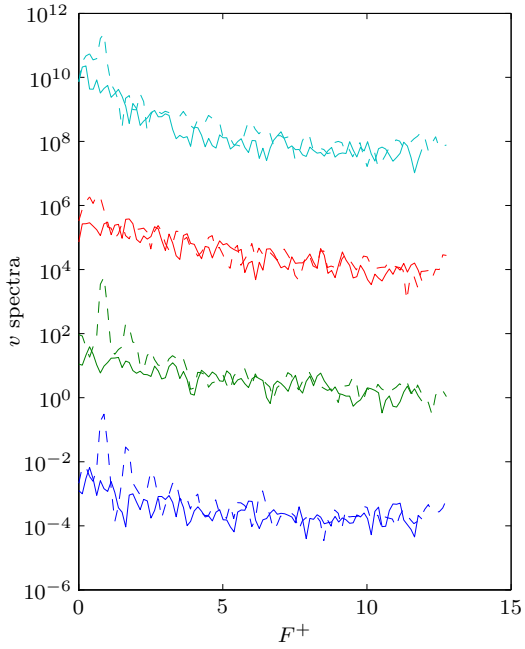

(a) M=0.6 LF: v spectra in the shear layer

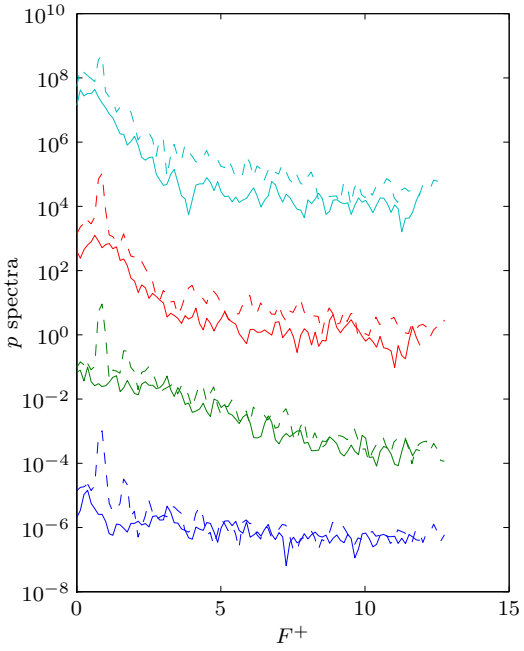

(b) M=0.6 LF: p spectra at the wall

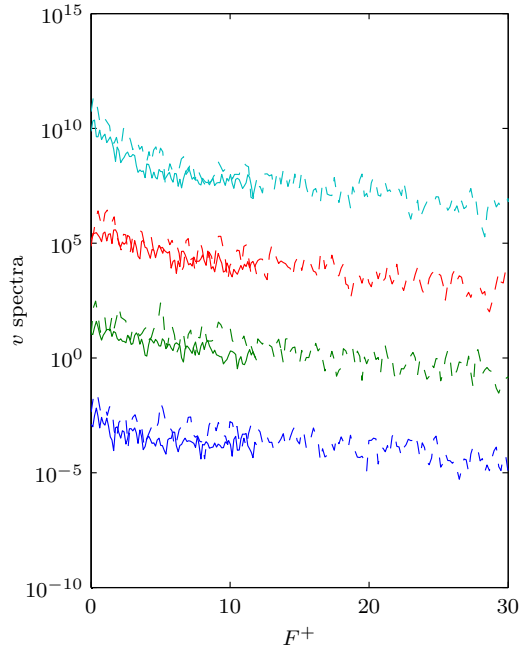

(c) M=0.6 HF v spectra in the shear layer

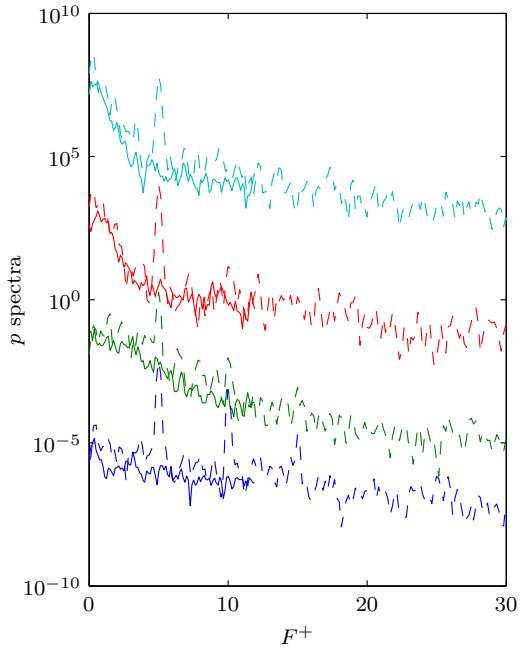

(d) M=0.6 HF: p spectra at the wall

Figure 5.15: $M = 0.6$ spectra from the span-averaged flow at four locations, separated by three decades for easier viewing. Locations are $x/c = 0.655$ (blue), 0.69 (green), 0.86 (red), and 1.1 (cyan), baseline (solid), controlled (dashed).

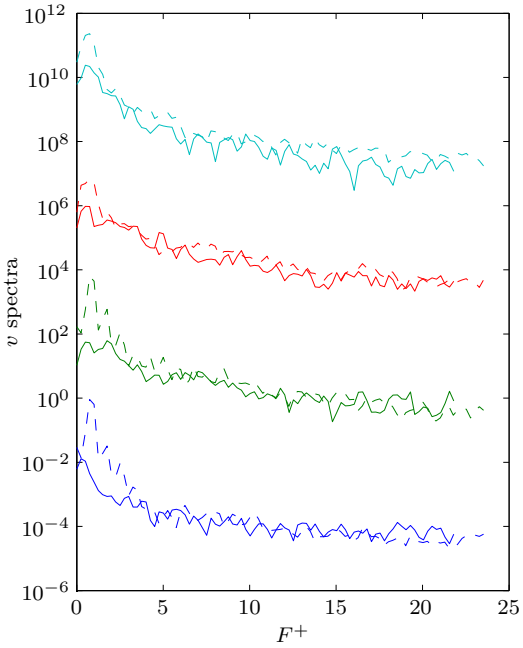

(a) M=0.25 LF: v spectra in the shear layer

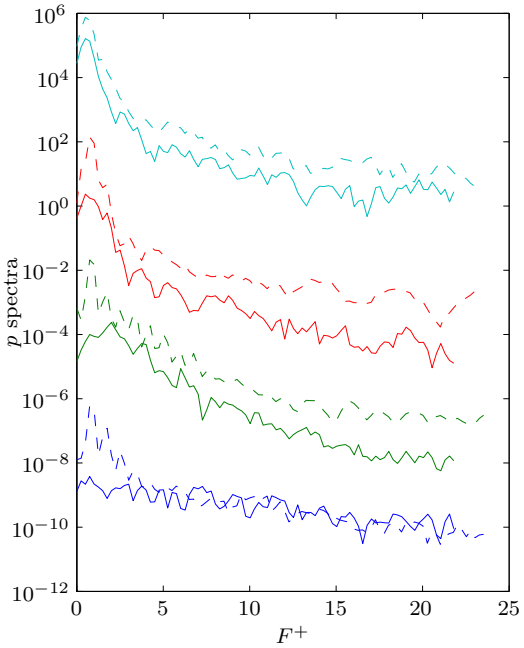

(b) M=0.25 LF: p spectra at the wall

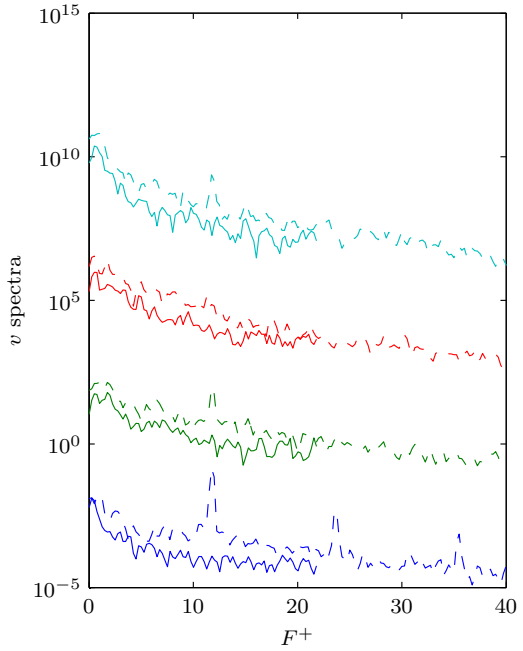

(c) M=0.25 HF v spectra in the shear layer

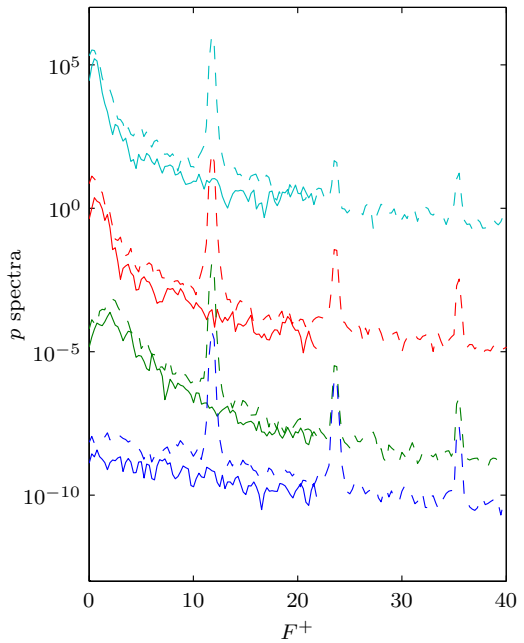

(d) M=0.25 HF: p spectra at the wall

Figure 5.16: $M = 0.25$ spectra from the span-averaged flow, legend the same as figure 5.15.

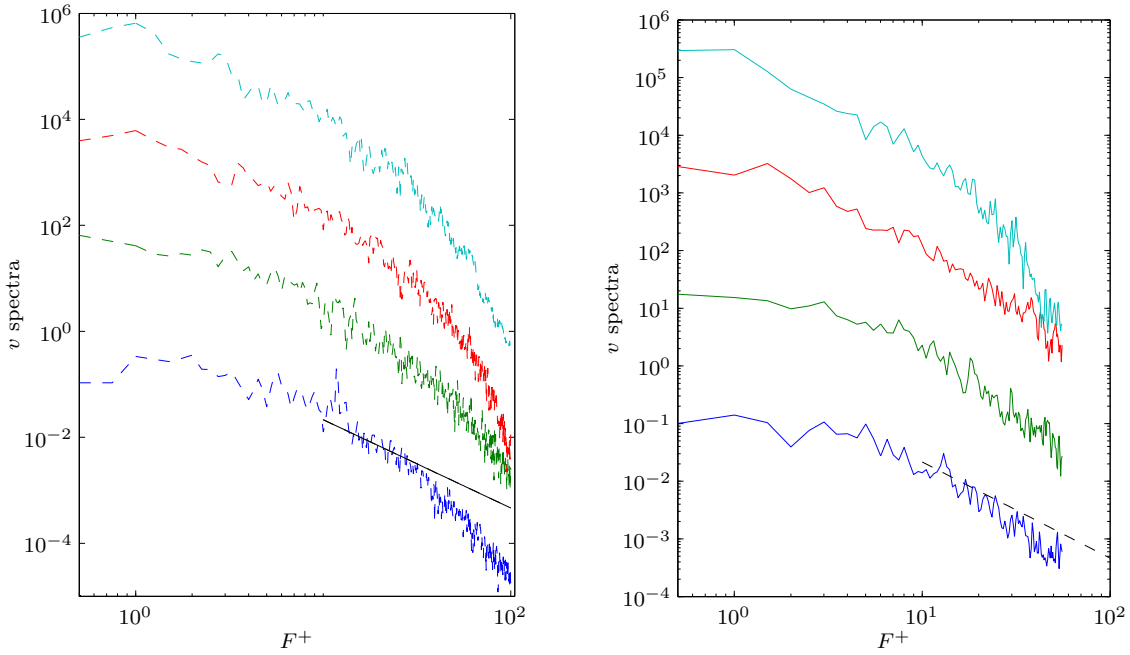

(a) $M = 0.25$ HF: v spectra in the shear layer

(b) $M = 0.6$ HF: v spectra in the shear layer

Figure 5.17: Spectra from the mid-span probes of the HF cases, with the -5/3 slope for reference.

Chapter 6

Conclusions

6.1 Summary

High Reynolds number separated flow and its control have been investigated for a wall-mounted hump geometry. The geometry is characterized by boundary layer separation induced by the convex curvature at 65% of the chord length. Separation is followed by a highly unsteady recirculation region over the trailing edge before the boundary layer reattaches to the wall downstream of the chord. A large-eddy simulation (LES) at $Re_c = 500,000$ was developed to simulate the natural separating flow at Mach numbers 0.25 and 0.6, as well as steady suction and oscillatory zero-net mass flux flow control.

6.1.1 Formulation and Validation of LES

The large-eddy simulation presented in chapter 2 solves the compressible, Favre-averaged Navier-Stokes equations in three dimensions using a high-order finite difference method in generalized coordinates. The subgrid scale stresses were modeled with a compressible, constant Smagorinsky model. A skew-symmetric numerical method and stable summation-by-parts boundary closures were implemented in order to minimize the build-up of numerical instabilities that require additional numerical dissipation or explicit filtering. The modified numerical method provides a stable and robust code capable of simulating under-resolved flows, such as those appropriate for large-eddy simulations.

Furthermore, due to the coordinate transform grid methodology and generalized coordinate system, the code is easily adaptable to other complex geometries.

The LES technique is validated in chapter 3 using the low Mach number experimental results on the wall-mounted hump geometry from Seifert and Pack [3] and Greenblatt et al. [20, 21]. The baseline LES demonstrated a good prediction of the averaged pressure coefficient, and a 7.3% longer separation bubble compared with experiments. The turbulent Reynolds stresses also showed similar trends as the experiments, although they are slightly under-predicted in the reattachment region. Compared with other compressible LES models, the current method has a more accurate prediction of the reattachment location using less than half as many grid points. The baseline LES results were also more accurate than Reynolds-Averaged Navier Stokes (RANS) based simulations.

Steady suction and zero-net flux oscillatory flow control were modeled at the surface boundary such that the control cavity location, size and non-dimensional actuation parameters matched that of the experiments. Control shortened the average size of the separation bubble, whose modified length and pressure recovery location agreed well with experimental data. In the low Mach number oscillatory controlled flow, the addition of the Smagorinsky model is shown to have slightly better prediction of the average actuated flow quantities compared with the equivalent implicit LES, and a better qualitative agreement with the turbulent Reynolds stresses. Comparing two implicit LES with different filters, it is found that filtering out more scales can decrease the rate of pressure recovery at reattachment and over-predict the Reynolds stresses during vortex formation and growth.

6.1.2 Effects of Compressibility

The effects of compressibility on the baseline and controlled flow at $M = 0.6$ were discussed in chapter 4 where they were also compared with the low Mach number flow. The LES accurately predicted features of the baseline compressible flow including a higher suction peak and a longer separation region. The $M = 0.6$ flow had a lower growth rate of vorticity thickness in the initially separated shear layer, which is consistent with previously published free shear layer results. In addition to the lower entrainment rate, there was less growth of the turbulent Reynolds stresses.

With less turbulent fluctuations and lower levels of turbulent kinetic energy in the separated region, the shear layer does not entrain as much fluid from above and below, which delays its growth and subsequent reattachment.

6.1.3 Effectiveness of Flow Control

The effectiveness of the control on the wall-mounted hump was also investigated. Steady suction was found more effective at reducing drag than oscillatory zero-net mass flux actuation. In the $M = 0.25$ flow, steady suction decreased the form drag by 50.5%. At the same levels of C_m, the control was slightly less effectiveness at $M = 0.6$, decreasing the form drag by 48.6%. Thus, the effect of compressibility in the absence of a shock wave does not have a significant effect on the effectiveness of control.

The steady suction control functions by constantly removing fluid from the boundary layer just before separation, creating a large suction peak which is followed by a desirable pressure recovery, and the delay of the boundary layer separation. The drag component is decreased mainly due to the extended pressure recovery region. On the other hand, low frequency oscillatory actuation excites large-scale structures, which increase entrainment and grow in size over the trailing edge. The net force on the steep backward-facing trailing edge has a large drag component, and therefore the presence of large-scale low pressure regions increases the local drag. Since the geometry is mounted to a wall, the benefits of lift, or the lift-to-drag ratio are not realizable. The result of oscillatory forcing is an overall increase in form drag in both the low and higher Mach number flows.

Another performance metric is reducing the length of the recirculation bubble. Both steady suction and low frequency oscillatory control were successful at initiating an earlier reattachment. Since the trailing edge is almost flush with the horizontal wall at the reattachment, an earlier reattachment does not necessarily correlate with lower form drag as it might with an airfoil. At $M = 0.25$ and momentum coefficients of $C_\mu = 0.11\%$, steady suction decreased the baseline separation bubble length by 20.3%, and oscillatory control decreased it by 15.6%. Likewise the $M = 0.6$ flow saw a reduction of 18.6% and 7.8%, respectively.

6.1.4 Comparison of 2D and 3D Flows

Simple two-dimensional direct numerical simulations (DNS) at low Reynolds number were performed to provide a comparison with the high Reynolds number three-dimensional LES. The laminar boundary separates earlier in the two-dimensional simulations and forms a larger average separation bubble. At Reynolds numbers less than $10,000$, the 2D flow has an unsteady shedding of vortices at the end of a free shear layer that extends a full chord length downstream of separation. As the Reynolds number is increased to $15,000$ at $M = 0.25$, the vortices are shed periodically, at a locked-in frequency of $fc/U_\infty = 0.8$. The periodic nature of the shedding reduces the size of the separation bubble.

Although the 3D LES show evidence of large-scale structures shed from the shear layer, the process is unsteady and aperiodic, and a range of frequencies are found in the shear layer spectra. The 3D vortices are also formed closer to separation and dissipate very quickly after they are formed, sometimes merging within the separated region. The periodic vortex shedding of the 2D flow simply convects each vortex downstream. Hence, to fully understand the dynamics of the turbulent separation bubble 3D simulations are necessary to capture the unsteady effects.

6.1.5 Effects of Actuation Frequency

Control of the 2D flow is most effective in shortening the separated region when actuated at frequencies on the same order as the natural shedding frequency. Similar results are seen in the LES simulations, where actuation frequencies from $F^+ \sim O(1)$ to $F^+ \sim O(10)$ are applied to the baseline flow. For both the low and higher Mach numbers, actuation frequencies at $F^+ \sim O(1)$ are more effective in shortening the separated region. The actuation produces large-scale structures that increase entrainment and promote earlier reattachment. At higher frequencies the vorticity structures generated at actuation are small and dissipate very rapidly. With actuation at $F^+ \sim O(10)$, the shear layer reattaches slightly downstream of the baseline flow. The local effect of the actuation decreases the magnitude of the turbulent Reynolds stresses, modifies the average streamlines, but does not delay the onset of separation. Although the mean streamlines and velocity profiles are

altered at the actuation location, there does not appear to be a stabilizing effect with actuation at $F^+ \sim O(10)$. Thus, for the actuation locations and C_μ values investigated, the high frequency actuation is not found to be beneficial for drag reduction or shortening the separation bubble.

6.2 Recommendations for Future Work

There are many interesting problems in the field of flow control, and certainly many hurdles before systems are widely implemented in industrial applications, including robust closed-loop control algorithms. A necessary precursor to closed-loop control is an understanding of the natural and open-loop controlled flow field. This task is challenging due to the variety of separated flows in which active flow control may be beneficial, and the different control objectives and performance factors of each configuration.

One particular question is the effects of high frequency actuation. It has been found to be both beneficial and detrimental, depending on the flow configuration, and thus the fluid mechanisms of high frequency actuation are not widely understood. Although this thesis investigates its effect on the wall-mounted hump flow for a limited range of parameters, more exhaustive investigations of other parameters and flow configurations could help in understanding the potential benefits of high frequency actuation.

Another facet of understanding the separated flow system is documenting the response of the flow to an impulse of control, such as a pulsatile blowing or suction. This can be important in understanding the transient effects of flow control, and the reaction time to gusts and other unpredictable natural phenomena that are encountered.

The long term goals are to gain understanding and insight into the flow dynamics such that robust feedback control can be designed and implemented. Such systems have the potential to increase the aerodynamic and hydrodynamic efficiency in many applications whose performance is impeded by flow separation.

Appendix A

Non Favre-Averaged LES Equations

A.1 Non Favre-Averaged Filtered Equations

The filtered compressible Navier-Stokes equations in the non Favre-averaged form are given by Eqs. (A.1).

$$\frac{\partial \bar{\rho}}{\partial t} + \frac{\partial}{\partial x_j}\bar{\rho}\bar{u}_j = \frac{\partial}{\partial x_j}F_{m_j} \tag{A.1a}$$

$$\frac{\partial}{\partial t}\bar{\rho}\bar{u}_i + \frac{\partial}{\partial x_j}(\bar{\rho}\bar{u}_i\bar{u}_j - \bar{\tau}_{ji}) + \frac{\partial \bar{p}}{\partial x_i} = \frac{\partial}{\partial t}F_{m_j} + \frac{\partial}{\partial x_j}F_{u_j m_j} \tag{A.1b}$$

$$\frac{\partial}{\partial t}\bar{\rho}\bar{E} + \frac{\partial}{\partial x_j}((\bar{\rho}\bar{E} + \bar{p})\bar{u}_j + \bar{q}_j - \bar{\tau}_{ji}\bar{u}_i) = \frac{\partial}{\partial t}F_{\rho E} + \frac{\partial}{\partial x_j}F_{(\rho E+p)u_j} \tag{A.1c}$$

The filtered stress tensor, $\bar{\tau}_{ij}$, and heat flux vector, $\bar{q}_j$, are given below in Eqs. (A.2).

$$\bar{\tau}_{ij} = \mu(\frac{\partial \bar{u}_i}{\partial x_j} + \frac{\partial \bar{u}_j}{\partial x_i}) + \frac{2\mu}{3}\frac{\partial \bar{u}_k}{\partial x_k}\delta_{ij} \tag{A.2a}$$

$$\bar{q}_j = \frac{\mu}{Pr}\frac{\partial \bar{T}}{\partial x_j} \tag{A.2b}$$

$$\bar{S}_{ij} = \frac{1}{2}\left(\frac{\partial \bar{u}_i}{\partial x_j} + \frac{\partial \bar{u}_j}{\partial x_i}\right) \tag{A.3a}$$

$$|\bar{S}| = (2\bar{S}_{ij}\bar{S}_{ij})^{1/2} \tag{A.3b}$$

$$F_{m_j} = C_\rho \Delta^2 |\bar{S}| \frac{\partial \bar{\rho}}{\partial x_i} \tag{A.4a}$$

$$F_{u_j m_j} = C_s \Delta^2 \bar{\rho} |\bar{S}| \bar{S}_{ij} \tag{A.4b}$$

$$F_{(\rho E+p)u_j} = C_q \Delta^2 \bar{\rho} |\bar{S}| \frac{\partial \bar{T}}{\partial x_j} \tag{A.4c}$$

A.2 Dynamic Smagorinsky Formulation

The coefficients C_ρ, C_s, and C_q can also be calculated dynamically at every time step in the same manner as Bodony [33]. The expressions for the dynamic coefficients are shown in Eqs. (A.5), and utilize a test filter with width, $\hat{\Delta} \approx 2\Delta$, whose expression is given in Eq. (A.6). The test filter is consecutively applied in all three coordinate directions.

$$C_\rho = \frac{\langle L_{ij} M_{ij} \rangle}{\langle M_{pq} M_{pq} \rangle}, \quad C_s = -\frac{\langle P_i O_i \rangle}{\langle O_j O_j \rangle}, \quad C_q = -\frac{\langle K_i N_i \rangle}{\langle N_j N_j \rangle} \tag{A.5}$$

$$\hat{f} = \frac{1}{6}(f_{i-1} + 4f_i + f_{i+1}) \tag{A.6}$$

$$L_{ij} = \widehat{\bar{\rho}\bar{u}_i\bar{u}_j} - \hat{\bar{\rho}}\hat{\bar{u}}_i\hat{\bar{u}}_j, \quad P_i = \widehat{\bar{\rho}\bar{u}_i} - \hat{\bar{\rho}}\hat{\bar{u}}_i, \quad K_i = \widehat{\bar{\rho}\bar{u}_i\bar{T}} - \hat{\bar{\rho}}\hat{\bar{u}}_i\hat{\bar{T}} \tag{A.7}$$

$$M_{ij} = \Delta^2 \widehat{\bar{\rho}|\bar{S}|\bar{S}_{ij}} - \hat{\Delta}^2 \hat{\bar{\rho}} |\hat{\bar{S}}| \hat{\bar{S}}_{ij} \tag{A.8a}$$

$$N_i = \hat{\Delta}^2 \hat{\bar{\rho}} |\hat{\bar{S}}| \frac{\partial \hat{\bar{T}}}{\partial x_i} - \Delta^2 \widehat{\bar{\rho}|\bar{S}| \frac{\partial \hat{T}}{\partial x_i}} \tag{A.8b}$$

$$O_i = \hat{\Delta}^2 |\hat{\bar{S}}| \frac{\partial \hat{\rho}}{\partial x_i} - \Delta^2 \widehat{|\bar{S}| \frac{\partial \hat{\rho}}{\partial x_i}} \tag{A.8c}$$

The $\langle\rangle$ notation refers to a spatial averaging over the homogenous coordinates, or the spanwise direction for this flow.

Appendix B

Inlet Noise Perturbations

B.1 Computation of Random Fourier Modes

In order to accelerate the development of a turbulent boundary layer a Gaussian region of random Fourier modes was prescribed at the inlet, superimposed with a turbulent boundary layer profile. This method is a simplification of the noise model proposed by Bechara et al. [39]. Perturbations $\mathbf{u}'(\mathbf{x}, t)$ are defined by Eq. (B.1).

$$\mathbf{u}'(\mathbf{x}, t) = \sum_{k=1}^{N} A_n cos(\mathbf{k}_n \cdot \mathbf{x} + \omega_n t + \Phi_n)\boldsymbol{\sigma}_n \tag{B.1}$$

The equation represents a sum of Fourier modes with amplitudes A_n. The wave vector is denoted by $\mathbf{k}_n$, with its phase and direction unit vector given by Φ_n and $\boldsymbol{\sigma}_n$ respectively. The wave vector is calculated from its spherical components (k_n, ϕ_n, θ_n). The approximation for ω_n is given by $\omega_n = 2\pi k_n 0.05M$. The incompressible flow condition of $\mathbf{k}_n \cdot \boldsymbol{\sigma}_n = 0$ is imposed, thus $\boldsymbol{\sigma}_n$ is always perpendicular to $\mathbf{k}_n$, and has only one free angle, α_n. The wavenumbers k_n range in size from the Kolmogorov scale k_{kol} to the integral lengthscale k_1. They are calculated from Eqs. (B.2) using a logarithmic step to provide a better distribution of wavenumbers in the larger scales which contain

most of the energy.

$$\Delta k = (\log(k_{kol}) - \log(k_1))/(N-1) \tag{B.2a}$$

$$k_n = \exp(\log(k_1) + (N-1)\Delta k) \tag{B.2b}$$

The angle components of $\mathbf{k}_n$, ϕ_n and θ_n, are calculated randomly using uniform probability density functions $P(\phi_n) = 1/\pi$ and $P(\theta_n) = 1/2\pi$. Φ_n is also calculated randomly with $P(\Phi_n) = 1/2\pi$. The free angle of the direction vector, or α_n, is calculated by $P(\alpha_n) = 1/2\pi$. In order to ensure proper resolution of the spanwise perturbations, the randomized wavenumbers in the x_3 spatial direction are aligned with the closest resolved Fourier mode. The amplitude of each mode is calculated from a crude model of the energy spectrum, a weighting function $w(y)$, and a scalar input a_1 to adjust the overall level of perturbations.

$$A_n = a_1 E(k_n) w(y) \tag{B.3a}$$

$$E(k) = 11.4 \exp\left(\frac{-0.584(k_n/k_e)^2(k_n/k_e)^4)}{(1+(k_n/k_e)^2)^{2.833}}\right) \tag{B.3b}$$

$$w(y) = \frac{a_2 y}{1 + a_3 y(1-\exp(-y))^2} \tag{B.3c}$$

The scalars a_2 and a_3 should be adjusted for the boundary layer thickness, and the value of k_e sets the peak of the energy spectrum. The values of the constants and parameters commonly used in the hump flow simulation are given in table B.1.

Table B.1: Noise perturbation constants.

Constant	Value
N	50
k_1	62,000
k_e	78
k_{kol}	5470
a_1	0.54
a_2	30
a_3	4000

Bibliography

[1] Greenblatt, D. and Wygnanski, I. J., "The control of flow separation by periodic excitation," *Progress in Aerospace Sciences*, Vol. 36, 2000, pp. 487–545.

[2] Glezer, A. and Amitay, M., "Synthetic Jets," *Annual Review of Fluid Mechanics*, Vol. 34, No. 1, 2002, pp. 503–529.

[3] Seifert, A. and Pack, L., "Active flow separation control on wall-mounted hump at high Reynolds numbers," *AIAA Journal*, Vol. 40, No. 7, Jul 2002, pp. 1363–1372.

[4] Castro, I. P. and Haque, A., "The structure of a turbulent shear layer bounding a separation region," *Journal of Fluid Mechanics Digital Archive*, Vol. 179, No. -1, 1987, pp. 439–468.

[5] Eaton, J. and Johnston, J., "A Review of Research on Subsonic Turbulent-Flow Reattachment," *AIAA Journal*, Vol. 19, No. 9, 1981, pp. 1093–1100.

[6] Hudy, L., Naguib, A., and Humphreys, W., "Wall-pressure-array measurements beneath a separating/reattaching flow region," *Physics of Fluids*, Vol. 15, No. 3, Mar 2003, pp. 706–717.

[7] Sigurdson, L., "The structure and control of a turbulent reattaching flow," *Journal of Fluid Mechanics*, Vol. 298, Sep 10 1995, pp. 139–165.

[8] Kiya, M., Shimizu, M., and Mochizuki, O., "Sinusoidal forcing of a turbulent separation bubble," *Journal of Fluid Mechanics*, Vol. 342, Jul 10 1997, pp. 119–139.

[9] Nishri, B. and Wygnanski, I., "Effects of Periodic Excitation on Turbulent Fow Separation from a flap." *AIAA Journal*, Vol. 36, No. 4, 1998, pp. 547–556.

[10] Seifert, A. and Pack, L., "Active Control on Generic Configurations at High Reynolds Numbers," *30th AIAA Fluid Dynamics Conference*, Jun 1999.

[11] Amitay, M. and Glezer, A., "Role of Actuation Frequency in Controlled Flow Reattachment over Stalled Airfoil," *AIAA Journal*, Vol. 40, No. 2, 2002, pp. 209–216.

[12] Glezer, A., Amitay, M., and Honohan, A., "Aspects of low- and high-frequency actuation for aerodynamic flow control," *AIAA Journal*, Vol. 43, No. 7, Jul 2005, pp. 1501–1511.

[13] Wu, J., Lu, X., Denny, A., Fan, M., and Wu, J., "Post-stall flow control on an airfoil by local unsteady forcing," *Journal of Fluid Mechanics*, Vol. 371, Sep 1998, pp. 21–58.

[14] Raju, R., Mittal, R., and Cattafesta, L., "Dynamics of Airfoil Separation Control Using Zero-Net Mass-Flux Forcing," *AIAA Journal*, Vol. 46, No. 12, Dec 2008, pp. 3103–3115.

[15] Dandois, J., Garnier, E., and Sagaut, P., "Numerical simulation of active separation control by a synthetic jet," *Journal of Fluid Mechanics*, Vol. 574, Mar 10 2007, pp. 25–58.

[16] Stanek, M., Raman, G., Ross, J., Odedra, J., Peto, J., Alvi, F., and Kibens, V., "High Frequency Acoustic Suppression-The Role of Mass Flow, The Notion of Superposition, And The Role of Inviscid Instability - A New Model (Part II)." *8th AIAA/CEAS Aeroacoustics Conference and Exhibit*, Jun 2002.

[17] Seifert, A. and Pack, L., "Compressibility and Excitation Location Effects on High Reynolds Numbers Active Separation Control," *Journal of Aircraft*, Vol. 40, No. 1, 2003, pp. 110–119.

[18] Pack, L. and Seifert, A., "Effects of sweep on the dynamics of active separation control," *Aeronautical Journal*, Vol. 107, No. 1076, Oct 2003, pp. 617–629.

[19] Rumsey, C. L., Gatski, T. B., Sellers, W. L., Vatsa, V. N., and Viken, S. A., "SumMary of the 2004 computational fluid dynamics validation workshop on synthetic jets," *AIAA Journal*, Vol. 44, No. 2, 2006, pp. 194–207.

[20] Greenblatt, D., Paschal, K. B., Yao, C.-S., Harris, J., Schaeffler, N.-N. W., and Washburn, A. E., "Experimental investigation of separation control - Part 1: Baseline and steady suction," *AIAA Journal*, Vol. 44, No. 12, Dec 2006, pp. 2820–2830.

[21] Greenblatt, D., Paschal, K. B., Yao, C.-S., and Harris, J., "Experimental investigation of separation control - Part 2: Zero mass-flux oscillatory blowing," *AIAA Journal*, Vol. 44, No. 12, Dec 2006, pp. 2831–2845.

[22] NAughton, J., Viken, S., and Greenblatt, D., "Skin-friction measurements on the NASA hump model," *AIAA Journal*, Vol. 44, No. 6, Jun 2006, pp. 1255–1265.

[23] Morgan, P. E., Rizzetta, D. P., and Visbal, M. R., "Large-eddy simulation of separation control for flow over a wall-mounted hump," *AIAA Journal*, Vol. 45, No. 11, Nov 2007, pp. 2643–2660.

[24] Saric, S., Jakirlic, S., Djugum, A., and Tropea, C., "Computational analysis of locally forced flow over a wall-mounted hump at high-Re number," *International Journal of Heat and Fluid Flow*, Vol. 27, No. 4, 2006, pp. 707–720.

[25] You, D., Wang, M., and Moin, P., "Large-eddy simulation of flow over a wall-mounted hump with separation control," *AIAA Journal*, Vol. 44, No. 11, Nov 2006, pp. 2571–2577.

[26] Franck, J. A. and Colonius, T., "A Compressible Large-Eddy Simulation of Separation Control on a Wall-Mounted Hump." *46th AIAA Aerospace Sciences Meeting and Exhibit*, Jan 2008.

[27] Moin, P., Squires, K., Cabot, W., and Lee, S., "A dynamic subgrid-scale model for compressible turbulence and scalar transport," *Physics of Fluids A-Fluid Dynamics*, Vol. 3, No. 11, Nov 1991, pp. 2746–2757.

[28] Gloerfelt, X., Bogey, C., and Bailly, C., "Numerical Evidence of Mode Switching in the Flow-Induced Oscillations by a Cavity," *International Journal of Aeroacoustics*, Vol. 2, No. 2, 2003, pp. 99–123.

[29] Pirozzoli, S. and Colonius, T., "Assessment of a high fidelity numerical code for Direct Numerical Simulation of flow in a diffuser geometry," Internal Caltech Document, 2000.

[30] Mattsson, K. and Nordström, J., "Summation by parts operators for finite difference approximations of second derivatives," *J. Comput. Phys.*, Vol. 199, No. 2, 2004, pp. 503–540.

[31] Suzuki, T., Colonius, T., and Pirozzoli, S., "Vortex shedding in a two-dimensional diffuser: theory and simulation of separation control by periodic mass injection," *Journal of Fluid Mechanics*, Vol. 520, Dec 10 2004, pp. 187–213.

[32] Fung, J., "Parallel implementation and general revision of the diffuser code," Internal Caltech Document, 2004.

[33] Bodony, D., *Aeroacoustic Prediction of Turbulent Free Shear Flows*, Ph.D. thesis, Stanford University, Dec. 2004.

[34] Boersma, B. and Lele, S., "Large eddy simulation of compressible turbulent jets," Annual research briefs, Center for Turbulence Research, 1999.

[35] Visbal, M. and Gaitonde, D., "High-order-accurate methods for complex unsteady subsonic flows," *AIAA Journal*, Vol. 37, No. 10, Oct 1999, pp. 1231–1239.

[36] Kravchenko, A. G. and Moin, P., "On the effect of numerical errors in large eddy simulations of turbulent flows," *J. Comput. Phys.*, Vol. 131, No. 2, 1997, pp. 310–322.

[37] Honein, A. E. and Moin, P., "Higher entropy conservation and numerical stability of compressible turbulence simulations," *J. Comput. Phys.*, Vol. 201, No. 2, 2004, pp. 531–545.

[38] Driscoll, T. A. and Trefethen, L. N., *Schwarz-Christoffel Mapping*, Cambridge University Press, 2002.

[39] Bechara, W., Bailly, C., Lafon, P., and Candel, S., "Stochastic Approach to Noise Modeling for Free Turbulent Flows," *AIAA Journal*, Vol. 2, 2003, pp. 99–123.

[40] Freund, J., "Proposed inflow/outflow boundary condition for direct computation of aerodynamic sound," *AIAA Journal*, Vol. 35, No. 4, Apr 1997, pp. 740–742.

[41] Postl, D. and Fasel, H., "Direct numerical simulation of turbulent flow separation from a wall-mounted hump," *AIAA Journal*, Vol. 44, No. 2, Feb 2006, pp. 263–272.

[42] Capizzano, F., Catalano, P., Marongiu, C., and Vitagliano, P. L., "U-RANS Modelling of Turbulent Flows Controlled by Synthetic Jets," *35th AIAA Fluid Dynamics Conference and Exhibit*, Jun 2005.

[43] Ho, C. and Huerre, P., "Perturbed Free Shear Layers," *Annual Review of Fluid Mechanics*, Vol. 16, 1984, pp. 365–424.

[44] Browand, F. and Troutt, T., "The Turbulent Mixing Layer - Geometry of Large Vortices," *Journal of Fluid Mechanics*, Vol. 158, No. Sep, 1985, pp. 489–509.

[45] Papamoschou, D. and Roshko, A., "The Compressible Turbulent Shear-Layer - An Experimental-Study," *Journal of Fluid Mechanics*, Vol. 197, Dec 1988, pp. 453–477.

[46] Slessor, M., Zhuang, M., and Dimotakis, P., "Turbulent shear-layer mixing: growth-rate compressibility scaling," *Journal of Fluid Mechanics*, Vol. 414, Jul 10 2000, pp. 35–45.

[47] Pantano, C. and Sarkar, S., "A study of compressibility effects in the high-speed turbulent shear layer using direct simulation," *Journal of Fluid Mechanics*, Vol. 451, Jan 2002, pp. 329–371.

[48] Pack, L. and Seifert, A., "Dynamics of Active Separation Control at High Reynolds Numbers," *38th Aerospace Sciences Meeting and Exhibit*, Jan 2000.